A Passive Microfluidic Device for Buffer Transfer of Cells

Sudharsan Thattai Sadagopan

Thesis submitted to the Faculty of the
Virginia Polytechnic Institute and State University
in partial fulfillment of the requirements for the degree of

Masters of Science
in
Engineering Mechanics

Mark A. Stremler, Chair
Rafael V. Davalos
Jonathan B. Boreyko

September 15, 2021
Blacksburg, Virginia

Keywords: Microfluidics, Computational Fluid Dynamics, Electrical Conductivity, Fluid Induced Shear Stress, Throughput, Buffer.

A Passive Microfluidic Device for Buffer Transfer of Cells

Sudharsan Thattai Sadagopan

(ABSTRACT)

Buffer transfer of cells is a critical process in many biomedical applications such as dielectrophoresis experiments, optical trapping, and flow cytometry. Existing methods for buffer transfer of cells are time consuming, require skilled technicians and involve expensive equipment such as centrifuges and bio safety hoods. Furthermore, even a minute error in transferring the cells can easily result in cell lysis and decrease in sample viability. In this work, a lab-on-a-chip device is proposed that uses a *passive microfluidic approach* to effectively transfer cells from a growth medium to a desired fluid buffer for downstream contactless dielectrophoresis (cDEP) analysis. This approach eliminates the need for any external fields or expensive equipment, and it significantly reduces manual efforts. Computational studies were carried out to analyze the impact of device geometry, channel configuration, and flowrate on the effectiveness of the buffer transfer. The proposed device was evaluated through a parametric sweep, and the device configurations were identified that induce low values of fluid shear stress, support high throughput, and maintain minimal diffusion. Finally, a method for fabricating the device in the laboratory using polydimethylsiloxane (PDMS) was illustrated. The outcome of this study helps further the development of highly effective microfluidic devices capable of performing buffer transfer of multiple cell lines.

A Passive Microfluidic Device for Buffer Transfer of Cells

Sudharsan Thattai Sadagopan

(GENERAL AUDIENCE ABSTRACT)

Prior to performing biomedical experiments, cells often need to be transferred from the chemical solution in which they are grown to a different fluid buffer that is customized for the analysis technique. This process is called buffer transfer and it is a critical process that needs to be performed before running many cell experiments. The way in which buffer transfer is carried out in most labs is time consuming, requiring skilled technicians and expensive machines. Moreover, even a small error while performing buffer transfer can easily cause the cells to die and reduce the cell count available for performing experiments. In this work, we propose an easy-to-use device that can perform the buffer exchange process without the need for expensive technologies or skilled technicians. The device achieves this exchange by leveraging fluid flow in the channel to filter the cells out of the growth medium and transferring the cells to the desired chemical solution while washing the unwanted chemical solution away. We used computer aided drawing (CAD) modeling and computational analysis to develop the device. The performance of the device was enhanced through a parametric analysis such that the device induces low shear stress, supports high flow through the channels and limits the mixing between the growth medium and the buffer. Finally, we have also illustrated a method for building the device in the laboratory. The results of this research work would help in furthering current efforts in the buffer transfer of cells.

Dedication

I dedicate this work to my parents for their unconditional love, unwavering support and for being a source of inspiration throughout my life.

Acknowledgments

I express my deepest gratitude to my advisor, Dr. Mark Stremler, for his support, guidance and trust throughout my master's journey. I also thank him for providing me an opportunity to work on this research project, and giving me the creative space to explore, learn and grow. I thank Dr. Rafael Davalos and Dr. Jonathan Boreyko for graciously accepting to be a part of my committee. The analytical and critical thinking skills I picked up from Dr Boreyko's course helped me throughout my masters journey. I am also grateful to Dr. Davalos for letting me be a part of his lab for a few months and supporting me in my research. I would like to acknowledge Josie Duncan for being a patient mentor and a supportive teammate. A special thanks to Dr. Alexandra Hyler for her support throughout my research and for giving me an opportunity to be a part of her amazing team for a few months. I also acknowledge Rose Keating for her enthusiastic contribution to this research work

I am grateful to my sister for the moral support, especially in the past year. I also thank my friends Neilashwin Raj, Ravikiran Bollineni, Bharath Bharadwaj and Manu Nimmala for all their encouragement and collaboration in multiple courses. I thank Lakshman Maalolan and Madhava Krishnan for being there during the lows and the highs, and making my stay in Blacksburg memorable. The inputs and encouragement from my family and friends has been vital in shaping my masters journey.

Finally, I extend my gratitude to the Biomedical Engineering and Mechanics Department at Virginia Tech for giving me an opportunity to pursue my masters and providing me the resources to carry out my research.

Contents

List of Figures

List of Tables

List of Abbreviations

μ TAS Micro Total Analysis System

2D Two Dimensional

3D Three Dimensional

BEAM Biomedical Engineering and Mechanics

cDEP contactless Di-ElectroPhoresis

CEH Center for Engineered Health

CFD Computational Fluid Dynamics

CTC Circulating Tumor Cells

DI De-Ionized

DLD Deterministic Lateral Displacement

DPM Discreet Phase Model

DRIE Deep Reactive Ion Etching

FSS Fluid Induced Shear Stress

GUI Graphical User Interface

ICP Inductively Coupled Plasma

NS Navier Stokes

PBS Phosphate Buffered Saline

PDMS Polydimethylsiloxane

PMMA Polymethylmethacrylate

PS Polystyrene

PTFE Polytetrafluoroethylene

RBC Red Blood Cells

S Siemens - a unit of electrical conductivity

t-pff-v Tilted Pinched Flow Fractionation Device with Vertical Focusing Channels

TDS Total Dissolved Salts

Chapter 1

Introduction

1.1 Microfluidic Devices

Microfluidic lab-on-chip devices are used in a plethora of biomedical applications [16]. A few applications include cell sorting and separation [37], organ on chip [76], dielectrophoresis [88], bio sensors [39], flow cytometry [14], micro total analysis systems (μTAS) [2], at home diagnostics [17], cell characterisation [10], visualization [15], cell manipulation [86] and buffer exchange [72]. Small size, ease of fabrication, low cost and wide ranging applications have caused the popularity of such devices to skyrocket over the years [83]. There are two different classifications of devices, namely active and passive devices.

The primary method of operation of a passive microfluidic device involves leveraging fluid forces in the channel to move the cells and manipulate them without depending on external forces or fields [46]. These devices are easy to fabricate, cost effective, and relatively simple to use. However, since they can only make use of the inherent microfluidic forces, their applications are a bit limited. The second category of device requires active application of an external force in addition to the ambient fluid flow in the channel, such as an electrical field, magnetic field, optical or acoustic fields, to name a few [65]. Even though active devices have a very wide range of application, they are comparatively more expensive and often require complicated setups to perform experiments.

One of the major applications of passive microfluidic devices involves manipulation of cells and controlling their position in the channel using forces generated by the fluid flow. With a precise device design, the forces of interaction between the cell, fluid, and the walls of the channel can be controlled and the cells can be made to move between different streamlines of the flowing fluid. This is often used in cell sorting, separation, and buffer transfer [30].

1.2 Current Buffer Transfer Process

Buffer transfer is the process of transferring the cells from a growth medium to a desired buffer for further downstream processing. This is a critical process, and even a small error may cause the cells to undergo lysis. The current widely used method for transferring the cells between buffers is a manual process in which the confluent cells are first trypsinized under a bio safety hood. Then the solution containing the cells is carefully pipetted out to a test tube and the desired quantity of buffer is added. The mixture is then transferred to a centrifuge and is subjected to density gradient centrifugation, with the heavier cells settling in the base of the test tube and the lighter fluid collecting above. The trypsin and buffer is carefully removed from the test tube under the bio safety hood. Care is taken to avoid the cells from getting piptetted out along with the fluid. Once the solution is removed, the required quantity of buffer is added to the test tube and the contents are mixed so that the cells will get suspended in the buffer. Once the buffer transfer is complete, the cells are used for downstream experimentation. This process is time consuming, requires expertise, and involves the use of expensive laboratory equipment. Moreover, there is very little control over the shear stress imparted on the cell and the final electrical conductivity and concentration of the buffer.

Efforts have been made through the years for developing an effective microfluidic device

for buffer transfer of cells. This involves using the inertial and fluid forces generated in the channel to control the cell and fluid motion and change the cell position in the device. Different microfluidic methods for cell manipulation are discussed in the following section.

1.3 Passive Microfluidic Methods for Cell Manipulation, Sorting and Buffer Transfer

Since passive methods rely primarily on the inertial forces in the channel, the size, shape, and density of the cells are important while displacing them in the fluid medium inside the channel [64]. In one type of passive microfluidic cell manipulation device, inertial forces from the fluid flowing close to the wall cause a lift force. This force is used in migrating cells across streamlines in laminar flow. One of the pioneering works in this area was by Di Carlo *et al.* [11], who used serpentine channels for size-based separation. The device supports high throughput and is used frequently in flow cytometry applications. Similarly, a technique called Dean Flow Fractionation was used by Hou *et al.* [24] to isolate circulating tumor cells (CTCs) from blood. In this process, the cells are subjected to a centrifugal force by making them flow through a spiral channel. Based on the size, mass and density, the cells get migrated to specific streamlines within the channel and are extracted from different outlets. In a similar work, Guan *et al.* [18] found that a trapezoidal cross section enhances the performance of a spiral channel, which leads to better sorting and separation. Parichehreh *et al.* [52] showed that the inertial forces in a straight microfluidic channel can be leveraged for manipulating cells in a channel. This manipulation was achieved by altering the aspect ratio of the channel.

Another class of devices that makes use of inertial forces in straight channels is the pinched

flow fractionation devices. In this method, the cells are pushed by the fluid against a wall of the channel in a narrow cross sectional area in the device called the pinched section. Then the particles are made to flow through a broadened section where they separate based on size [84]. This has been leveraged by Nho *et al.* to achieve size based separation of red blood cells (RBCs) and platelets [48].

Deterministic lateral displacement (DLD) is a technique of manipulating cells using a periodic array of microposts. In this design, each row is periodically offset from the next by a fixed distance [40]. Huang *et al.* [25] showed that small cells move easily between the pillars compared to the larger cells. This causes the smaller cells to follow a different fluid streamline, leading to separation.

DLD and micropillar arrays have inspired a host of filtration techniques. One such widely used method is called *size exclusion filtration* [42]. In this method, the micropillars are arranged such that the spacing between the posts reduces with distance. As a result, cells are selectively filtered based on size and shape. To reduce the chances of clogging during the filtration process, a cross flow filtration technique is used. An array of lateral slits are aligned along the flow direction so they act like a sieve in which the cells get filtered based on size [44].

Another commonly used filtration technique is called *hydrodynamic filtration* [85]. Here, multiple branched outlets are used to filter cells by size. The cells are pushed towards the outlet by a cross flow. The fluid draining from the outlet pulls the cells through the channels. The smaller cells exit through the near outlets while the larger ones exit through the outlets downstream. The above techniques used for cell manipulation, flow control and cell filtration could be leveraged to develop a device for effective buffer exchange of cancer cells.

In the standard buffer transfer process, there is very little control over the shear stress

imparted in the cells which could cause cell lysis. Furthermore, the process consumes lots of time, upwards of 45 minutes to get a viable batch of cells. Finally there is little control over the electrical conductivity of the final buffer, which is very critical for downstream cDEP analysis. In addition to the above, the process requires expensive equipment like a bio-safety hood for safely handling the cancer cells and a centrifuge for separating the cells from the growth solution.

1.4 Objective

The objective of the current work is to design a novel passive microfluidic device capable of leveraging the inertial and fluid forces in the channel to transfer cells from the biological buffer to the cDEP buffer for downstream cDEP analysis.

In addition to buffer exchange, the device should also be capable of

- minimizing diffusion in the channel so as to maintain significant control over electrical conductivity at the outlet, which is critical for cDEP analysis,
- maintaining a sufficiently low value of shear stress so that the cells don't undergo lysis during the buffer transfer process, and
- supporting high throughput and reducing the time taken for buffer transfer significantly, compared to current manual techniques.

The design, computational fluid dynamic (CFD) modeling, and fabrication of the device are discussed in detail in the subsequent chapters.

Chapter 2

Design of the Buffer Exchange Device

2.1 3D Model and Dimensions

The three dimensional model of the buffer exchange device was designed in SolidWorks 2019. The proposed buffer exchange device has three sections, namely, the inlet region, the main channel, and the side channel. This is a two layered device in which the first layer consists of the inlet section and the main channel and the second layer consists of the side channels, as shown in Figure 2.1a. There are two inlets, one for the cell solution and one for the buffer. The buffer solution flows at either 10 times or 30 times the velocity of the cell solution. When the two solutions reach the main channel, the high velocity buffer solution pushes the low velocity cell solution out through the side channel, as shown in Figure 2.1b. Since the overlap gap, shown in Figure 2.1c, between the main and side channel is less than the cell diameter, the cells get filtered out of the cell solution and are transferred into the buffer solution and remain the main channel, thus bringing about buffer exchange. Figure 2.1d shows the alignment between the main channel and the side channels.

The 2D design with dimensions is shown in Figure 2.2 for a buffer exchange device with 4 side channels and 45° wall angle. The height of the channels were designed to be 50 μm. The width of the inlet channels was 450 μm and they were designed such that they converged at a 30^o angle at the main channel inlet. The length and width of the main channel were designed to be 4000 μm (4mm) and 300 μm respectively.

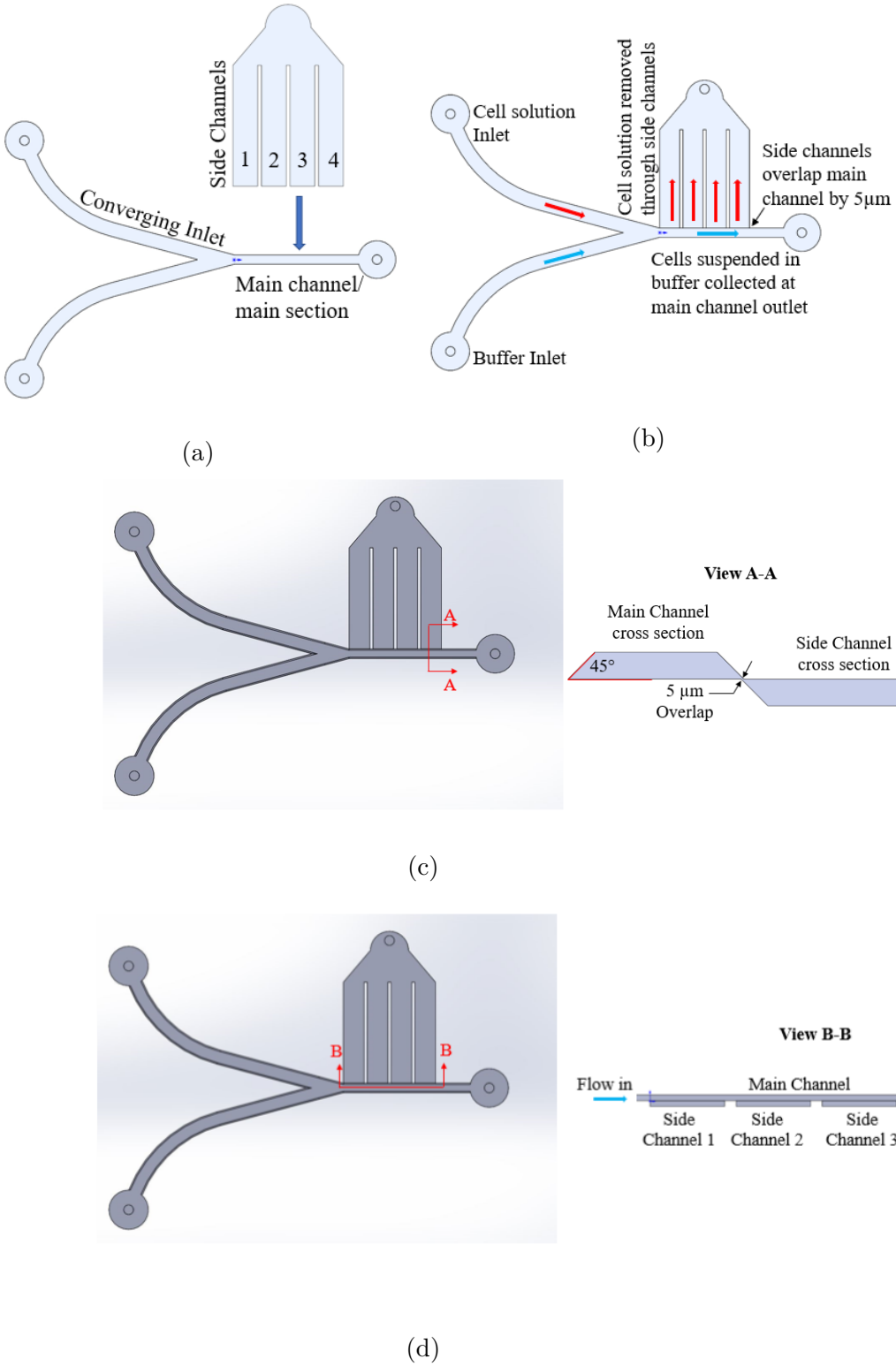

Figure 2.1: Design of the buffer exchange device. (a) The two layers of the device. (b) Fluid flow path in the assembled device. (c) Cross sectional view of main and side channel overlap. (d) Side view of the device showing main and side channel alignment

The side channel is aligned perpendicular to the main channel in such a way that the side channel overlaps the main channel by 5 µm. Figure 2.3 shows the positioning of the side channel and its overlap with the main channel. The width of each side channel was designed to be 650 μm and the spacing between the channels was 150 μm. The design of the device was inspired from a similar microfluidic lab-on-a-chip device used for cell separation applications [49] (for details of the device refer to Figure 3.10).

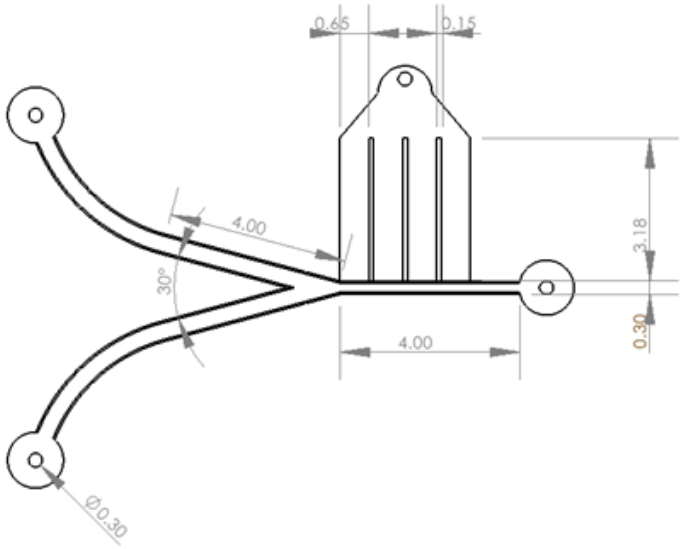

Figure 2.2: Top View with dimensions (in mm) for device with 4 side channels. Channel height: 50 μm

10x Phosphate Buffered Saline (PBS) with a conductivity of 1.1 S/m, which acts as a biological buffer, and de-ionized (DI) water with conductivity value $6 * 10^{-4}$ S/m are made to flow through those inlets at controlled flowrates of either 3 µL/min or 1.5 µL/min. The flowrates were chosen based on existing data for a high throughput cDEP device, which is assumed to be used downstream of the buffer exchange device [60]. The inlet channels join at the main channel of the device, where the cross-sectional width reduces to 300 μm.

The converging inlet flows, the reduction in the cross section of the channel, and a difference in the flowrate values between the two inlet fluids create a pinching effect in which the DI

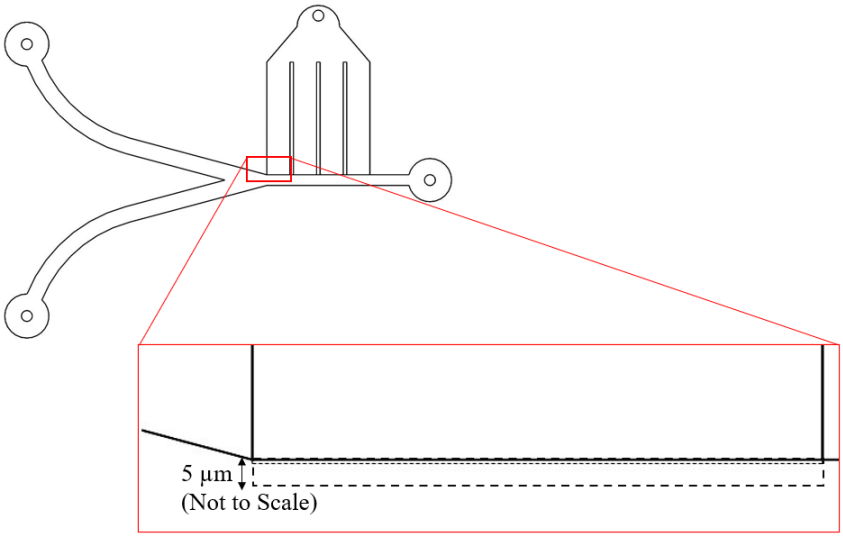

Figure 2.3: Opening between the main and side channels

water pushes the PBS through the side channel. Since the cell diameter is about 20 µm [68], which is four times the width of the opening between the main channel and the side channels, cells get filtered from the PBS and remain suspended in the DI water in the main channel, thus effecting buffer exchange. To prevent cells from clogging the 5 µm wide opening, the walls of the channels are inclined as shown in Figure 2.1c.

The reduction in cross section at the inlet-main channel interface also accelerates the flow along the main channel, causing the DI water and the cells to flow towards the main channel outlet. Circular outlets are designed downstream of both the main channel and the side channels, as shown in Figure 2.4, where 30-gauge PTFE tubing of specified length is attached to both outlets.

The cells, now suspended in DI water, are collected downstream from the main channel outlet for further analysis, such as cDEP experiments.

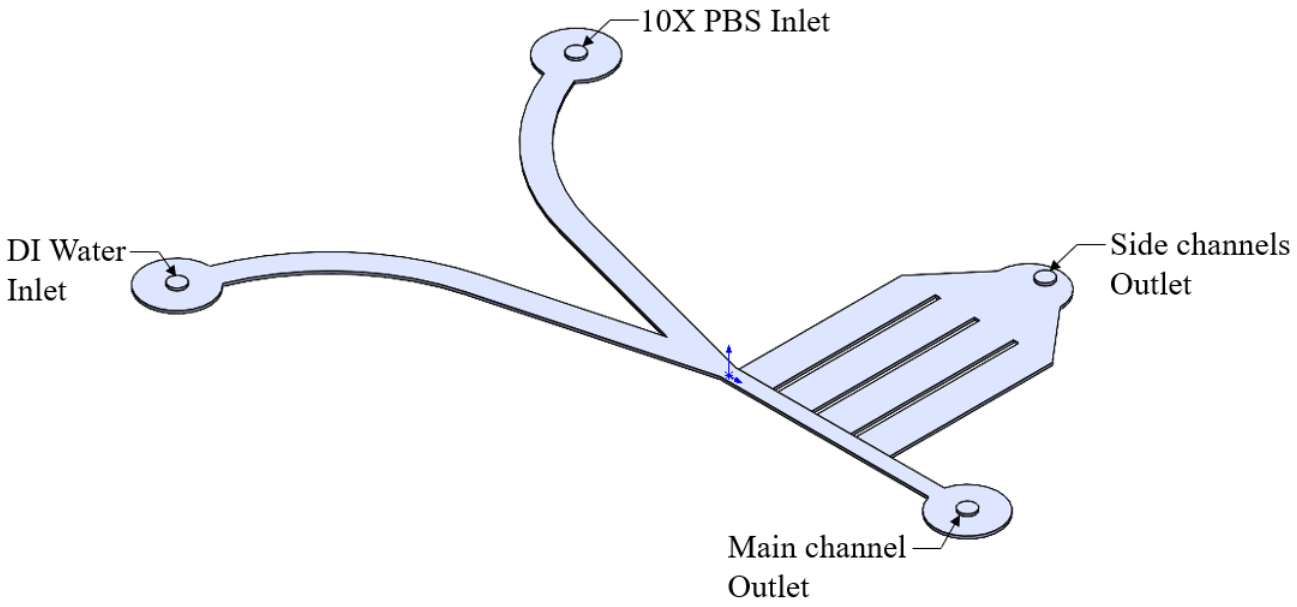

Figure 2.4: Circular Inlets and Outlets for connecting PTFE tubes

2.2 Design Parameters

To find the optimal design for reducing the main channel outlet conductivity and increasing the throughput, four different parameters were considered, namely: number of side channels, total flowrate through the device, flowrate ratio between the two inlets, and side wall angle. Four different configurations based on the number of side channels per device were designed. The different configurations are shown in the Figure 2.5. Figure 2.5a shows a device with one side channel aligned with the main channel as discussed above. Figure 2.5b, Figure 2.5c, Figure 2.5d show the devices with two, three and four side channels respectively. For all the device configurations, irrespective of the number of side channels, a single circular outlet was designed such that all the side channels converged at that outlet.

Three different side wall angles were also designed with the aim of exploring the effect on fluid diffusion, electrical conductivity and overall flow. The three angles chosen, as shown

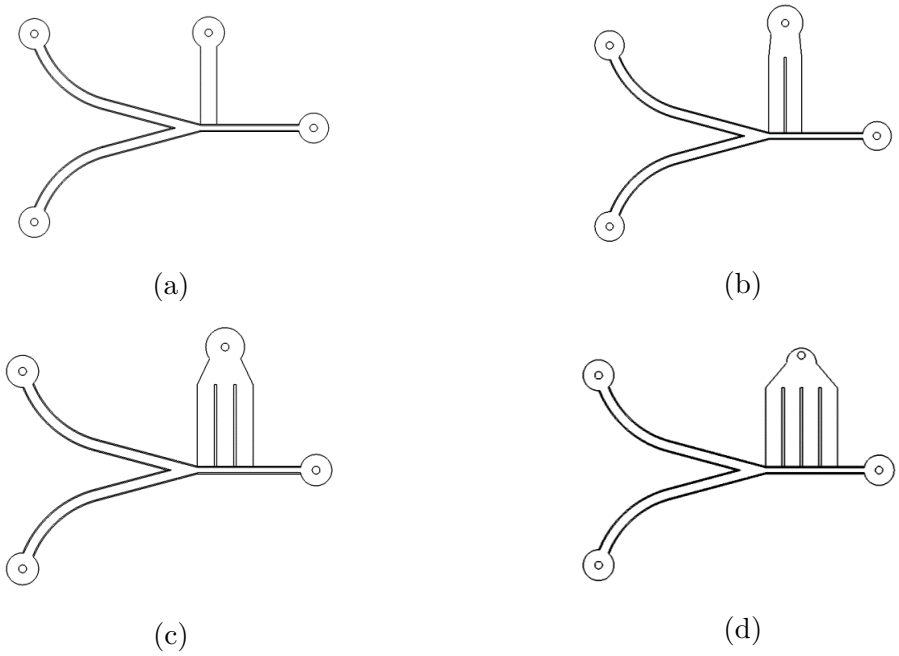

Figure 2.5: The different side channel configurations for a device with 45° wall angle. (a) single side channel. (b) two side channels. (c) three side channels. (d) four side channels

in Figure 2.6, were 45°, 54° and 90°.

The total flowrate of the fluid flowing through the channel, which determined the throughput of the device, was maintained at either 1.5 µL/min or 3 µL/min. Since the two inlet channels converge at the entrance of the main channel, the difference in flowrates between the DI water and the 10x PBS cause the cells to experience shear stress. Two different flowrate ratios between the inlets, 10:1 (DI Water:10x PBS) and 30:1 (DI Water:10x PBS), were chosen to study the effect of flowrate difference on the fluid induced shear stress in the channel and the outlet conductivity. A summary of the design parameters are given in Table 2.1.

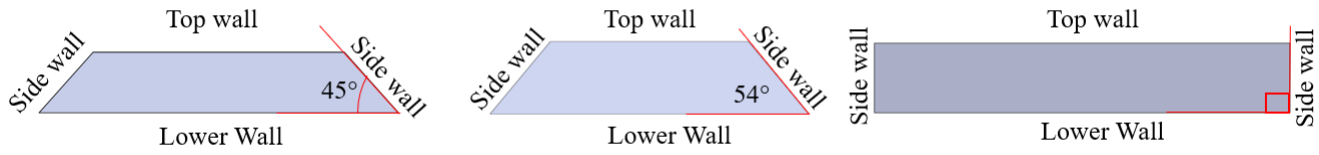

Figure 2.6: Channel Side wall angles

Table 2.1: A summary of design parameters and device configurations considered for analysis.

Parameter	**Variant 1**	**Variant 2**	**Variant 3**	**Variant 4**	**Total No.of Variants**
No.of Side Channels/device	1	2	3	4	4
Total Flowrate (µL/min)	1.5	3			2
Inlet Flowrate Ratio (DI Water : 10X PBS)	10:1	30:1			2
Side Wall Angle (Degrees)	45	54	90		3
Total number of possible device configurations considered					**48**

2.3 Flow Reynolds Number

The Reynolds number represents the nature of the flow inside the channel and serves as an indicator as to whether the flow is laminar or turbulent [57]. The Reynolds number is

$$\mathrm{Re} = \frac{\rho v D_h}{\mu}. \tag{2.1}$$

Here, ρ represents the density of the fluid, v the velocity of flow through the channel and μ the dynamic viscosity respectively. D_h represents the hydraulic diameter of the channel,

which for non circular cross sections is given by

$$D_h = \frac{4A}{P}, \tag{2.2}$$

where A represents the cross sectional area and P the perimeter of the cross section, respectively. The hydraulic diameter of the main channel of the device with 45^o side wall angle was calculated to be 77.95 μm ($7.795 * 10^{-5}$m) based on the dimensions of the cross section shown in Figure 2.7. The viscosity and pressure values were obtained from the literature (refer section 3.1 and Table 3.1 for further details).

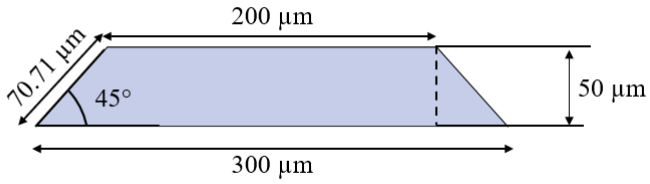

Figure 2.7: Main channel cross section dimensions for a device with 45^o side wall angle

The total flowrate through the main channel was used to calculate the flow velocity. The velocity was calculated using

$$v = \frac{Q}{A}, \tag{2.3}$$

where Q is the volume flow rate through the main channel, A is the cross sectional area and v is the flow velocity in the channel. For a 3 μL/min ($5 * 10^{-11}$m^3/s) flowrate configuration, the average velocity of the fluid through the main channel was found to be 0.004 m/s.

Using the above values for velocity, hydraulic diameter, density, and viscosity in Equation 2.1 gives Re = 0.054. In microchannels of about 250 μm diameter, the onset of turbulence starts

at a Reynolds number of around 1800 [63]. From the above, it can be ascertained that the flow in the device is completely laminar.

Chapter 3

CFD Modeling

3.1 Flow Modeling and Discretization

ANSYS 2020 R1 simulation software was used to perform CFD analysis on the buffer exchange device. The 3D design was imported into the ANSYS Fluent Meshing tool, which was used to generate an unstructured grid in the fluid domain (for meshing details refer to section 3.3). Figure 3.1 shows the mesh used to model the flow field in a straight walled buffer exchange device with 4 side channels.

The mesh was exported into the Fluent software, in which a steady state pressure-based solver was used to model the incompressible flow. Multiple chapters from the ANSYS Theory guide [26] have been used as a reference to construct the computational model; details from this manual are explained in this chapter.

The general mass conservation equation is given by

$$\frac{\partial \rho}{\partial t} + \nabla \cdot (\rho \vec{v}) = S_m, \tag{3.1}$$

where ρ denotes the density of the fluid, $\vec{v}$ represents the velocity of the flow and S_m is a term which denotes the mass added to the continuous phase by user defined sources or a dispersed phase. Similarly, the momentum conservation equation is given by

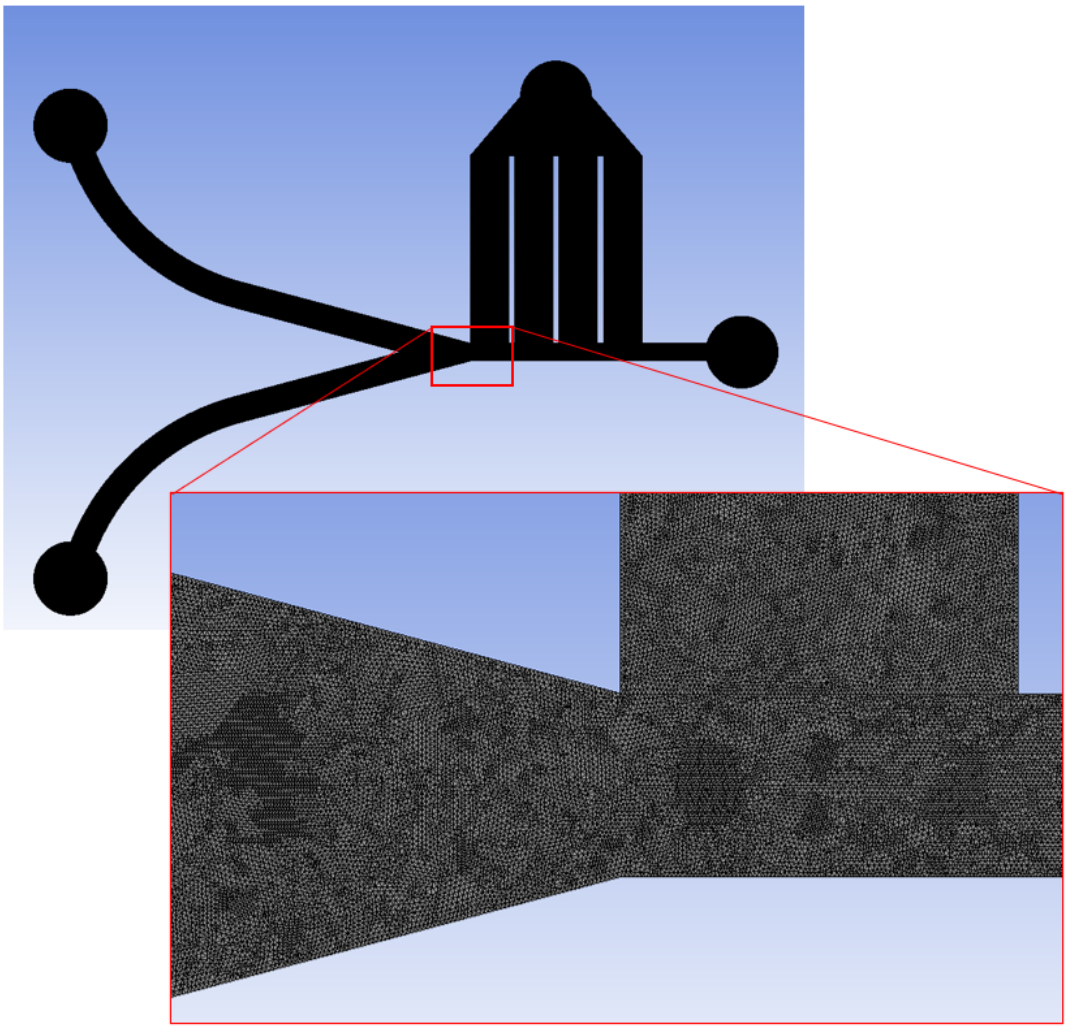

Figure 3.1: Unstructured mesh for the buffer exchange device with four side channels

$$\frac{\partial}{\partial t}(\rho\vec{v}) + \nabla \cdot (\rho\vec{v}\vec{v}) = -\nabla p + \nabla \cdot (\bar{\bar{\tau}}) + \rho\vec{g} + \vec{F}, \tag{3.2}$$

where ∇p denotes the gradient of static pressure in the domain, $\bar{\bar{\tau}}$ denotes the stress tensor which accounts for the viscous forces, and ρg and $\vec{F}$ denote the gravitational body force and external body force terms.

Assuming the fluid is incompressible and the system is operating in steady state, Equation 3.1

and Equation 3.2 reduce to

$$\nabla \cdot (\vec{v}) = 0 \tag{3.3}$$

and

$$\nabla \cdot (\rho \vec{v} \vec{v}) = -\nabla p + \nabla \cdot (\overline{\overline{\tau}}) + \rho \vec{g} + \vec{F}. \tag{3.4}$$

In integral form these equations are written as

$$\oint \rho \vec{v} \cdot d\vec{A} = 0 \tag{3.5}$$

for the continuity equation and

$$\oint \rho \vec{v} \vec{v} \cdot d\vec{A} = -\oint pI \cdot d\vec{A} + \oint \overline{\overline{\tau}} \cdot d\vec{A} + \int_V \vec{F} dV \tag{3.6}$$

for the momentum equation. Here $d\vec{A}$ represents a differential element of the face area through which mass flux occurs and dV the differential element of the control volume. I denotes the identity matrix. For an arbitrary control volume V, the scalar transport for a variable φ is written as

$$\int_V \frac{\partial \rho \varphi}{\partial t} dV + \oint \rho \varphi \vec{v} \cdot d\vec{A} = \oint \Gamma_\varphi \nabla \varphi \cdot d\vec{A} + \int_V S_\varphi dV, \tag{3.7}$$

where Γ_φ is the diffusion coefficient of φ, $\nabla \varphi$ is the spatial gradient of φ, and S_φ is the source term. Equation 3.7 is applied to each cell in the domain and discretized using Equation 3.8, giving

$$\frac{\partial \rho\varphi}{\partial t}V + \sum_{f}^{N_{\text{faces}}} \rho_f \vec{v}_f \varphi_f \cdot \vec{A}_f = \sum_{f}^{N_{\text{faces}}} \Gamma_\varphi \nabla\varphi_f \cdot \vec{A}_f + S_\varphi V, \tag{3.8}$$

where N_{faces} is the number of faces enclosing the cell, φ_f is the value convected through face f, $\rho_f \vec{v}_f \cdot \vec{A}_f$ represents the mass flux, $\vec{A}_f$ is the face area vector, $\nabla\varphi_f$ represents the face gradient, and V is the cell volume.

A linearized form of Equation 3.8 is written as

$$a_P\varphi = \sum_{nb} a_{nb}\varphi_{nb} + b, \tag{3.9}$$

where the subscript nb refers to the neighboring cells, and a_p and a_{nb} are linearized coefficients.

The viscous laminar model was used in the simulations of flow through the buffer exchange device, since flow Reynolds number was less than 1 (refer to section 2.3 for details). The 10x PBS and DI water were modeled based on their properties including density [45], specific heat [8] [71], thermal conductivity [20], viscosity [1] and electrical conductivity [56] (see Table 3.1 for property values).

The species transport model predicts the local mass fraction of each species, Y_i, by solving

$$\frac{\partial}{\partial t}(\rho Y_i) + \nabla \cdot (\rho \vec{v} Y_i) = -\nabla \cdot \vec{J}_i + R_i + S_i \tag{3.10}$$

iteratively. This model was used to create a mixture template containing the two fluids. Here R_i is the net rate of production of the species through chemical reaction, S_i is the rate of creation through the dispersed phase and $\vec{J}_i$ is the diffusive flux due to the concentration gradient. Volume and mass weighted mixing laws were used to define the resulting diffusion

Table 3.1: Properties of DI Water and 10x PBS

Properties	DI-Water	10x PBS	Units
Density	998.20	1005.30	kg/m^3
Specific Heat	4182.00	4148.00	J/kg.k
Thermal Conductivity	0.58	0.60	W/mk
Viscosity	0.00577	0.00102	kg/ms
Molecular Weight	18.02	18.02	kg/mol
Electrical Conductivity	0.0006	1.10	S/m

between the interacting fluids.

Since the flow is laminar, the mass diffusivity was defined through a constant dilute approximation or Fick's Law [77], which is used to model the mass diffusion due to the presence of a concentration gradient. Under this assumption, the diffusion flux is solved using

$$\vec{J_i} = -\rho D_{i,m} \nabla Y_i - D_{T,i} \frac{\nabla T}{T}, \tag{3.11}$$

where $D_{i,m}$ and $D_{T,i}$ are the mass and thermal diffusion coefficients of species i, respectively.

It is assumed that there is no temperature difference between the two fluids, and that no heat is generated because the flow velocity is low (refer to section 2.3 for details), which causes the temperature distribution to be homogeneous throughout the domain. This reduces the temperature gradient ∇T term to zero, and Equation 3.11 becomes

$$\vec{J_i} = -\rho D_{i,m} \nabla Y_i. \tag{3.12}$$

To model the electrical conductivity of the fluids, the potential equation, written as

$$\nabla \cdot (\sigma \nabla \varphi) = 0, \tag{3.13}$$

was used. Here, φ represents the electric potential and σ represents the ionoc conductivity in the fluid zone. Since there is no Joule heating, the sources term in the general form of the equation reduces to zero, so it is not included in Equation 3.13.

A uniform velocity boundary condition was specified at both fluid inlets. Since the area of the inlets was a constant, the velocity values were used as a representation of fluid flowrate through each of the inlet channels. A pressure boundary condition was used for the outlets, with the value of the gauge pressure determined to emulate the presence of additional downstream components, namely the outlet tubing and the cDEP device, with reasonable accuracy. Figure 3.2 shows the complete lab-on-chip setup, including the components downstream of the main and side outlets and the dimensions of the cDEP device and the polytetrafluoroethylene (PTFE) tubing.

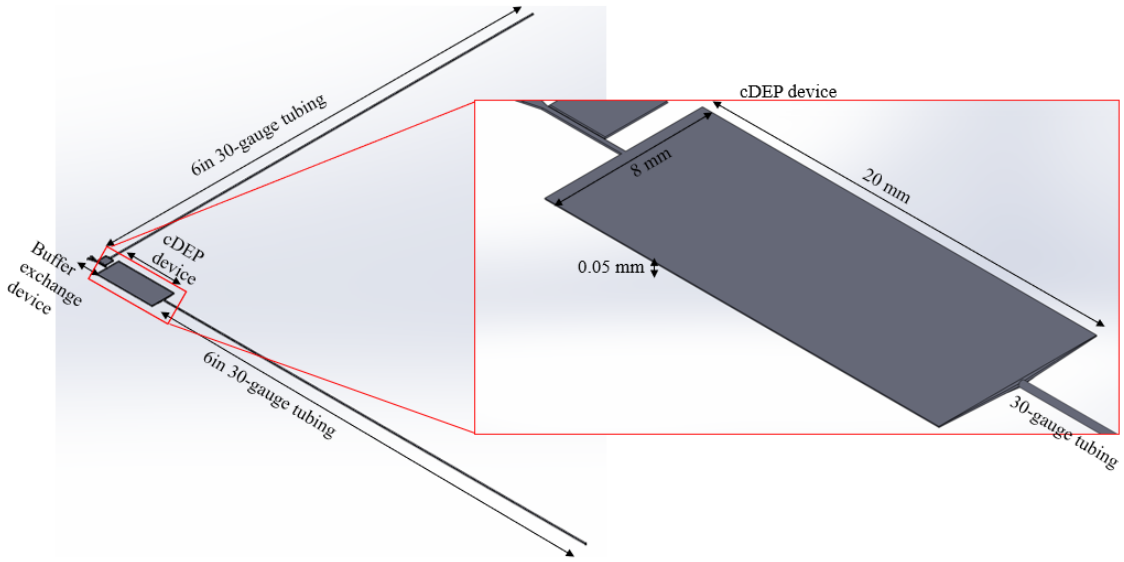

Figure 3.2: The complete microfluidic lab-on-a-chip system containing the buffer exchange device, cDEP device and the PTFE tubing

The pressure at the main channel outlet is the cumulative pressure drop in the cDEP device and the PTFE tubing, which can be represented as

$$P_{Main\ Outlet} = \Delta P_{cDEP} + \Delta P_{Tubing}. \tag{3.14}$$

The pressure at the side channel outlet is only the pressure drop value across the tubing, which is given by

$$P_{Main\ Outlet} = \Delta P_{Tubing}. \tag{3.15}$$

For determining the pressure drop across the 6in 30-gauge tubing, the Hagen-Poiseuille equation [67], given as

$$Q = \frac{\pi D^4 \Delta P}{128 \mu L}, \tag{3.16}$$

was used. Here Q represents the flowrate through the tube, D the diameter, L the length of the tube, ΔP the unknown pressure drop across the tube, and μ the dynamic viscosity of the fluid. Since the flowrate was known, Equation 3.16 was modified to be

$$\Delta P = \frac{128 \mu L Q}{\pi D^4}, \tag{3.17}$$

from which the pressure drop across the tube was determined.

The cDEP device was modeled as a rectangular channel, and the pressure drop was calculated using the Dirichlet solution for fully developed flow through a rectangular duct, which is given by [82]

$$Q = \frac{4ba^3}{3\mu}\left(-\frac{\Delta P}{L}\right)\left[1 - \frac{192a}{\pi^5 b}\sum_{i=1,3,5,\ldots}^{\infty}\frac{\tanh(i\pi b/2a)}{i^5}\right], \tag{3.18}$$

where Q is the flowrate, a and b represent the half width and half height of the channel, ΔP is the pressure drop across the channel and L is the length of the channel considered. Equation 3.18 was rearranged to give

$$\Delta P = \frac{3\mu LQ}{\left[1 - \left(\frac{192a}{\pi^5 b}\right) \sum_{i=1,3,5}^{\infty} \frac{\tanh\left(\frac{i\pi b}{2a}\right)}{i^5}\right] 4ba^3}, \tag{3.19}$$

which determines the pressure drop value. From existing data, it was observed that the pressure drop across an actual cDEP chip is almost twice that of the analytical result owing to the presence of micropillars inside the device. Thus the pressure drop across the cDEP chip was taken to be twice the ΔP value obtained from Equation 3.19.

Using Equation 3.9, the x - momentum equation is discretized by setting $\varphi = u$, giving

$$a_P u = \sum_{nb} a_{nb} u_{nb} + \sum p_f A \cdot \hat{l} + S. \tag{3.20}$$

If the pressure and mass fluxes are known, the velocity field can be obtained. However, since the pressure field is not readily known, a coupled scheme was used for the pressure-velocity coupling, which enabled solving for mass and momentum variables in the Navier-Stokes equation simultaneously through fully implicit coupling of mass flux and pressure gradient in the momentum equation. Although this method is computationally expensive, the results have better accuracy compared to segregated pressure-based solution algorithms [26].

A Second-Order Upwind scheme was used for interpolating the cell center data to the faces of the control volume. This method is more robust than first order schemes when working with unstructured tetrahedral meshes for which the flow is not aligned with the grid. The higher-order accuracy is achieved through the Taylor series expansion of the cell-centered

solution about the centroid [5]. The face value $(\varphi_f)_{SOU}$ is calculated using

$$(\varphi_f)_{SOU} = \varphi + \nabla\varphi \cdot \vec{r}, \tag{3.21}$$

where φ and $\nabla\varphi$ are the cell center value and the gradient in the upstream cell, respectively and $\vec{r}$ is the displacement vector.

To evaluate the gradients of diffusive flux and velocity derivatives in higher order discretization schemes, the Least-Squares Cell-Based method was used since it yields more accurate results than the Green-Gauss Cell-Based method for unstructured grids.

For the implementation used in this work, the change in cell value between two adjacent mesh cells c_0 and c_i is given by

$$\nabla(\varphi_{c0}) \cdot \Delta r_i = (\varphi_{ci} - \varphi_{c0})\,. \tag{3.22}$$

The gradient is computed as the product of a weight factor W and the difference vector $(\varphi_{c1} - \varphi_{c0})$. For a three-component system this is written as

$$(\varphi_{c0})_k = \sum_{i=1}^{n} W_{i0}^k \cdot (\varphi_{ci} - \varphi_{c0})\,, \tag{3.23}$$

where k represents the x, y or the z component.

Finally, the Hybrid Initialization method was used to initialize the solution with the Laplace equation being solved to determine the velocity and pressure fields. The Laplace equation for velocity is written as

Table 3.2: Summary of the computational setup

S.No	Solver Schemes	Effect on the computational Setup
1	Steady State Solver	Eliminates time dependent variables
2	Pressure based solver	Models incompressible flow
3	Viscous Laminar Model	Uses the low Reynolds Number assumption for solving Navier Stokes equation
4	Species Transport Model	Defines the mass diffusion and flow physics between two interacting species
5	Potential Equation	Models ionic conductivity between diffusing fluids
6	Coupled Scheme	High accuracy pressure-velocity coupling
7	Second order Upwind	Interpolates the cell centered data to the faces of control volume
8	Least Square Cell Based Method	Evaluates gradients of diffusive flux and velocity derivatives
9	Hybrid Initialization	Solves Laplace Equation to initialize the velocity and pressure fields

$$\nabla^2 \varphi = 0, \tag{3.24}$$

where the gradient of the velocity potential φ is used to determine the velocity components. The Laplace equation for pressure is given by

$$\nabla^2 P = 0, \tag{3.25}$$

which is used to produce a smooth pressure field in the domain.

A summary of the solution methods and techniques used can be found in Table 3.2.

3.2 Discrete Phase Modeling

For modeling particle motions inside the channel, Discrete Phase Modeling (DPM) was used. This was done with the aim of comparing the computed particle trajectories with the experimental results presented in the literature, as explained in subsection 3.4.2.

In this model the particles are assumed to be point masses such that their entire mass is concentrated at their center of gravity. Spherical polystyrene (PS) particles of 2 μm diameter and ellipsoidal PS particles of 4 μm diameter were considered for modeling since they were used in the literature [48]. The numerical model is explained below.

DPM is a Euler-Lagrange approach in which the fluid is treated as a continuum for solving the Navier-Stokes equations, and forces acting on the particle are integrated to predict the particle trajectory in the fluid.

The particle force balance in the Lagrangian frame is written as

$$m_p \frac{d\vec{u}_p}{dt} = m_p \frac{\vec{u} - \vec{u}_p}{\tau_r} + m_p \frac{\vec{g}\,(\rho_p - \rho)}{\rho_p} + \vec{F}, \tag{3.26}$$

where m_p and $\vec{u}_p$ denote the particle mass and particle velocity, $\vec{u}$ is the fluid velocity, and ρ and ρ_p are density of the fluid and density of the particle, respectively. τ_r is the particle relaxation time written as

$$\tau_r = \frac{\rho_p d_p^2}{18\mu} \frac{24}{C_d \mathrm{Re}}, \tag{3.27}$$

where μ denotes the viscosity, C_d the coefficient of drag of the particle and d_p is the particle diameter. Here Re is the relative Reynolds number, which is computed as

$$Re \equiv \frac{\rho d_p \left|\vec{u}_p - \vec{u}\right|}{\mu}. \tag{3.28}$$

In Equation 3.26, $\vec{F}$ denotes the additional forces that act on the particle as described below. The ρ/ρ_p value approaches unity, which means that the density of the particle approaches the fluid density. The fluid experiences an acceleration when flowing around the particle, and the forces associated with this acceleration are represented as virtual mass and pressure gradient forces. The virtual mass force is given by

$$\vec{F_{vm}} = \frac{1}{2} m_p \frac{\rho}{\rho_p} \left(\vec{u}_p \nabla \vec{u} - \frac{d\vec{u}_p}{dt} \right). \tag{3.29}$$

The additional force arising due to the pressure gradient in the fluid is written as

$$\vec{F_{PG}} = m_p \frac{\rho}{\rho_p} \vec{U} \nabla \vec{u}. \tag{3.30}$$

Additionally, the particles experience a lift force due to shear [59], and the generalized form of that force is given by

$$\vec{F_{SL}} = m_p \frac{2Kv^{1/2}\rho d_{ij}}{\rho_p d_p \left(d_{lk} d_{kl}\right)^{1/4}} \left(\vec{u} - \vec{u}_p\right), \tag{3.31}$$

where d_{ij} is the deformation tensor and K takes the value 2.594 for small particles with diameter in the range of a few microns [38]. The combination of forces in Equation 3.29, Equation 3.30 and Equation 3.31 gives the cumulative additional force $\vec{F}$ acting on the particle in Equation 3.26.

Inert PS particles were modelled with a density of 1053 kg/m^3 [62]. Different drag laws in

the literature were used to model the drag coefficient C_d in Equation 3.27 based in the shape of the particle. For the 2 μm spherical particles, the Morsi Alexander drag law [43] was used for which the drag coefficient is given by

$$C_D = a_1 + \frac{a_2}{Re} + \frac{a_3}{Re^2}. \tag{3.32}$$

Here, a_1, a_2 and a_3 are constants over a varying Reynolds number range. Owing to the difference in shape of the 4 μm particles, a non spherical drag law developed by Haider and Levenspiel [19] was used, with the drag coefficient defined as

$$C_D = \frac{24}{Re_{sph}}\left(1 + b_1 Re_{sph}^{b_2}\right) + \frac{b_3 Re_{sph}}{b_4 + Re_{sph}}. \tag{3.33}$$

The b_1, b_2, b_3 and b_4 values are determined by the shape factor φ, which is written as

$$\varphi = \frac{s}{S}. \tag{3.34}$$

In Equation 3.34, S denotes the actual surface area of the particle and s denotes the surface area of a sphere that has the same volume as the particle. It was observed from the literature that was being used as a reference [48], that the disc shaped particles are an oblate spheroid. The volume of the oblate spheroid was calculated as

$$V = \frac{4}{3} \cdot \pi \cdot (\mathrm{b})^2 \cdot \mathrm{c}, \tag{3.35}$$

where V denotes the volume, b denotes the semi major axis and c the semi minor axis. Knud Thomsen's formula was used to estimate the surface area S of the oblate spheroid as

$$S = 4 \cdot \pi \left(\frac{b^{2p} + 2b^p c^p}{3} \right)^{1/p}. \tag{3.36}$$

Here p takes the value 1.6075. The value of p is determined such that surface area value has the least relative error. The value of shape factor S for the 4 μm particle was found to be 0.9144 .

3.2.1 A note on the DPM

Since the particles are considered as point masses in this model, the presence of a solid particle boundary of a specified diameter is not taken into account in Fluent while calculating the trajectories of the particles. This simplification causes the particles to enter orifices that are smaller in size than the diameter of the particle itself.

In subsection 3.4.2, it is shown that DPM gives an accurate representation of particle positions. This accuracy can be attributed to the fact that, when the flowrate in the channel is sufficiently high, the particles have enough momentum that most of them carry on past the side channels. Since the flowrate through the device in subsection 3.4.2 is relatively high, at about 25 μL/min ($4.17 * 10^{-10}$m^3/s), the particles modelled via DPM possess enough momentum to reach the outlet of the expanding section. The velocity in the channel is calculated based on Equation 2.3, in which the A takes the value of the cross sectional area of the above channel used for validation. The cross sectional area was calculated to be 75 μ m^2 ($7.5 * 10^{-11}$m^2) and the resulting flow velocity was found to be 5.5 m/s. The mass of the PS particles that is being modeled is $5.52 * 10^{-13}$kg. The average momentum of the particle in the channel is $3 * 10^{-12}$ kgm/s.

However, in the proposed device, the maximum flowrate is maintained at only 3 μL/min.

Additionally, the cross sectional area of the channel is about 10 times larger that of the device used in subsection 3.4.2. Both these factors cause the velocity inside the channel to drop significantly. The average velocity of particles in the main channel is 0.004 m/s (refer section 2.3 for details on velocity calculation). The diameter of the PS particles used in the main channel of the buffer exchange device is 4 times that used in the above model, and hence the particle mass increases by 64 times to $353.28 * 10^{-13}$kg. Since the particles are suspended in the fluid, their momentum also reduces significantly to $1.4 * 10^{-13}$ kgm/s, which is a $21X$ reduction in particle momentum as compared to the particles in the smaller channel used in subsection 3.4.2. This reduction in particle momentum combined with the fact that the particles are considered as point masses, causes the particles to exit through the side channels in the model of the proposed device. In the simulations, not even a fraction of the particles reach the main channel outlet since they don't have the momentum to cross the side channels. Hence, it was not possible to use DPM to calculate particle trajectories in the proposed device.

3.3 Grid Independence Study

An unstructured grid was used to mesh the domain since it conforms well with the shape of the boundary and thus is well suited for modeling complicated geometries [81]. Moreover, an unstructured grid enables good control over local grid concentration. Even though a structured grid is well ordered and is easy to generate, as it requires less computational resources, the boundary representation is not accurate for non-rectangular geometries, and this causes the grid to poorly resolve the viscous boundary layer on boundaries [73]. Since the buffer exchange device has angled walls and curved inlets, an unstructured grid was chosen over a structured grid. ANSYS meshing software was used to generate the grid, with

the physics performance parameter set to "CFD" and the growth rate set at 1.2 to prevent high aspect ratios. The mesh smoothing was set at medium to balance computational load and mesh quality.

To verify that there are a sufficient number of mesh cells to accurately resolve the flow, a grid independence study was carried out. The buffer exchange device design with 90° wall angle and four side channels was chosen for this analysis. The outlet electrical conductivity value, which is based on a diffusive quantity, was determined to be the most sensitive variable to grid size. Also, since conductivity was one of the key parameters of interest, it was chosen to test grid independence. The non-dimensional mesh length λ, computed as the ratio of average mesh element size to the hydraulic diameter of the main channel, was used to characterize a given mesh size (refer to section 2.3 and Equation 2.2 for details on hydraulic diameter).

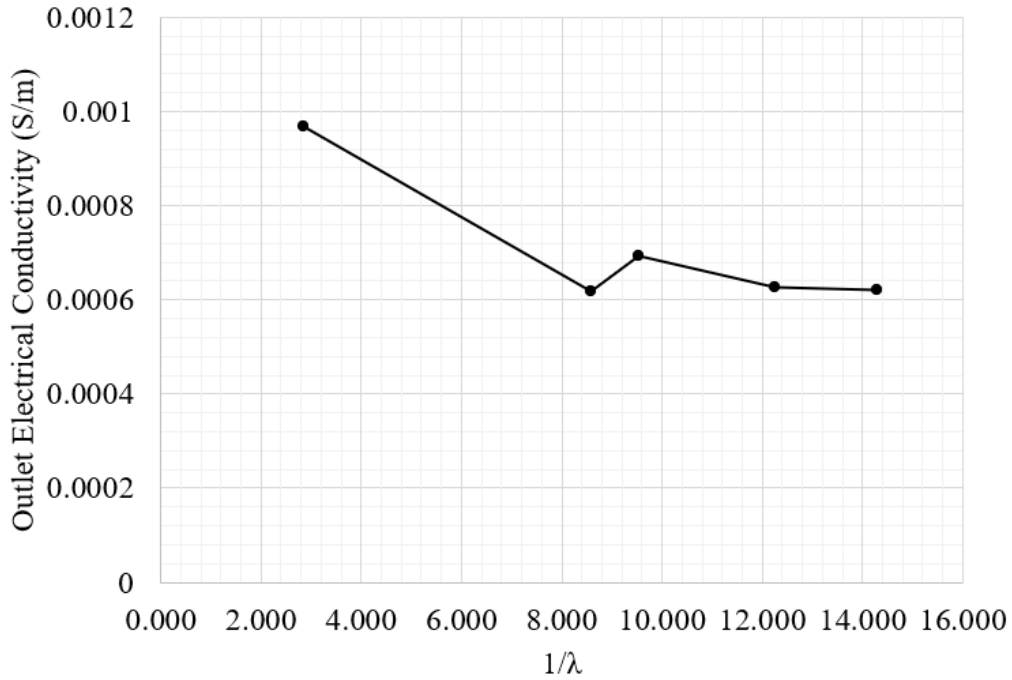

Figure 3.3: Plot of outlet electrical conductivity vs inverse non-dimensional mesh length

From Figure 3.3, it could be observed that the outlet electrical conductivity value reaches

grid independence at $\lambda^{-1} \approx 12$. This corresponds to about 28.28 million mesh cells in the domain. To rule out anomalous results, the side channel flowrate was chosen as a second variable to check grid independence.

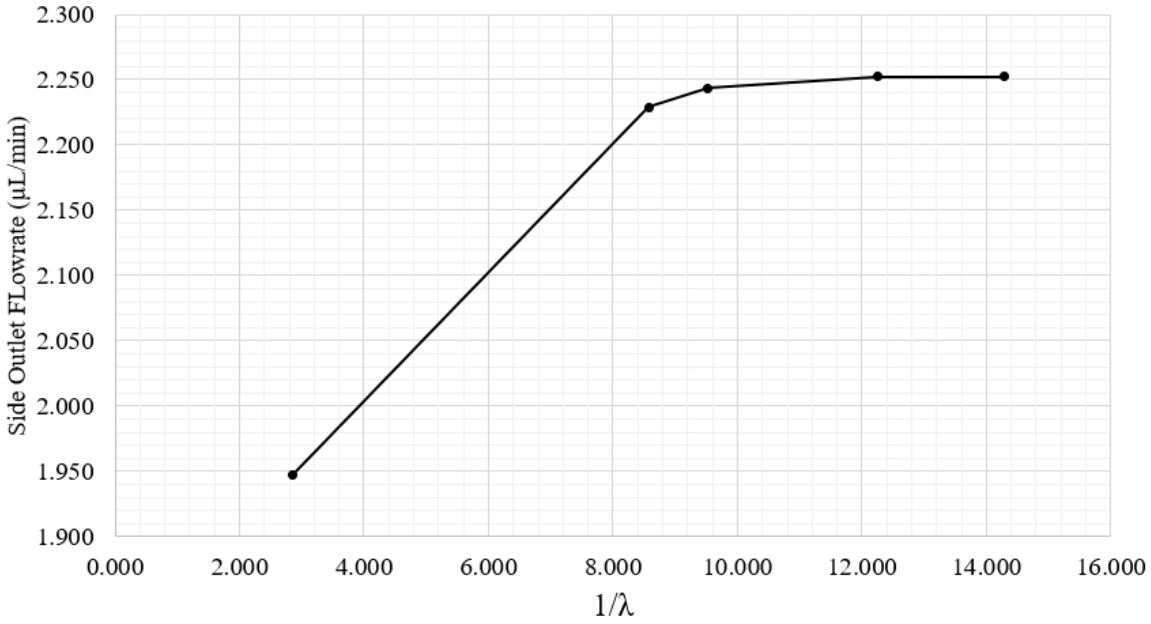

Figure 3.4: Plot of side channel flowrate vs inverse non-dimensional mesh length

By observing Figure 3.4, the side outlet flowrate shows similar grid convergence at $\lambda^{-1} \approx 12$. From Figure 3.5, it can be seen that the percent difference in the electrical conductivity is on the order of 10^{-5} between the mesh with highest resolution and one with the second highest resolution. By combining the results from Figure 3.3, Figure 3.4 and Figure 3.5, it can be ascertained that grid independence is achieved at a $\lambda^{-1} \approx 12$ or a mesh size of around 28.28 million mesh elements.

For the grid independent mesh, Figure 3.6 gives the quality distribution of elements. The average quality is around 0.85 with a standard deviation of 0.094. Since a mesh quality of 0.65 is considered acceptable, the current mesh quality of 0.85 is a very good mesh for modeling the laminar flow in the channel.

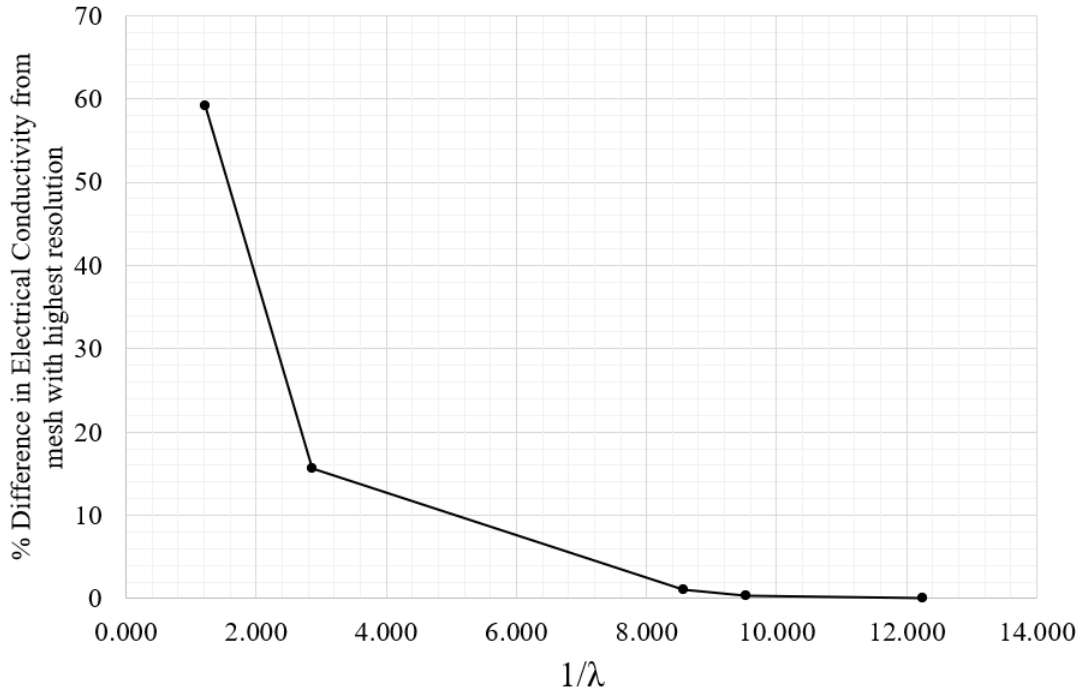

Figure 3.5: Plot of % difference in electrical conductivity from the mesh with highest resolution vs inverse non-dimensional mesh length

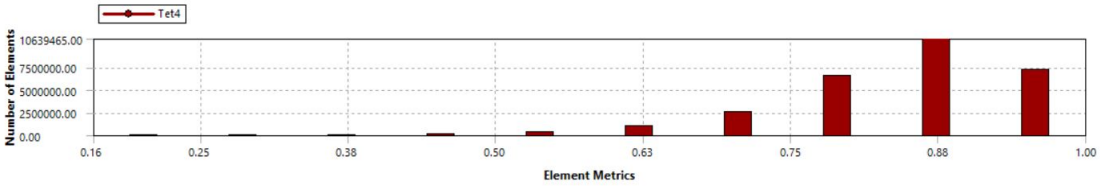

Figure 3.6: Mesh quality distribution for grid independent mesh

Similarly, the aspect ratio distribution is shown in Figure 3.7, where it could be observed that the average value of the mesh aspect ratio was around 1.81 with a standard deviation of 0.45, which is a very good aspect ratio. Furthermore, the average characteristic length was observed to be 4.69 μm for an average element size of 7 μm.

From the above data, it is evident that the grid independent mesh is a robust, high quality mesh. Hence, this mesh setup was used for performing simulations for all the configurations and designs of the buffer exchange device.

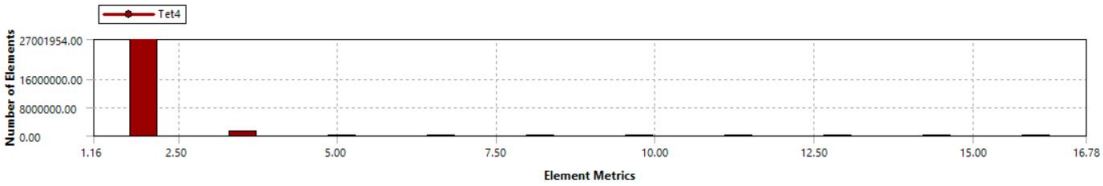

Figure 3.7: Mesh aspect ratio distribution for grid independent mesh

3.4 Computational Model Validation

3.4.1 Residual Convergence

The solution accuracy and residual convergence decide the robustness of the computational model [27]. The number of iterations to be run was determined by the convergence of residuals, while closeness of computational results to the existing experimental and analytical results was used as an indication of correctness of the model used. The solution was considered as converged when it no longer changed significantly with additional iterations, overall mass and momentum balance was achieved, and the residuals dropped at least by 4 orders of magnitude [80] [79].

Figure 3.8 shows the variation of continuity residual values with iteration number. It is observed that the residuals diminish to the order of 10^{-5} within 100 iterations. Similarly, the variation of velocity residuals with iteration number was also monitored. From Figure 3.9, the velocity residuals drop to an order of magnitude of around 10^{-7} within 100 iterations.

One other critical criteria for convergence is the net mass imbalance, which is a representation of numerical error associated with the discretization of the continuity and momentum equations [6]. To study the mass imbalance, the net inlet and outlet flowrate values were computed from Fluent, and the difference in these results was found to be less than 0.1%. From the above results, it was concluded that, for the grid independent mesh, the solution

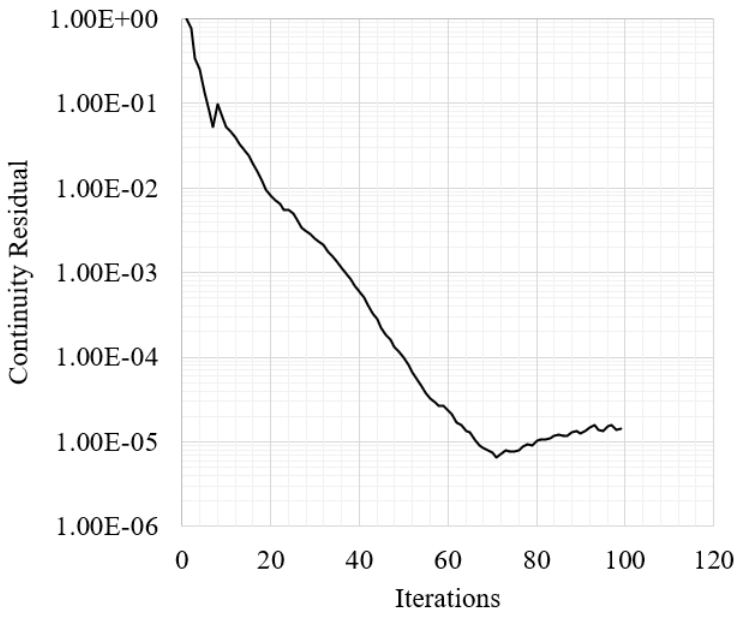

Figure 3.8: Convergence of continuity residuals with iterations

converges within 100 iterations.

3.4.2 Validation with Experimental Work Present in Literature

A microfluidic device with a similar design, known as a Tilted-wall Pinched Flow Fractionation device (t-pff-v), has been used for particle and cell separation and extraction [48]. The device design and dimensions are shown in Figure 3.10. This device is used as a passive cell separation tool, relying on microfluidic forces and particle interaction with the channel as opposed to relying on external forces such as acoustic [35] or magnetic fields [51], which could be harmful to the cells [61].

Passive size separation is achieved by the steric exclusion effect at the walls [3], and the expanding/broadened segment of the device enhances the separation that originally occurs in the main channel. The vertical focusing channels help in aligning the cells with the wall, and the tilted side walls prevent cell agglomeration and clustering by enhancing horizontal

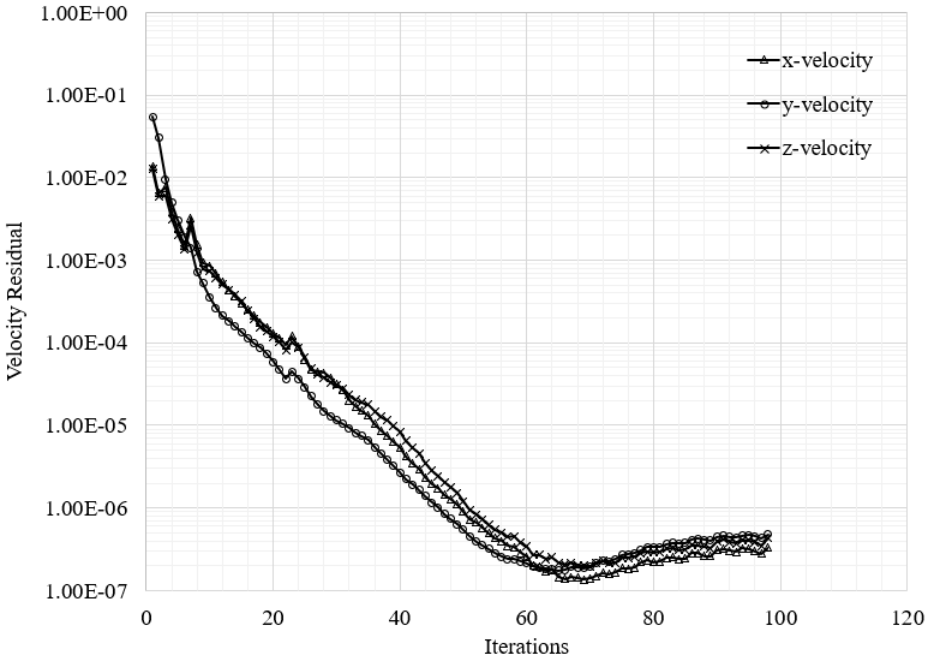

Figure 3.9: Convergence of velocity residuals with iterations

separation [47].

For this experimental study, spherical and disk shaped polystyrene (PS) particles were used as a representation of platelets and red blood cells (RBCs) [49]. The buffer flowrate was 30 times that of the particle-laden biofluid flowrate. The flow parameters, fluid properties and particle dimensions used in the experiment are given in Table 3.3.

Table 3.3: Experimental parameters and properties used in the literature

Parameter/Property	**Value**	**Units**
Solution Flowrate	50	μL/hour
Buffer Flow Rate	1500	μL/hour
Fluid Density	1055.1	kg/m^3
Dynamic Viscosity	0.001728	Ns/m
Fluid Temperature	298	k
Spherical PS Particle Diameter	2	μm
Disk Shaped PS Particle Diameter	4	μm

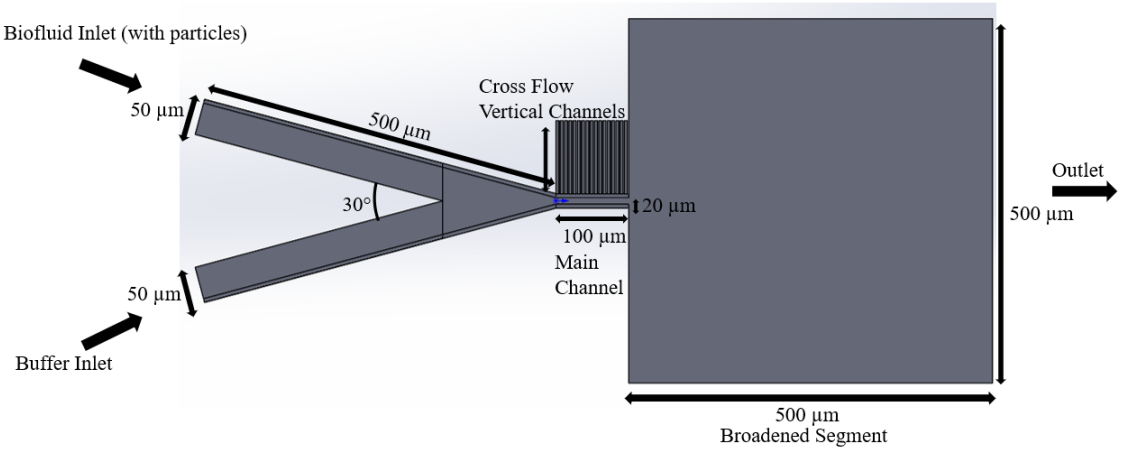

Figure 3.10: t-pff-v lab on chip device for size based cell separation. Height of the device: 5.6 μm. Side walls tilted at 45^o. Adopted from [48]

The computational setup explained in chapter 3 was used to model the flow in this device. In addition, the particle motion was modelled using the Discreet Phase Model (DPM) in Fluent as discussed in section 3.2.

An unstructured grid with 31 million elements was used to run the simulation. The DPM model was used as a post processing step once the velocity field was resolved by Fluent. The outlet of the broadened section, which was 300 μm in width, was divided into 31 equally spaced imaginary bins for every 10 μm and the percentage of the total particles passing through each of the bins was noted. The percentage frequency of the particles passing through the bins was plotted against their position in the outlet, which is shown in Figure 3.11.

Good agreement is observed between the computational and experimental results with regards to the particle position, frequency, and separation in the broadened section outlet.

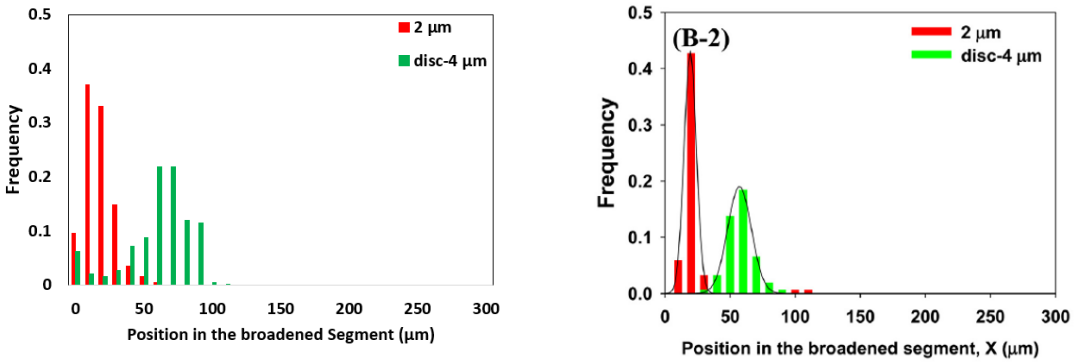

(a) (b)

Figure 3.11: Comparison between particle positions in the broadened outlet section between (a) Fluent DPM Result (b) Experimental result from [49]

3.4.3 Comparison with Analytical Data

The device used in subsection 3.4.2 was then scaled by 9X in size since the size of cancer cells is around 20 μm [68], which is about 10 times the size of the particles considered in the t-pff-v device in the literature. The numerical setup and meshing was based on chapter 3 and section 3.3 respectively. The values of molar concentration and electrical conductivity at the broadened section outlet were observed.

The relation between electrical conductivity (EC) and total dissolved salts (TDS) in a solution is given by

$$\mathrm{TDS}\left(\frac{\mathrm{mg}}{\mathrm{L}}\right) = \mathrm{k} \times \mathrm{EC}\left(\frac{\mu\mathrm{S}}{\mathrm{cm}}\right), \tag{3.37}$$

where k is a coefficient whose value depends on the number of ions in the solution [56]. For DI water, the value of k is approximately 0.5 [78]. However, its value increases to 0.65 for salt solutions similar to the biological buffer [22].

The concentration data from Fluent, which is given in mol/L, was converted to mg/L to

obtain the TDS value. The conversion is given by

$$\frac{\text{mol buffer}}{L \text{ solution}} \times \frac{\text{molNaCl}}{\text{mol buffer}} \times \frac{58.44 \text{ gNaCl}}{1 \text{ molNaCl}} \times \frac{1000\text{mg}}{g} = \frac{\text{mgNaCl}}{L \text{ solution}}. \tag{3.38}$$

Once the outlet concentration values were converted to TDS, the EC values were calculated for the salt solution based on Equation 3.37. The electrical conductivity for the salt solution and DI water mixture at the broadened section outlet was calculated as

$$EC \text{ solution } = \frac{TDS}{k} + EC \text{ deionized water } . \tag{3.39}$$

The calculated conductivity values at the broadened section outlet were compared with the values of EC obtained directly from Fluent, and the % error between the two are shown in Figure 3.12.

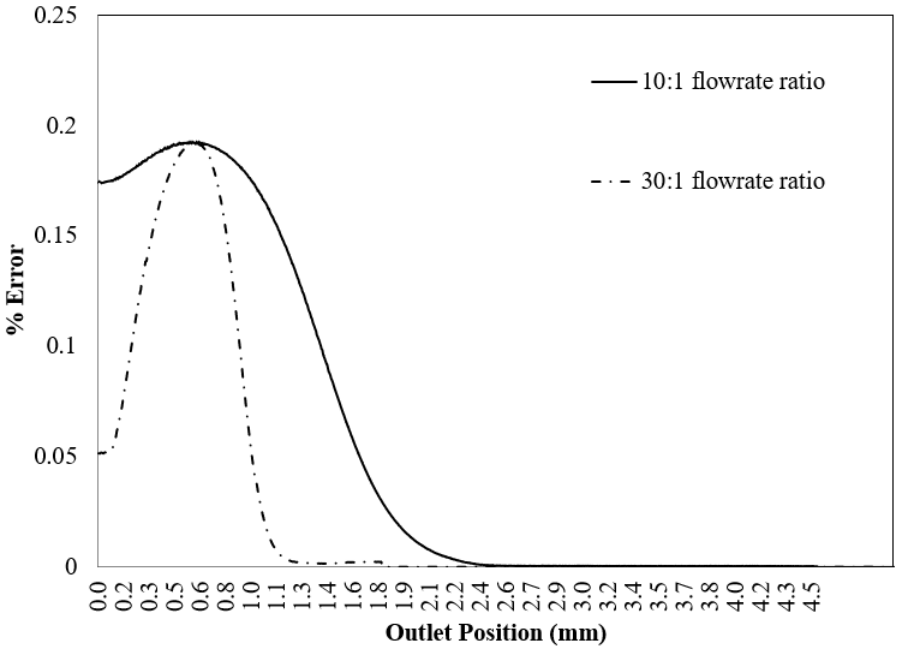

Figure 3.12: Comparison of the % error between the manual and numerical solution of EC values at the outlet

It was observed that the error between the two solutions was less than 0.17%.

From residual convergence and the literature-based experimental comparison, it was ascertained that the computational model was robust.

Chapter 4

Results and Discussion

The effectiveness of the buffer exchange device was defined based on three parameters:

- the electrical conductivity at the main channel outlet,
- the shear stress generated in the device, and
- the flowrate exiting from the main channel, or the throughput of the system that is delivered to the downstream cDEP system.

A parametric study was performed to analyse the effect of geometry, input flowrate and wall angle on the device effectiveness. An ideal buffer exchange device would have the least shear stress with maximum throughput and lowest electrical conductivity at the main channel outlet. Simulations were run to identify the optimal design configuration for each of these parameters.

The computational model was initialized in the local system through the Fluent Graphical User Interface (GUI). However, since the number of mesh elements exceeded 28 million, and discretizing the Navier-Stokes equation and solving for mass, momentum, diffusion, and energy at every node was computationally intensive, the simulation was run on the BEAM High Performance Cluster. The case and data files containing the computational model information were generated locally and uploaded to the cluster. A journal code was written to control the inlet and outlet boundary conditions (BCs) and the number of iterations, and

to automate the data extraction from the simulation at specified intervals. The resulting data was then imported into the local system and analyzed through the local GUI.

4.1 Shear Stress Analysis

Since the two inlet streams in the device have significantly different flowrates, a shear force develops in the interface between the two fluids due to the abrupt change in the velocity gradient [50] in the main channel. This shear force would be experienced by the cells in the biological buffer (10x PBS). In addition to that, when the fluid enters any side channel, it flows from the main channel, which is 300 μm wide, through the overlap gap, which is only 5 μm wide. Such a sudden contraction of flow while moving through this overlap gap causes the shear stress to increase in the fluid [21], which is transmitted on to nearby cells. Finally, any fluid flowing through a microchannel develops shear stress [87], the magnitude of which is determined by the flowrate through the channel and the channel dimensions.

The cells experience the cumulative shear stress induced by all the above factors. Since cells undergo lysis at high shear stress values [55], the system design and parameters were analysed to determine the device with the least flow induced shear stress (FSS) in the channel with the aim of preserving the cells for further downstream analysis using a cDEP device.

The overlap gap is located in the base of the main channel, hence the cumulative shear stress is greater near the lower wall of the channel. Figure 4.1 shows the shear stress contour in the inlet and main channel of the device for a system configuration with 10:1 flowrate ratio and a 1.5 μL/min total flowrate. It can be observed that the maximum value of the shear stress occurs at the overlap between the main channel and the side channels.

Figure 4.2 shows the plane where the shear stress in the channel was quantified. Typical

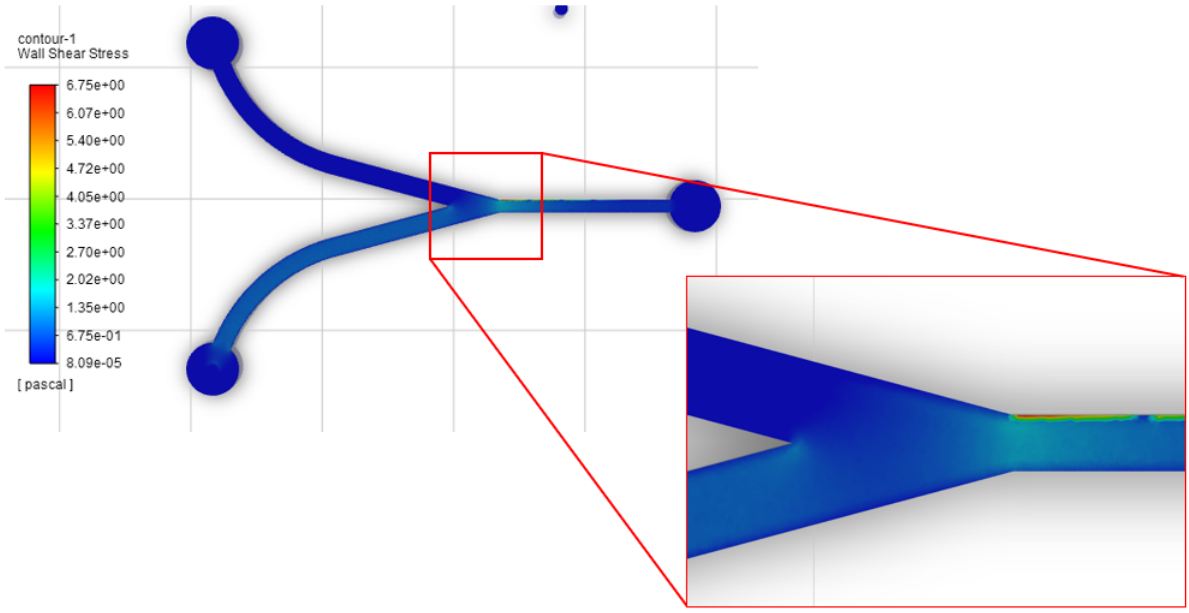

Figure 4.1: Shear stress contour in a plane adjacent to the lower wall of the device in the inlet and main channel

cell trajectories through the main channel will be close to the side wall since the biological buffer is pushed towards this wall by the cDEP buffer. Therefore, a plane 20 μm wide was chosen as shown based on anticipated cell position in the channel. The plane of analysis is 4 mm long and is located 5 μm above the lower wall in the main channel.

The nodal values of shear stress were recorded from Fluent. MATLAB was used to generate a 3D surface plot of the variation of shear stress in the plane. Figure 4.3 shows the shear stress distribution for a straight walled device with four side channels. The peak shear stress value occurs at the areas of overlap between the main channel and the side channel. Moreover, it was also observed that the magnitude of shear stress drops as the flow progresses through the channel. This variation indicates that the maximum flowrate occurs through the first side channel, and the pressure gradient and flowrate through the subsequent side channels

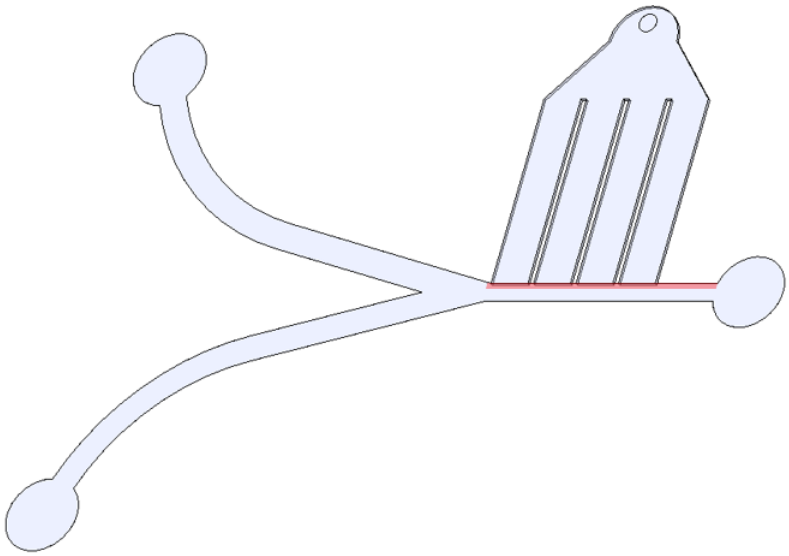

Figure 4.2: The plane adjacent to the lower wall of the main channel, represented in the figure by a red box, where the shear stress is measured

drops off.

The maximum shear stress value recorded in the plane of analysis, as shown in Figure 4.3, was 14.8Pa, and this peak occurred at the initial overlapping point between the main channel and the first side channel. The average shear stress at which a cancer cell undergoes lysis after hours of prolonged exposure is 60 dyne/cm^2 or 6 Pa [55]. Cancer cells are capable of withstanding high shear stress values of up to 3000 dyne/cm^2 or 300 Pa for short exposure times [4]. In the proposed device the average residence time of the cells in the channel is around 6 to 12 seconds. Furthermore, the cell is exposed to the maximum shear stress values at the overlap of the first side channel for less than 0.4 seconds. Hence, there is little chance of lysis in the device. The higher values of shear stress observed at the overlapping region can be attributed to the steep difference in the velocity gradient when the fluid enters the 5 μm orifice.

In biological systems, cancer cells generally experience an average shear stress of 15 dyne/cm^2

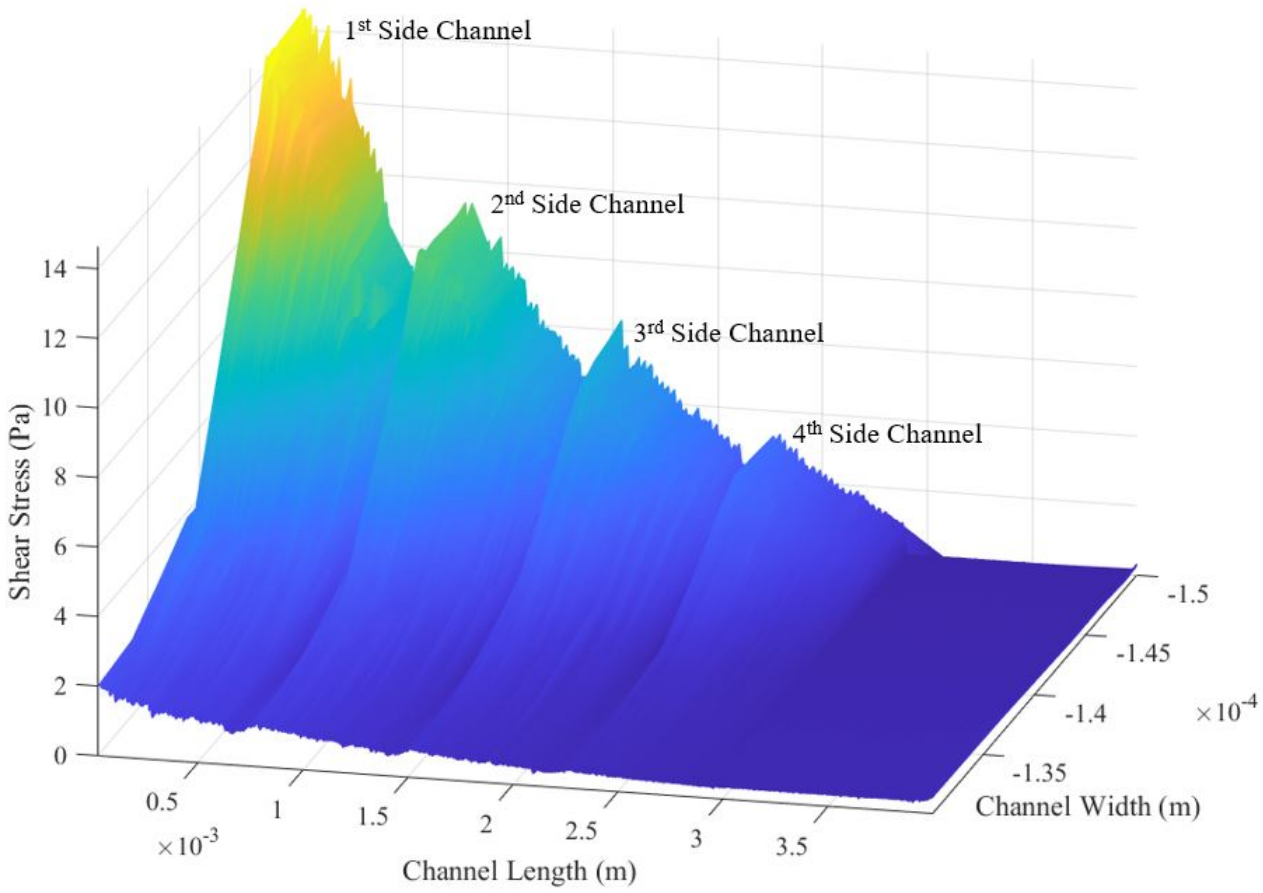

Figure 4.3: Variation of Shear Stress in the plane of analysis in the main channel of the device

or 1.5 Pa for a prolonged duration [13]. The area weighted average of the shear stress in the channel was recorded for all the different device designs and flowrates. A shear stress index $\tau*$ was defined as

$$\tau^* = \frac{\bar{\tau}}{\tau_{sys}}, \tag{4.1}$$

where $\bar{\tau}$ represents the area averaged shear stress value in the device and $\tau_{sys} = 1.5$ Pa is taken as the average shear stress experienced by a cancer cell in a biological system.

Simulations were run in Fluent for a straight walled channel to analyze the effect of different side channel configurations and flowrates on the shear stress index.

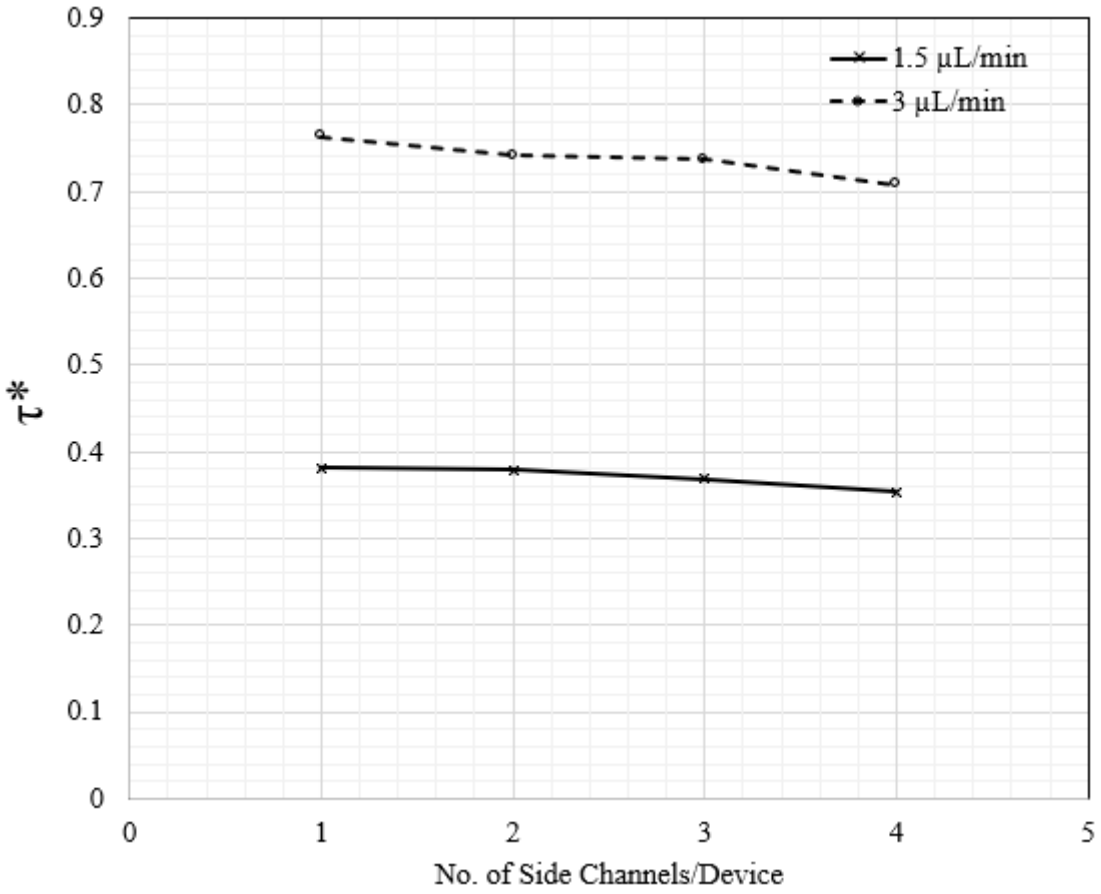

Figure 4.4: Variation of shear stress index with number of side channels for a flowrate ratio of 10:1 between the DI water inlet and the 10xPBS inlet

Figure 4.4 shows the change in shear stress index for different side channel configurations for two different total flowrates. For the higher flowrate value of 3 μL/min the shear stress index is observed to be 2X greater than the 1.5 μL/min flowrate for every side channel configuration of the device. This is inline with what was expected, since it is known that a higher flowrate induces greater shear stress in the channel.

It is also observed that the value of shear stress index reduces with an increase in the number of side channels.

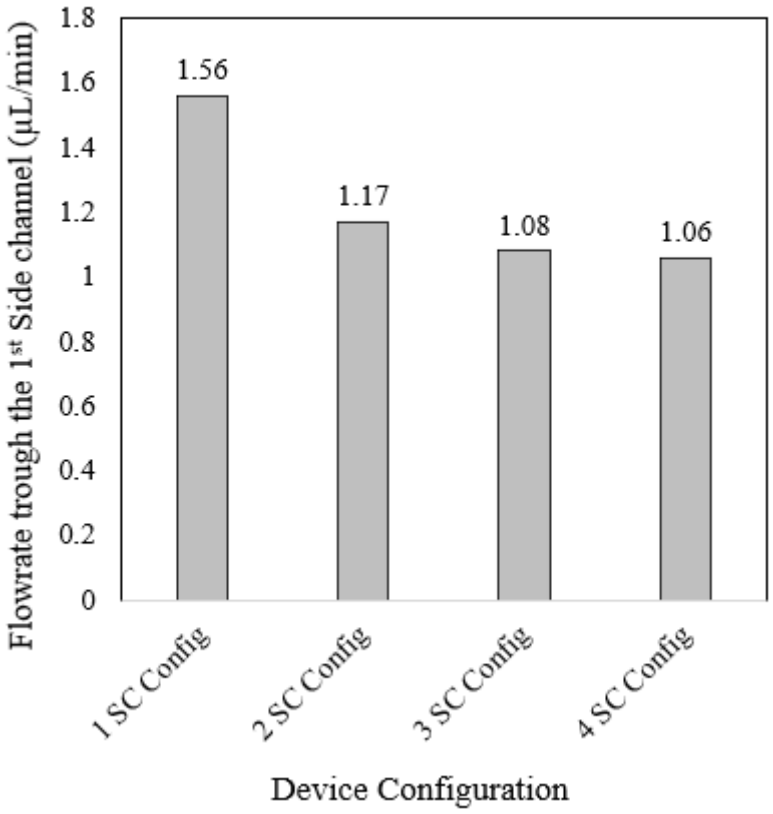

Figure 4.5: Flowrate values through the 1^{st} side channel for different device configurations : flowrate ratio of 30:1 and total flowrate of 3 μL/min

Figure 4.5 shows the flowrate value through the 1^{st} side channel of each of the devices and Figure 4.6 shows the cumulative flowrate through all the side channels in the device. Although the cumulative flowrate through all the side channels is greater for devices with more side channels, it is observed that the flowrate in the first side channel reduces as the number of side channel device increases. This is because the pressure difference between the downstream side channels and the corresponding region in the main channel is less than the first side channel. As the fluid flows through the channel, the pressure reduces and hence less flow is pushed through the downstream side channels.

Figure 4.7 shows the flowrate in each of the side channels in a 4 side channel device. It can

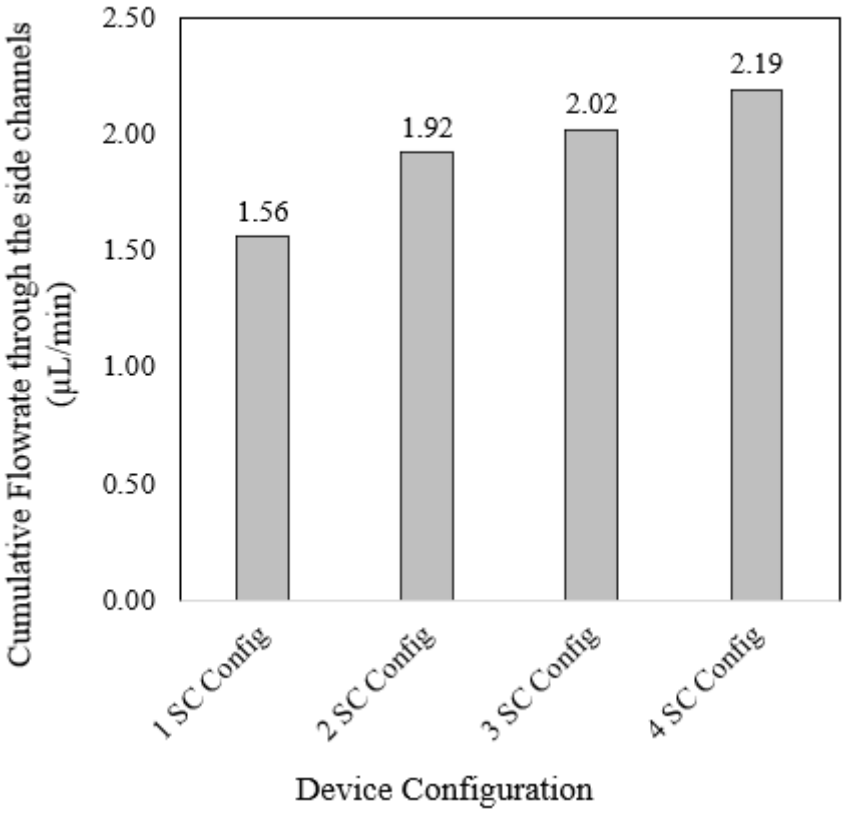

Figure 4.6: Cumulative Flowrate values through the side channels for different device configurations : flowrate ratio of 30:1 and total flowrate of 3 μL/min

be seen that the flowrate through each side channel reduces as we move downstream of the main channel. The higher flowrate in the first side channel corresponds to a higher shear stress index. A similar trend is observed in Figure 4.8, where the flowrate ratio between the two inlets was maintained as 30:1.

In both cases the shear stress index was lowest for the configuration in which the total flowrate was maintained at 1.5 μL/min. Figure 4.9 shows the variation of shear stress index with number of side channels per device for two different flowrate ratios. The lowest shear stress index occurs for the device with four side channels and a 10:1 flowrate ratio.

Finally, to understand the effect of device wall angle on the shear stress index, a four side

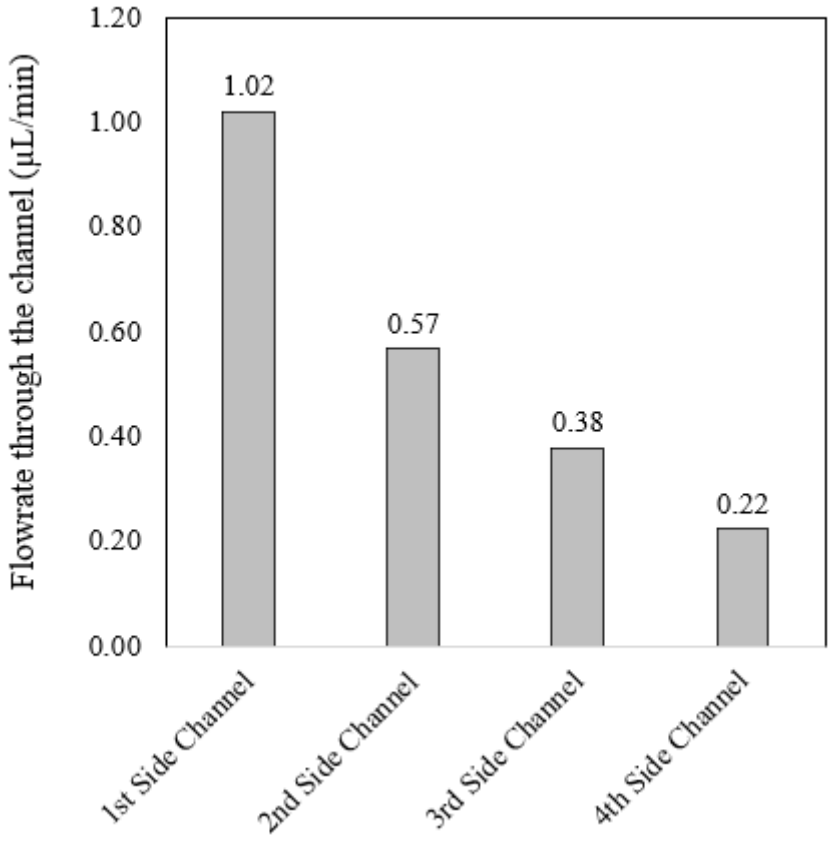

Figure 4.7: Flowrate values through each of the side channels for a 4 Side Channel device configuration : flowrate ratio of 30:1 and total flowrate of 3 μL/min

channel configuration with 10:1 flowrate ratio between the inlets and a total flowrate of 1.5 μL/min with different wall angles was used.

From Figure 4.10 the lowest determined value of shear stress index, τ^*=0.225, corresponding to a $\overline{\tau}$ of 0.337 Pa or 3.37 dyne/cm^2, was recorded in the straight walled device with four side channels for a flowrate ratio of 10:1 between the inlets and a total flowrate of 1.5 μL/min. There is a 40% difference in shear stress between the straight walled device and the 45^o angled wall configuration where the highest shear stress value was observed. This can be attributed to that fact that, for devices with angles walls, the cross sectional area of the

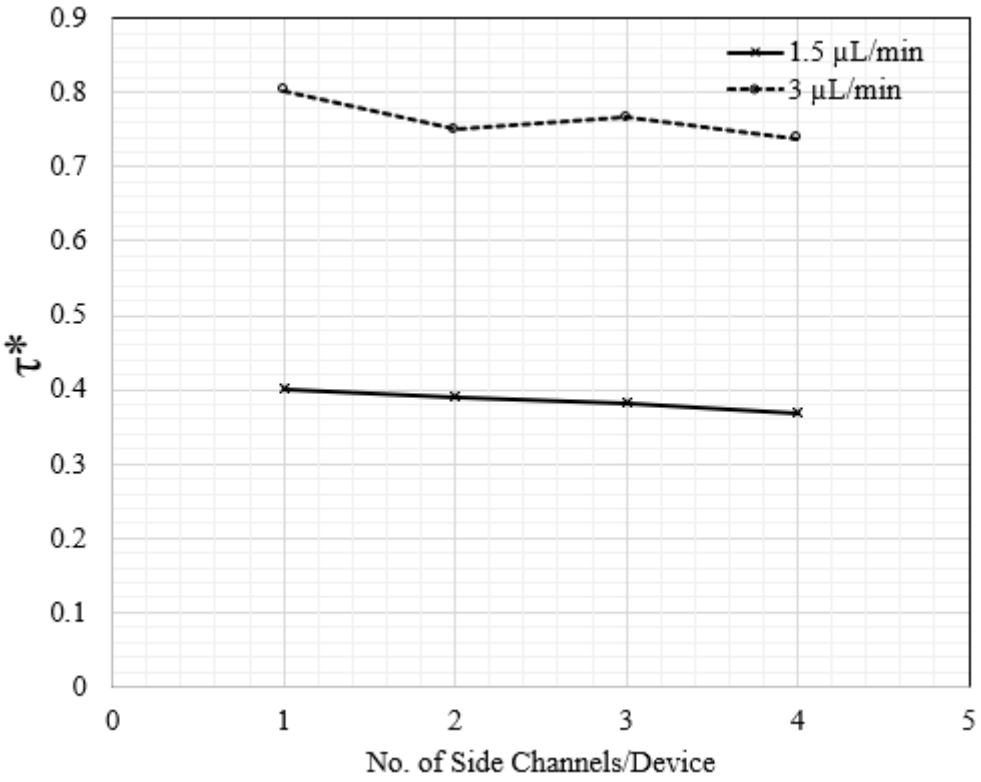

Figure 4.8: Variation of shear stress index with number of side channels for a flowrate ratio of 30:1 between the 10xPBS inlet and the DI water inlet

channel reduces. Since the total flowrate remains the same, the stream wise velocity of the flow increases inside the channel to compensate for the reduction in cross sectional area and to conserve the flowrate [53], as shown in Figure 4.11. It is observed that the velocity in the main channel increases by 33% in the device with 45^o wall angle compared to the straight walled configuration. This increase in velocity causes the shear stress to increase in the channel.

From all the above observations, we can conclude that the configuration in which the cells would experience the least amount of shear is a straight walled device with four side channels with a total flow rate of 1.5 μL/min passing through the system and a flowrate ratio of 10:1 between the inlet channels.

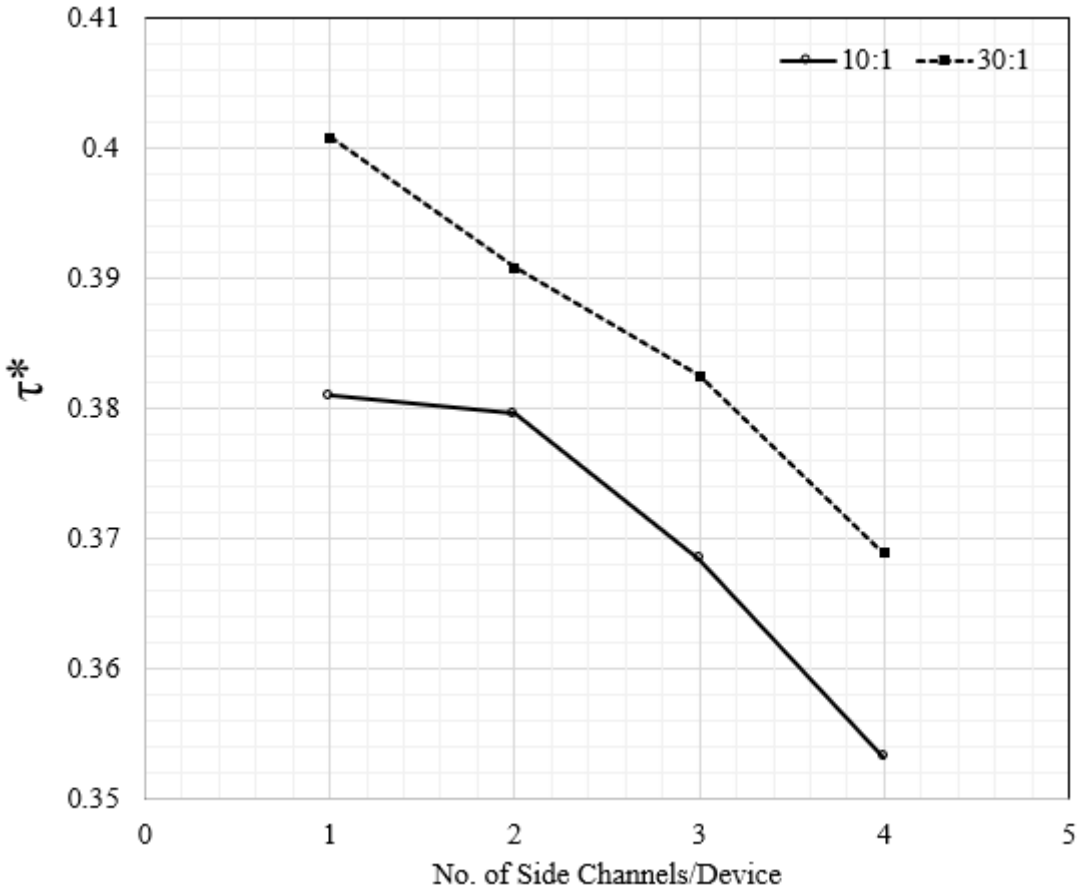

Figure 4.9: Variation of shear stress index with number of side channels for a total flowrate of 1.5 μL/min

4.2 Buffer Exchange Device Throughput

Since the cell diameter is 4x the size of the overlap between the main and the side channels, the cells are expected to remain in the main channel and will be collected at the main channel outlet. Thus the flowrate through the main channel decides throughput of the buffer exchange device. Since the cDEP devices handles a maximum flowrate of 5 μL/min [60], the buffer exchange device that is capable of achieving a throughput close to that value is desirable.

A dimensionless throughput was defined as

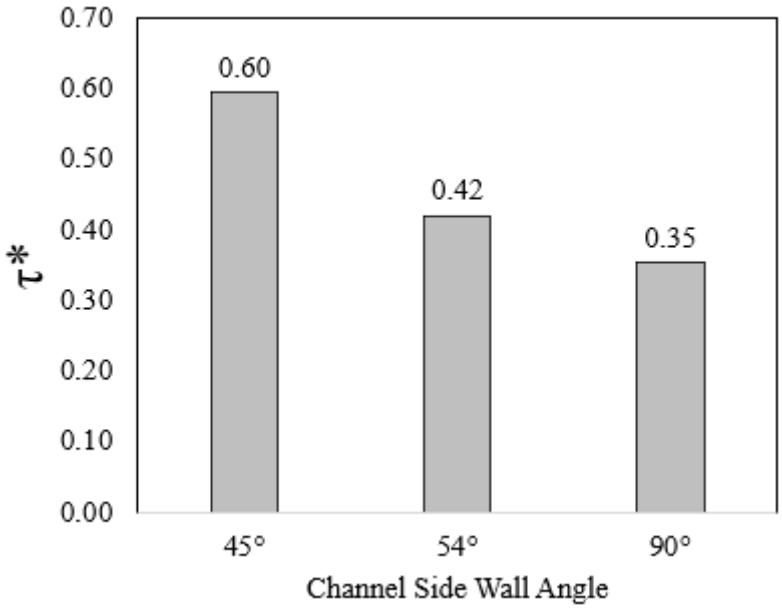

Figure 4.10: Variation of shear stress index with side wall angle for a flowrate ratio of 10:1 between the 10xPBS inlet and the DI water inlet and total flowrate of 1.5 μL/min

$$Q^* = \frac{Q_P}{Q_{Max}}, \tag{4.2}$$

where Q_P is the flowrate through the main channel and $Q_{Max} = 5$ μL/min is the target flowrate though the downstream cDEP device [60].

Simulations were run in Fluent for a straight walled channel to analyze the effect of different side channel configurations and flowrates on the throughput. Figure 4.12 shows the variation of Q^* for 10:1 flowrate ratio between the DI water inlet and the 10x PBS inlet. As expected, it is observed that the throughput for the 3 μL/min flowrate configuration is approximately twice that for the 1.5 μL/min flowrate for all the side channel designs. A similar trend is observed in Figure 4.13 for the 30:1 flowrate ratio between the inlet channels.

It is also observed that the throughput is highest for the single side channel device configura-

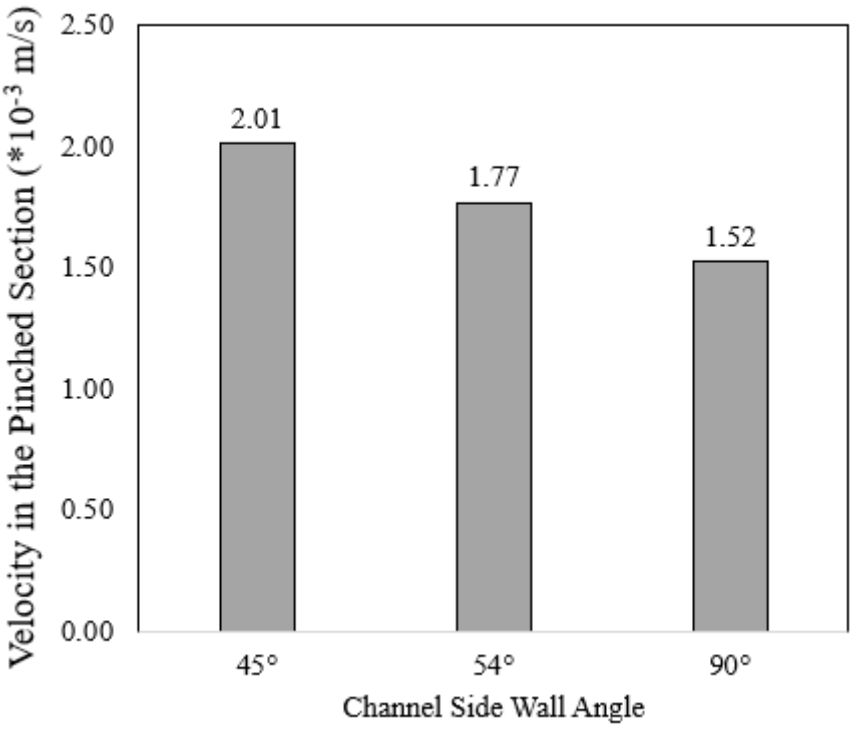

Figure 4.11: Variation of flow velocity in the main channel with side wall angle for a flowrate ratio of 10:1 between the 10xPBS inlet and the DI water inlet and total flowrate of 1.5 μL/min

tion for every flowrate ratio and cumulative flowrate value. As the number of side channels in the device increases, the cumulative volume flowrate of the fluid removed through them increases. Since more flow is removed through the side channels, the overall main channel flowrate reduces, causing a corresponding reduction in throughput ratio.

The effect of flowrate ratios on the throughput for different side channel configurations can be seen in Figure 4.14. It is observed that the difference in result between the two flowrate ratios is minor. The maximum difference in Q^* is less than 2.4%. Hence, it could be concluded that the flowrate ratio does not significantly affect the Q^* values. However, the flowrate of cells in the 10:1 configuration would be three times that of the 30:1 flowrate ratio. This is because the flowrate of cells containing 10x PBS is 1/11 of the total flowrate of

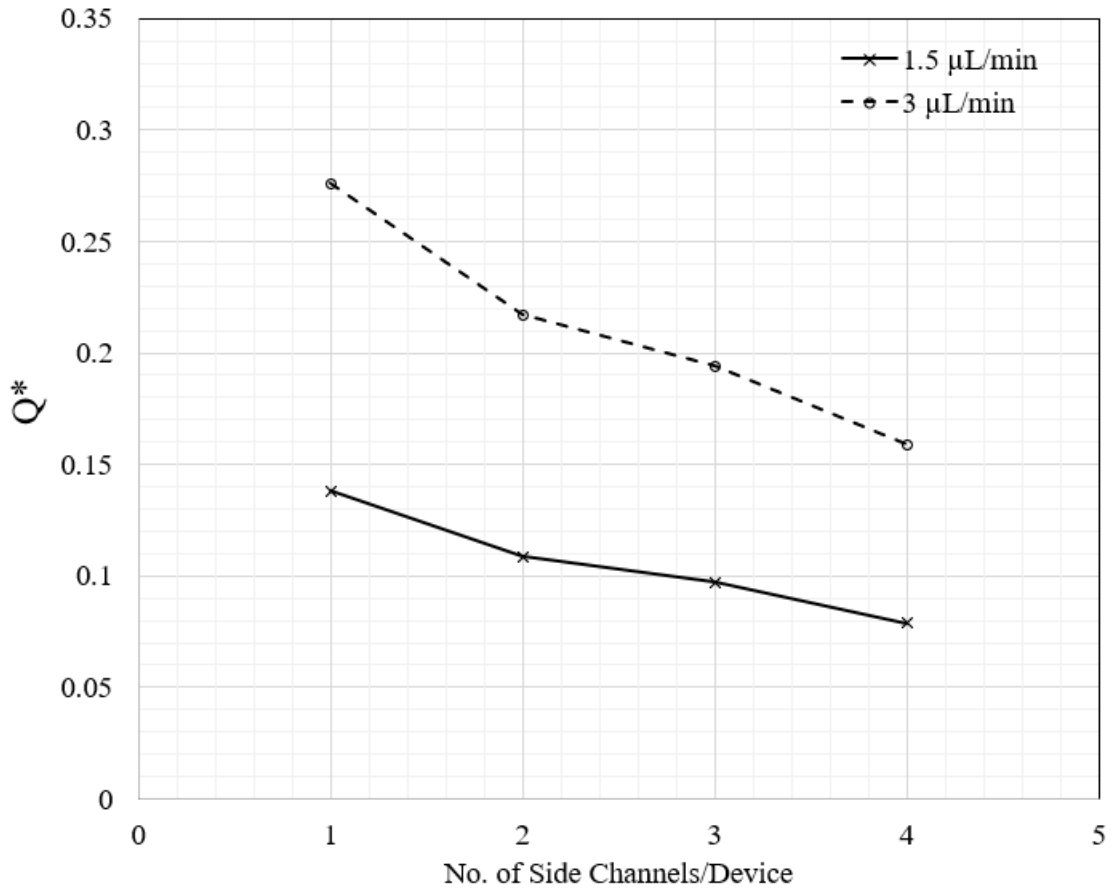

Figure 4.12: Variation of throughput ratio with number of side channels per device for 10:1 inlet flowrate ratio in a straight walled buffer exchange device

3 μL/min, which gives a value of 0.27 μL/min. In the case of the 30:1 configuration, the cells flow at 1/31 of the total flowrate, which gives 0.09 μL/min. Thus the number of cells that experience buffer transfer and are collected at the outlet for a given total flowrate would be three times greater for the 10:1 flowrate ratio configuration.

Finally, the variation of throughput with wall angle was analyzed. From Figure 4.15 it can be observed that the channel with the 45^o wall angle has the highest dimensionless throughput of 0.3, which translates to a main channel flowrate of 1.5 μL/min, followed by the device with 54^o angled walls. The straight walled channel has the least throughput, $Q^* = 0.27$, or

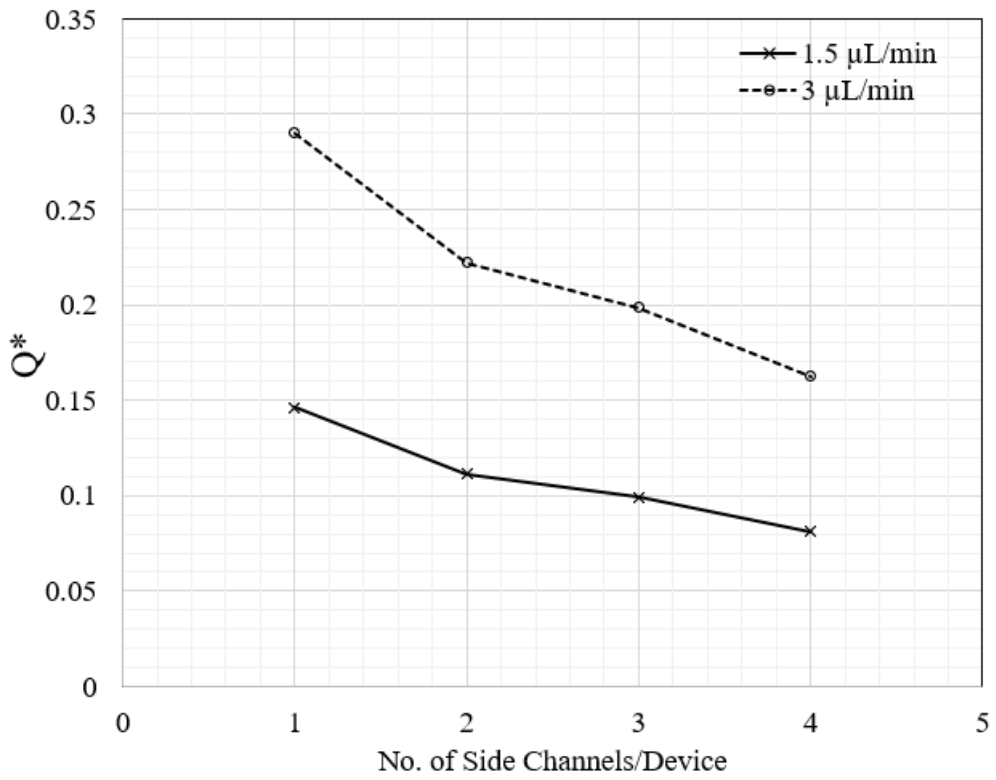

Figure 4.13: Variation of throughput ratio with number of side channels per device for 10to1 inlet flowrate ratio in a straight walled buffer exchange device

Q_P=1.35 μL/min. From the above result, it can be observed that the channel wall angle does not have much effect on the overall throughput of the device. However, an angled wall channel would prevent clogging of cells and help the device to perform effective buffer transfer [48].

Hence, it can be concluded that the single side channel device with a total flowrate of 3 μL/min, a flowrate ratio of 10:1, and a wall angle of 45^o is the optimal configuration for achieving the maximum throughput.

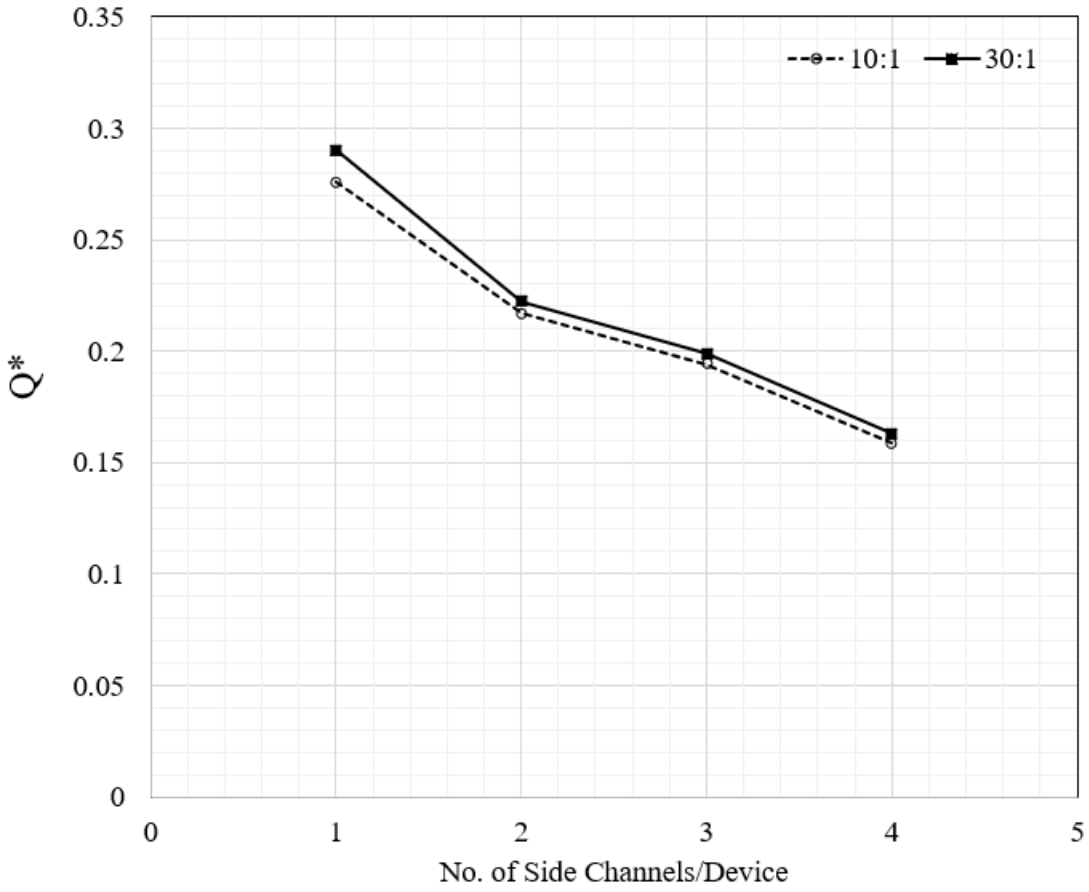

Figure 4.14: Variation of throughput ratio with number of side channels/device for a cumulative flowrate of 3 μL/min

4.3 Outlet Electrical Conductivity

The electrical conductivity of the cell medium plays a major role in running cDEP experiments. Low conductivity buffers are required for cell characterization. However, cells get stressed in low conductivity buffer over long exposure times and start resealing ions into the buffer [58]. This causes a change in overall conductivity and can cause cDEP experiments to fail. To control the outlet electrical conductivity of the buffer, the diffusion of the two inlet fluids inside the device needs to be minimized. The desired value of outlet conductivity for performing cDEP experiments is 0.01 S/m or less. Hence, a buffer exchange device capable

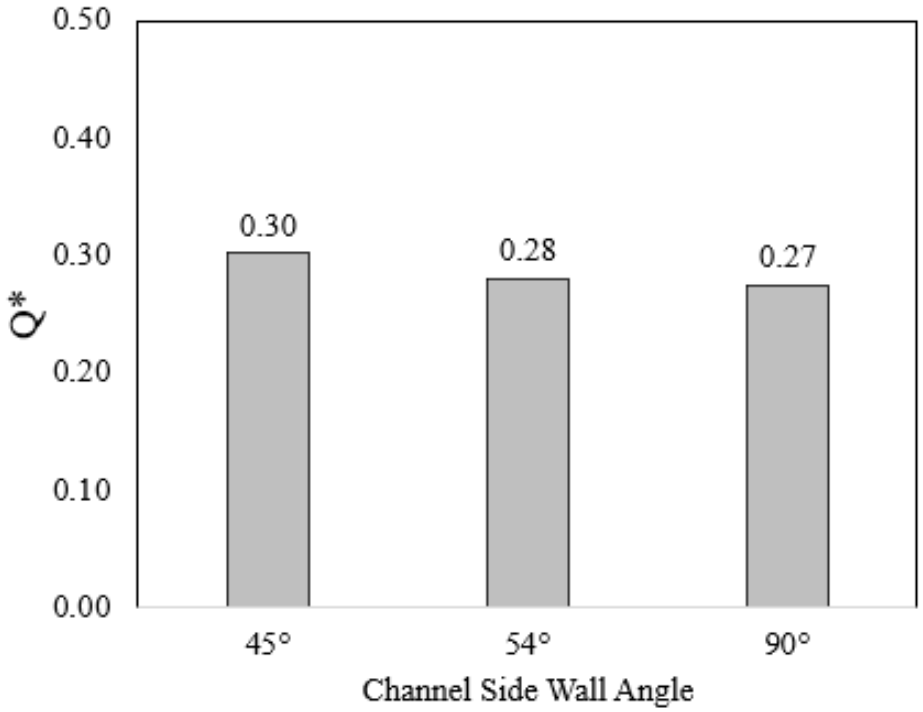

Figure 4.15: Variation of throughput ratio with channel wall angle

of achieving a value less than this value is preferable.

An electrical conductivity ratio was defined as

$$K^* = \frac{K_P}{K_{Req}}, \tag{4.3}$$

where K_P represents the value of electrical conductivity at the main channel outlet and K_{Req} =0.01 S/m is the desired value of electrical conductivity. The optimal device would have K^* < 1.

Simulations were run in Fluent for a straight walled channel in order to analyze the effect of different side channel configurations and flowrates on the electrical conductivity ratio.

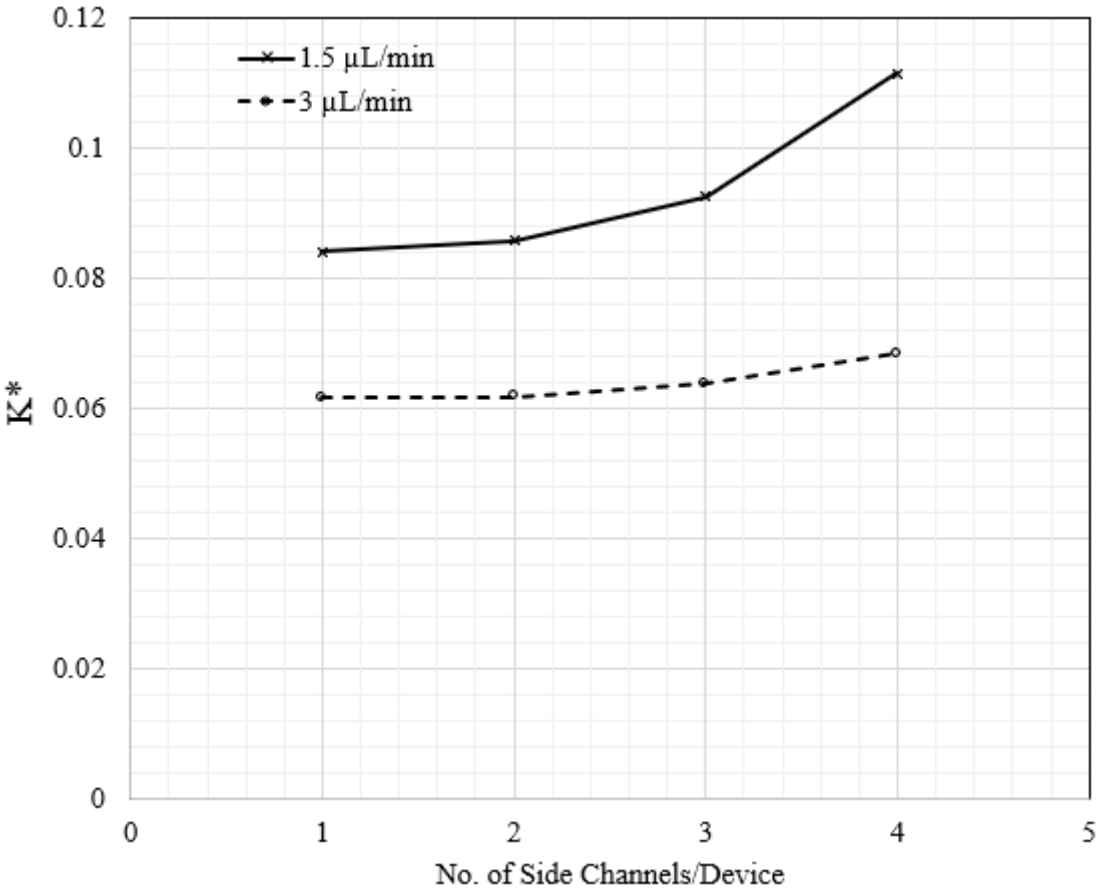

Figure 4.16: Variation of conductivity ratio with number of side channels per device for 10:1 inlet flowrate ratio in a straight walled buffer exchange device

From Figure 4.16, it can be observed that the value of outlet electrical conductivity in all the device configurations is very close to that of the inlet DI water. This value is significantly lower than the desired K^* value of 1, and hence the device is very effective at buffer transfer of cells.

Figure 4.17 and Figure 4.18 shows the depth averaged contours of molar concentration of the 10X PBS, which represents the biological buffer initially containing cells, in the device with a 1 side channel and a 4 side channel configuration, respectively. The diffusion of the 10X PBS can be observed from the contours. Here, red colored regions represent the location in the device where the concentration of 10X PBS is close to 100%. Since 10X PBS exclusively

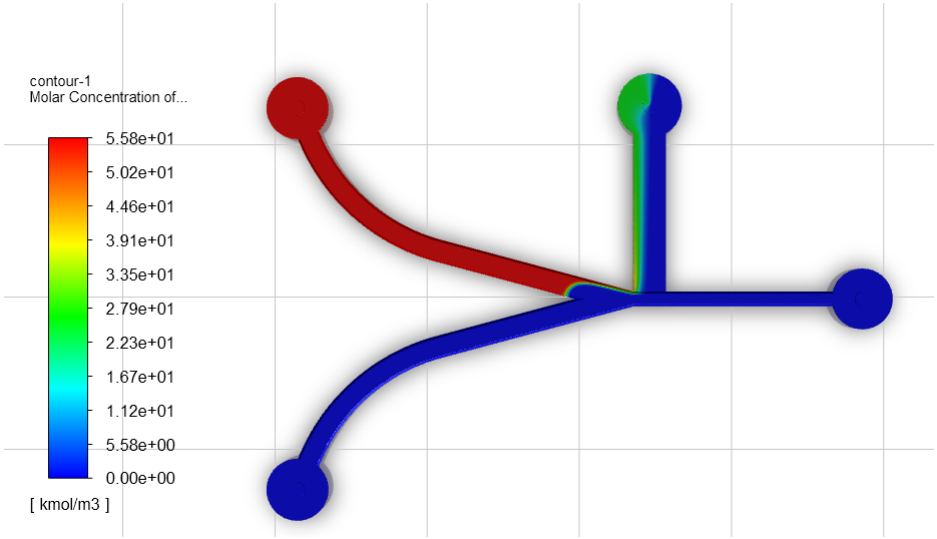

Figure 4.17: Contours of molar concentration of the 10X PBS in a single side channel device

flows through the bio buffer inlet, the concentration in the inlet channel is 100%. As the 10X PBS flows downstream and comes in contact with the DI water, there is observable, but minimal, diffusion in the channel. The effect of diffusion can be observed from the transition of the concentration contour in red to green, showing that the local concentration of 10X PBS is not 100% in those regions. However, before the 10X PBS completely diffuses into the DI water, it gets pushed out of the side channels due to the high values of the DI water flowrate. This reduces the concentration of the 10X PBS significantly, close to 0%, in the main channel. The absence of 10X PBS is represented as a dark blue color in the contour. Since the cells remain in the main channel, they get transferred from a region of 100% 10X PBS concentration to near 0% concentration (i.e., into the DI water). Hence, Figure 4.17 and Figure 4.18 also serve as a visual representation of buffer transfer in the device.

The low mixing in the device can be attributed to the low Reynolds number values of less than 1 in the channel. At such a low Reynolds number, the flow remains completely laminar, the flow streamlines remain parallel, and hence very low mixing of fluids occurs. There is also low diffusion owing to the low residence time of the fluids in the device. Since the fluids

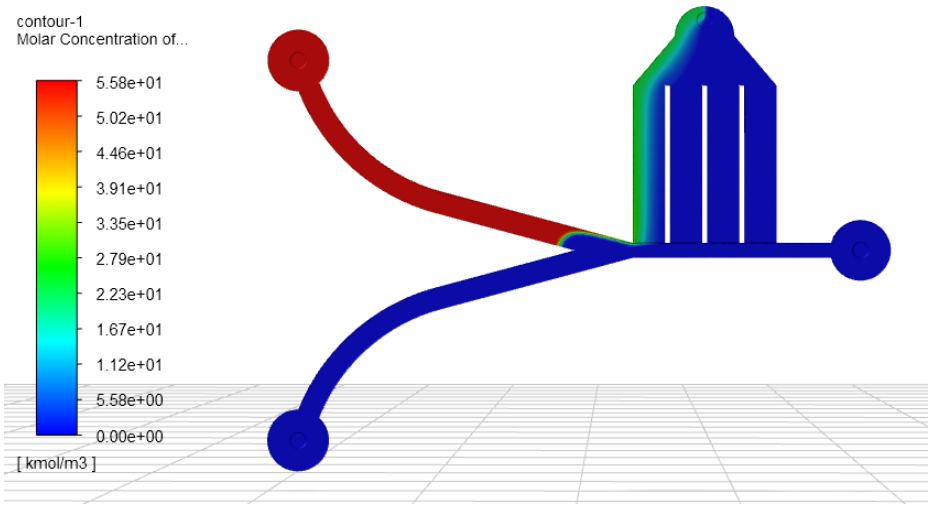

Figure 4.18: Contours of molar concentration of the 10X PBS in a 4 side channel device

spend less than 12 seconds in the device, the time available for diffusion is small.

From Figure 4.16, it could also be observed that for both of the flowrate ratios, the 1 side channel configuration has the lowest K^* value, and K^* keeps increasing as the number of side channels per device increases. The maximum K^* value, and hence the worst buffer exchange, is observed in the 4 side channel configuration. As it can be observed from Figure 4.6, the cumulative flowrate through the side channels keeps increasing as the number of side channels per device increases. Consequently, the flow through the main channel reduces with an increase in number of side channels per device. Hence, the highest flowrate value is observed in the single side channel and the lowest flowrate occurs in the main channel of the 4 side channel configuration. Since pressure drop and flow resistance across any channel is based on the flowrate, a very high flow resistance is encountered in the main channel of the single side channel configuration and the lowest values of flow resistance are found in the main channel of the 4 side channel configuration. The high flow resistance in the single side channel configuration induces a high back pressure in the main channel, which causes the low velocity 10X PBS to be pushed out more effectively through the side channel in

comparison with the other device configurations.

The difference in molar concentration between the single side channel and 4 side channel configuration was analyzed in 5 different planes along the flow direction as shown in Figure 4.19.

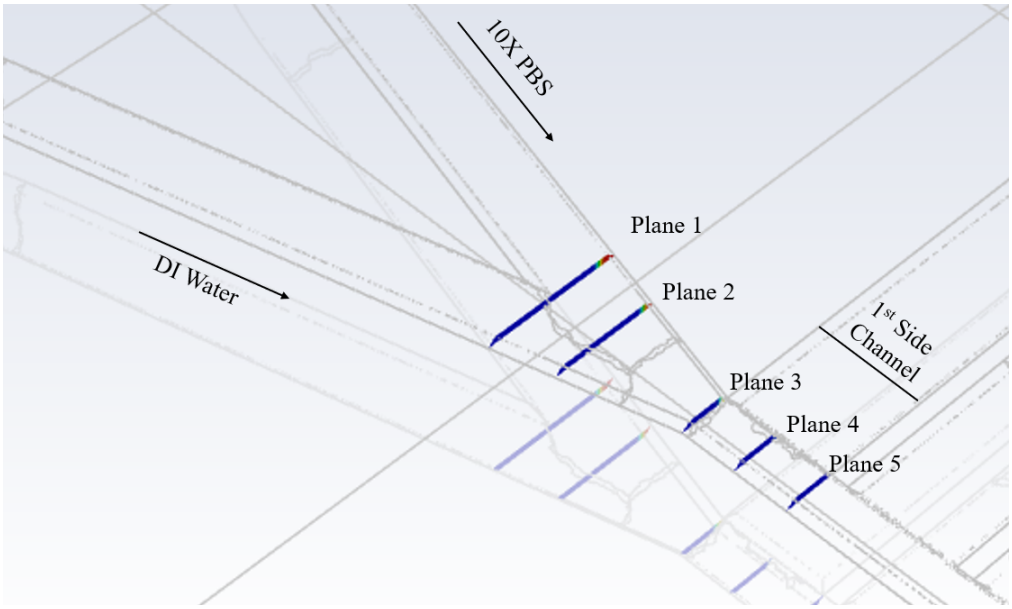

Figure 4.19: The planes along the channel where the concentration values are analysed for single side channel and 4 side channel device configurations

The values of molar concentration were recorded from Fluent, and MATLAB was used to generate surface plots.

From Figure 4.20 and Figure 4.21 it is observed that there is no noticeable difference in the molar concentration values between the 1^{st} and the 2^{nd} planes. The shape of the surface plot depicts the variation of molar concentration values of 10X PBS in the device cross section. Since the 10X PBS gets pushed towards the wall by high velocity DI water, its concentration is highest near the corresponding side wall. The value of concentration rapidly drops off with distance from side wall due to low diffusion in the device.

There is a very small but observable difference in the concentration profiles between the two

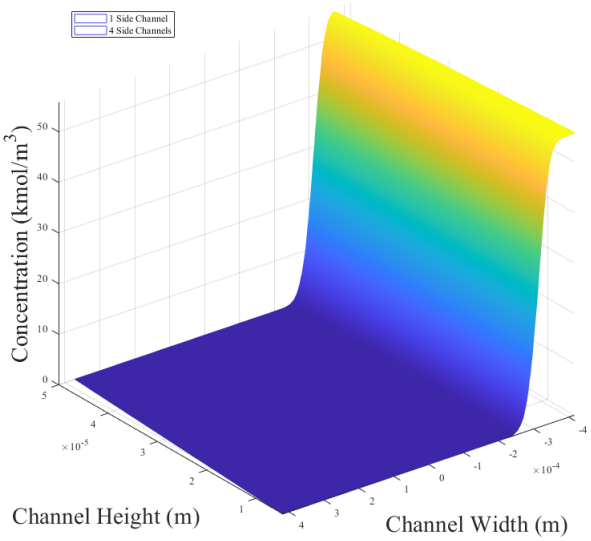

Figure 4.20: Comparison of molar concentration at Plane 1 (Figure 4.19) between 1 side channel and 4 side channel configurations

device configurations at plane 3, which is at the beginning of the main channel, as shown in Figure 4.22. The difference is greatly amplified a short distance downstream in planes 4 and 5, as shown in Figure 4.23 and Figure 4.24.

As we move downstream through the main channel, the concentration values are significantly lower in the single side channel configuration compared to the 4 side channel device. Furthermore, the concentration of 10X PBS drops off faster in the 1 side channel device compared to the 4 side channel configuration as we proceed downstream. This indicates that in the single side channel configuration the 10X PBS is pushed through the side channel more upstream than in the 4 side channel device, causing less diffusion to occur in the channel. Since the overall outlet electrical conductivity value is dependent on the concentration of the PBS medium, the single side channel with the lower downstream 10X PBS concentration has a lower K^* value. The variation of molar concentration between the two configurations in the plane of overlap is shown in Figure 4.25.

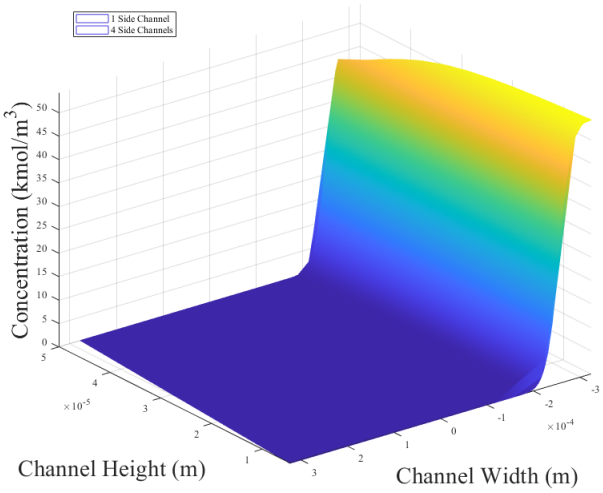

Figure 4.21: Comparison of molar concentration at Plane 2 (Figure 4.19) between 1 side channel and 4 side channel configurations

As expected, the concentration profile is noticeably steeper in the single side channel configuration. This is further indication that the 10X PBS is pushed out through the side channels more upstream in the single side channel configuration, which leads to lesser diffusion and lower outlet electrical conductivity. The electrical conductivity values were compared at the main channel outlet for single and 4 side channel configurations as shown in Figure 4.26.

It can be observed that the conductivity value at the outlet of 1 side channel is noticeably lower than in the 4 side channel configuration. Moreover, it can also be observed that the concentration is homogeneous at the outlet of the main channel for both of the configurations. On top of being further proof of the effective buffer transfer capability of the device, homogeneous distribution of the medium helps with preventing cell lysis and increases cell viability. The absence of local concentration gradients is also essential for performing downstream cDEP analysis.

From Figure 4.16 it could be further observed that devices with a cumulative flowrate of 3 μL/min have a lower K^* value for the same number of side channels and the same flowrate

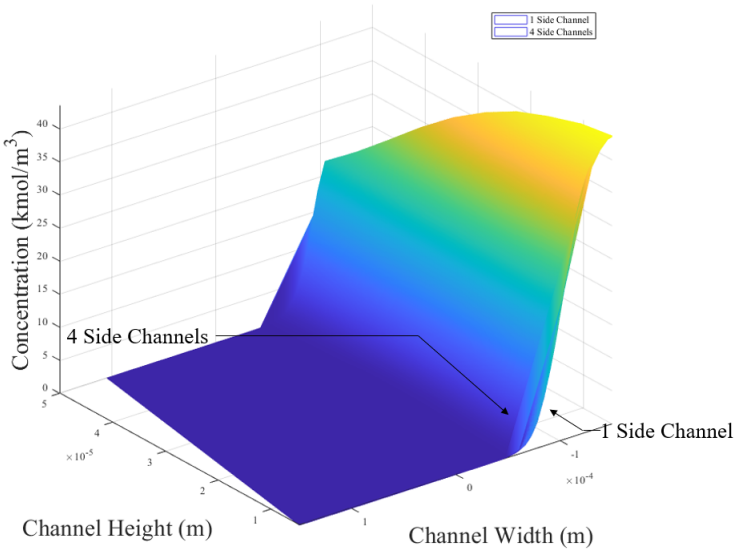

Figure 4.22: Comparison of molar concentration at Plane 3 (Figure 4.19) between 1 side channel and 4 side channel configurations

ratio. The higher cumulative flowrate through the device leads to higher flowrate through the main channel compared to the lower cumulative flowrate counterpart. This causes the flow resistance to increase in the both the main channel and the side channels. But this increase in flow resistance is not equal in the main and side channels. Since the cross sectional area of the main channel is smaller compared to that of the side channels, the flow resistance rises significantly in the main channel compared to the side channels for even a small rise in flowrate. This increase in flow resistance in the 3 μL/min configuration pushes the 10X PBS through the side channel more effectively, as discussed above. A similar trend is observed for configurations with an inlet flowrate ratio of 30:1 as shown in Figure 4.27.

Here too it can be observed that the single side channel configuration has a lower value of K^* compared to devices with a greater number of side channels, and the 3 μL/min flowrate configuration results in lower outlet conductivity.

The K^* values were compared between the 10:1 and 30:1 flowrate ratio configurations for

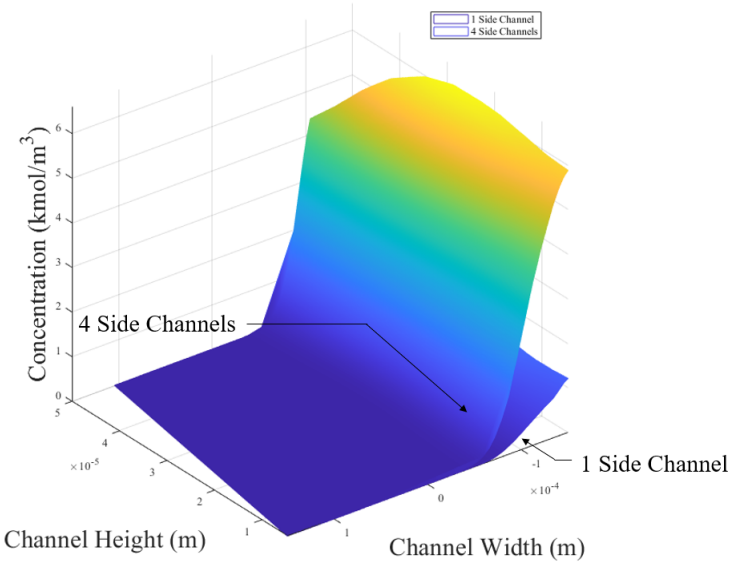

Figure 4.23: Comparison of molar concentration at Plane 4 (Figure 4.19) between 1 side channel and 4 side channel configurations

devices with a total flowrate of 3 μL/min, as shown in Figure 4.28. It can be observed that configurations with a 30:1 flowrate ratio have a slightly lower value of K^* compared to 10:1 flowrate ratio configurations. This difference can be attributed to the high flowrate and high momentum of DI water in the 30:1 configuration, which causes it to push the low momentum 10X PBS a bit more effectively through the side channel. Furthermore, in the 30:1 flowrate ratio configuration, the overall flowrate of the 10X PBS is about 3 times lower than in the 10:1 configuration. This leads to a lower concentration of 10X PBS in the main channel and, ultimately, a lower electrical conductivity.

Note that the difference in the $K*$ value between the 10:1 and 30:1 flowrate ratio configurations is less than 2%, while the flowrate of cells in the 10:1 configuration is about 3 times that in the 30:1 configuration. Thus the 10:1 flowrate ratio configuration is likely preferred. Finally, the impact of wall angle on the K^* value was analysed for the single side channel configuration with a total flowrate value of 3 μL/min and an inlet flowrate ratio of 10:1.

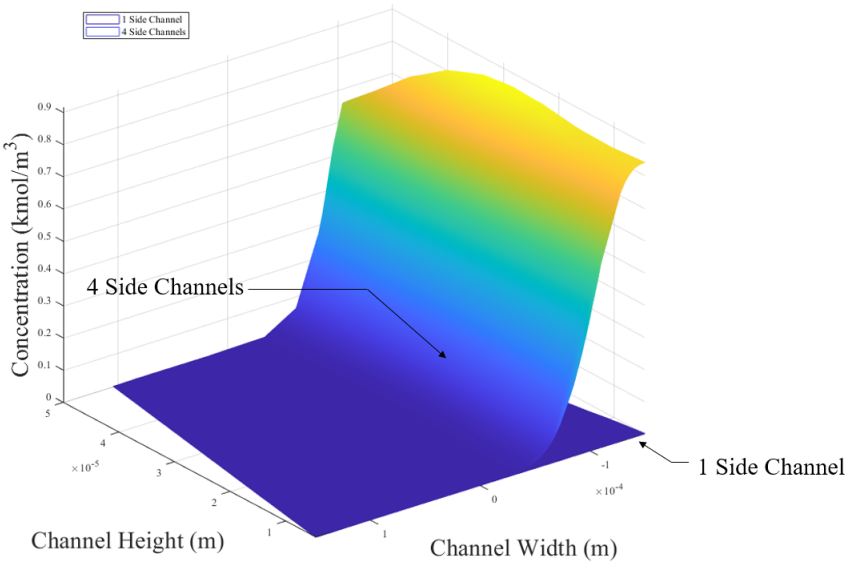

Figure 4.24: Comparison of molar concentration at Plane 5 (Figure 4.19) between 1 side channel and 4 side channel configurations

It can be observed from Figure 4.29 that there is no significant variation in the K^* values caused by changes in side wall angle. However, there is an observable increase in the overall conductivity value with increase in the wall angle. The device with 45^o angled side walls has a conductivity value that is 2% lower than in the straight walled channel.

Since the cross sectional area of the main channel is smaller for the angled side walled configurations compared to the straight walled configurations, the velocity of the fluid in the main channel increases in the angled configurations to conserve the flowrate. Moreover, the reduction in cross sectional area leads to greater flow resistance in the main channel. As discussed above, this increase in resistance results in the 10X PBS being pushed through the side channel with increased effectiveness. Thus the concentration of the 10X PBS reduces in the main channel, causing the outlet conductivity to be smaller in the angled side walled configurations. It can be concluded that a single side channel device with 45^o angled walls, a 3 μL/min cumulative flowrate, and an inlet flowrate ratio of 10:1 is the optimal configuration

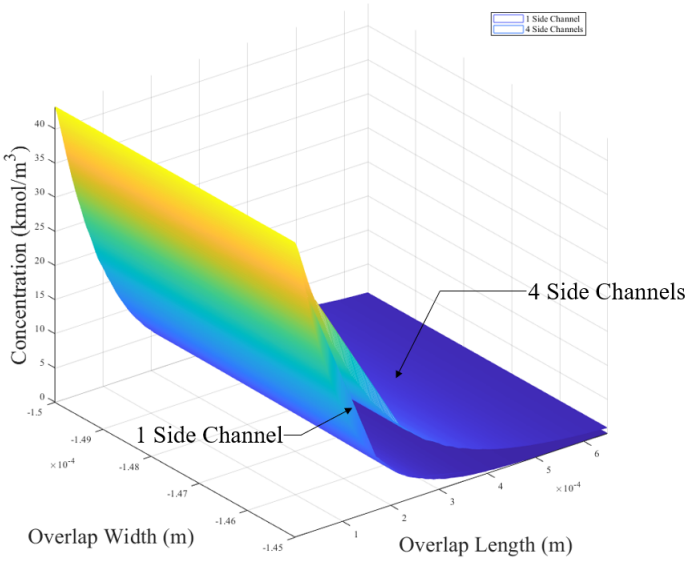

Figure 4.25: Comparison of molar concentration at the overlap plane between 1 side channel and 4 side channel configurations

for maintaining low outlet conductivity.

4.4 Summary of Results

A detailed CFD study was performed with the buffer exchange device. The key input variables for the study were the number of side channels per device, the total flowrate through the device, the inlet flowrate ratio and the side wall angle. The results of this parametric sweep helped identify the optimal device and flow configurations for

- minimizing fluid induced shear stress in the device,
- supporting high throughput for downstream cDEP analysis, and
- maintaining high control over electrical conductivity values at the outlet.

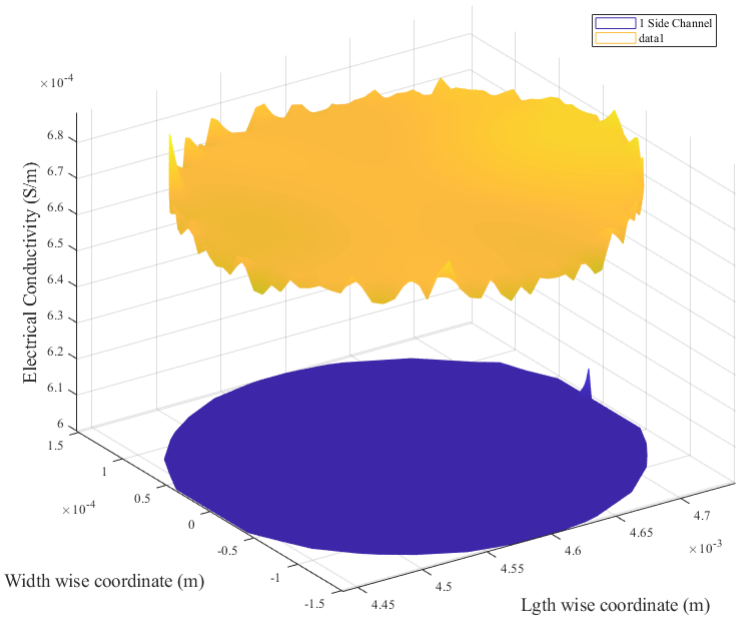

Figure 4.26: Comparison of electrical conductivity at the main channel outlet between 1 side channel and 4 side channel configurations

The results of this study are summarized in Table 4.1. From the results of the parametric study, it is ascertained that the single side channel with 45^o side walls, a 10:1 inlet flowrate ratio, and a total throughput of 3 μL/min is the optimal configuration for maintaining high throughput, low outlet conductivity, and a sufficiently low value of shear stress in the device. The angled side walls prevent the cells from clogging at the 5 μm orifice between the main channel and the side channels. These features make this configuration the most effective of the considered configurations for buffer transfer of cells.

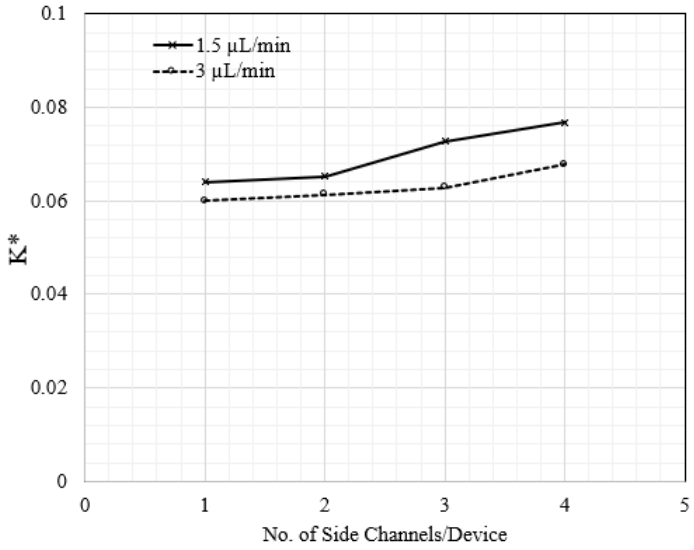

Figure 4.27: Variation of conductivity ratio with number of side channels per device for 30:1 inlet flowrate ratio in a straight walled buffer exchange device

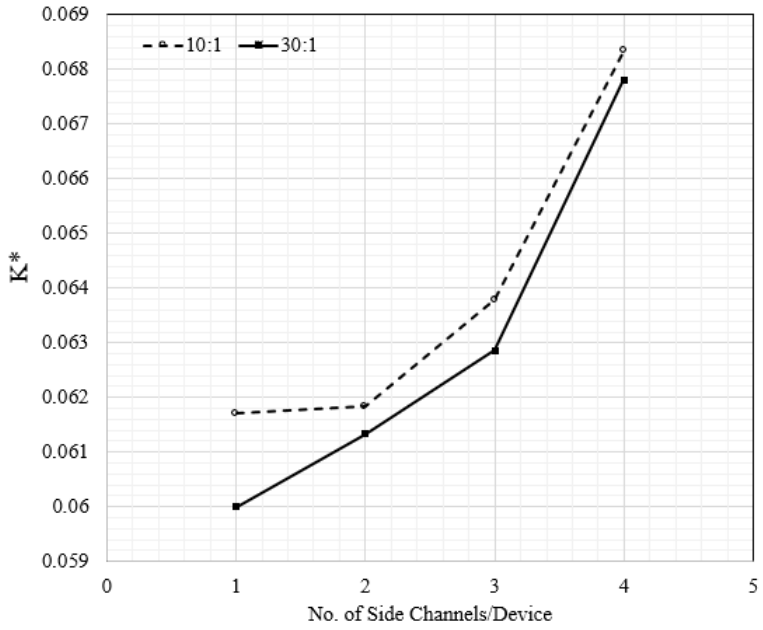

Figure 4.28: Variation of conductivity ratio with number of side channels per device for 3 μL/min total flowrate in a straight walled buffer exchange device

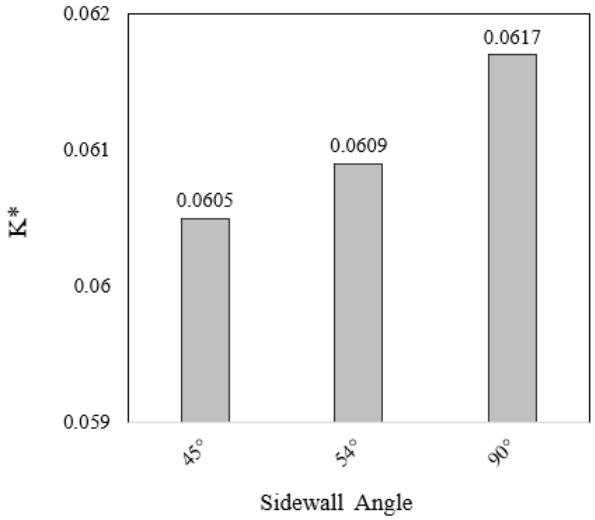

Figure 4.29: Variation of conductivity ratio with side wall angle for 3 μL/min total flowrate and 10:1 flowrate ration in a single side channel configuration

Table 4.1: A summary of the parametric study: Optimal configurations identified for specific objectives

Objective	**Optimal Configuration**				**Result**	
	Side Channels /Device	**Total Flowrate (µL/min)**	**Inlet Flowrate Ratio**	**Side Wall Angle**	**Target Value**	**Achieved Value**
Minimizing shear stress (Pa)	4	1.5	10:01	90^o	1.5	0.34
Maximizing throughput (µL/min)	1	3	10:01	45^o	-	1.5
Maintaining low outlet conductivity (S/m)	1	3	10:01	45^o	0.01	0.000605

Chapter 5

Fabrication of the Buffer Exchange Device

The are three distinct stages in the fabrication of the buffer exchange device:

- design of a two-dimensional (2D) photomask,
- development of silicon wafers with the inverse mold of the buffer exchange device, and
- physical fabrication using polydimethylsiloxane (PDMS).

The buffer exchange device was designed to consist of two layers. The top layer contains the inlet and the main channels and the bottom layer contains the side channels, as shown individually in Figure 5.1. The two layers are to be aligned on top of each other in such a way that the side channel overlaps the main channel by approximately 5 μm. The details of fabrication are discussed below.

5.1 Design of the 2D Photomask

Once the design of the device was finalized, the 3D model was split into two parts, with one part containing the inlet and main channel (Figure 5.1a) and the other part containing the side channels (Figure 5.1b). This was done for all of the side channel configurations. Then

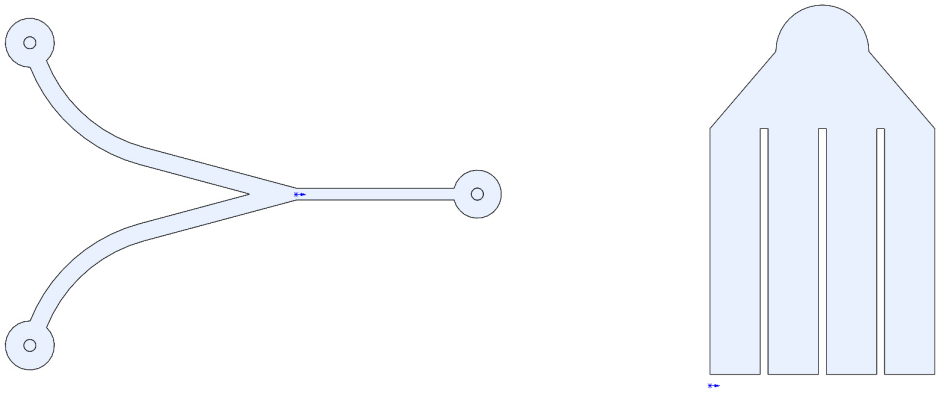

(a) (b)

Figure 5.1: The two layers of the device for a 4 side channel configuration: (a) inlet and main channels and (b) side channels

the 3D models of the parts were converted to 2D CAD models in AutoCAD software. The 2D CAD model of the main channel and the side channels are shown in Figure 5.2. Once the layers were fabricated, precision alignment is required to make sure that the side channel layer overlaps the main channel layer by approximately 5 μm. Since the operation of the device depends on effectively filtering the cells out of the PBS using the 5 μm overlap, this alignment process becomes very critical while fabricating the device.

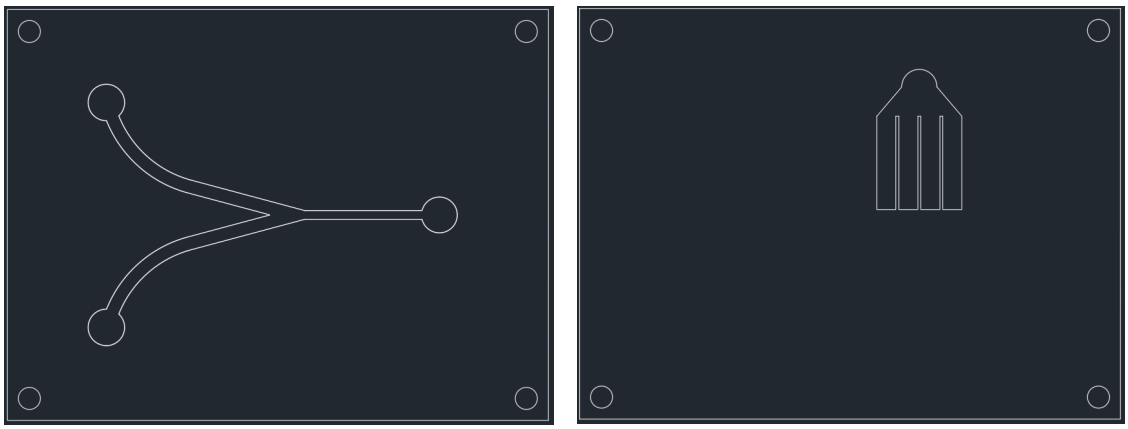

(a) (b)

Figure 5.2: CAD model of the two layers of the device (a) main channel (b) side channels

Since the size of the each layer is less than 10mm, a silicon wafer of 100mm diameter was chosen as a substrate for making the chips. Based on this selection, a 10 in by 12 in transparency photomask with 20k dots per inch (DPI) was designed. Since the smallest features in the design of each individual layer was 50 μm, a low resolution polyester photolithograpy mask was chosen, since it is the least expensive option that can reproduce this scale of features [28]. CAD/Art Services Inc.(Bandon, OR) was contracted to fabricate the mask through precise laser cutting. Positive polarity of the mask was decided upon based on the use of the Deep Reactive Ion Etching (DRIE) process for etching the wafer [34]. Eight pairs of layers with varying numbers of side channels were printed on the mask, as shown in Figure 5.3.

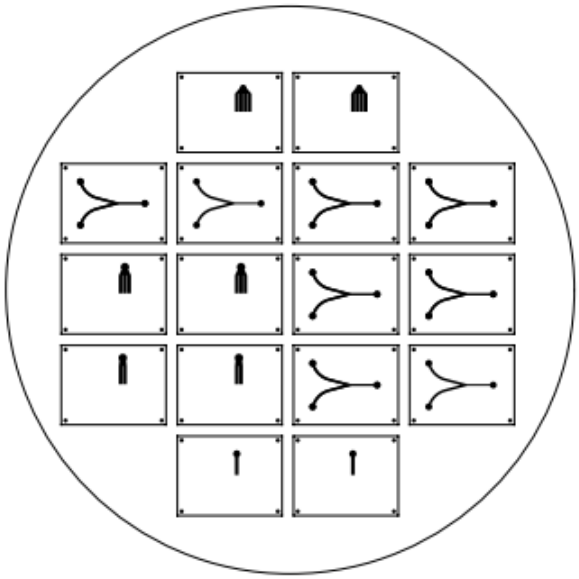

Figure 5.3: 2D design transparency photomask with emulsion side up

5.2 Development of Silicon Wafer

The transparency mask was sent to the Chapel Hill Analytical and Nanofabrication Laboratory (CHANL) at UNC Chapel Hill. The Alcatel AMS 100 Deep Reactive Ion Etcher in the

Chapman Hall clean room was used for the DRIE process. In this process, the transparency mask is first aligned with the silicon wafer substrate using precision mask alignment methods [41]. The Bosch DRIE process is used to etch the wafer substrate. This process is also called "time-multiplexed etching" as it comprises of two phases that alternate over and over again. The first phase is the plasma etching phase where ions in a plasma are made to etch the wafer in the vertical direction. Based in the polarity of the transparency mask, the plasma etches the exposed silicon wafer. The design on the wafer is etched layer by layer. After the initial etching, an inert passivation layer is coated on top of the etched layer to protect the wafer substrate from further chemical etching. This is the second phase. When the first phase is repeated again, the ions in the plasma collide with the base of the protective coating and remove it, increasing the groove depth. However, the side walls coated with the protective layer remain intact. This process is repeated many times over until the desired channel depth is reached in the wafer [33]. In this process, inductively coupled plasma along with fluorine gas was used as the etchant and silicon dioxide was used as wafer substrate. Similar to the 2D photomask, 8 pairs of layers with varying numbers of side channels were etched on each wafer, as shown in Figure 5.4.

Since PDMS was chosen for fabricating the device, the silicone wafers were silanized. Silanization is a process of passivating the wafer to prevent the PDMS from bonding with the substrate so that it can be removed from the wafer once cured [74]. Trichlorosilane (97% - Aldrich Chemistry, St.Louis, MO) was used for silanizing the wafer. In this process the wafer was placed in a desiccator along with 100 μL of trichlorosilane. Once a vacuum was generated inside the chamber, the valve of the desiccator was closed and the wafer was left undisturbed for 3 hours to let silane vapour coat its surface.

To prevent the PDMS from flowing out of the wafer, 1.5mm thick walls were designed such that they encircled the circumference of the wafer. The walls were fabricated using

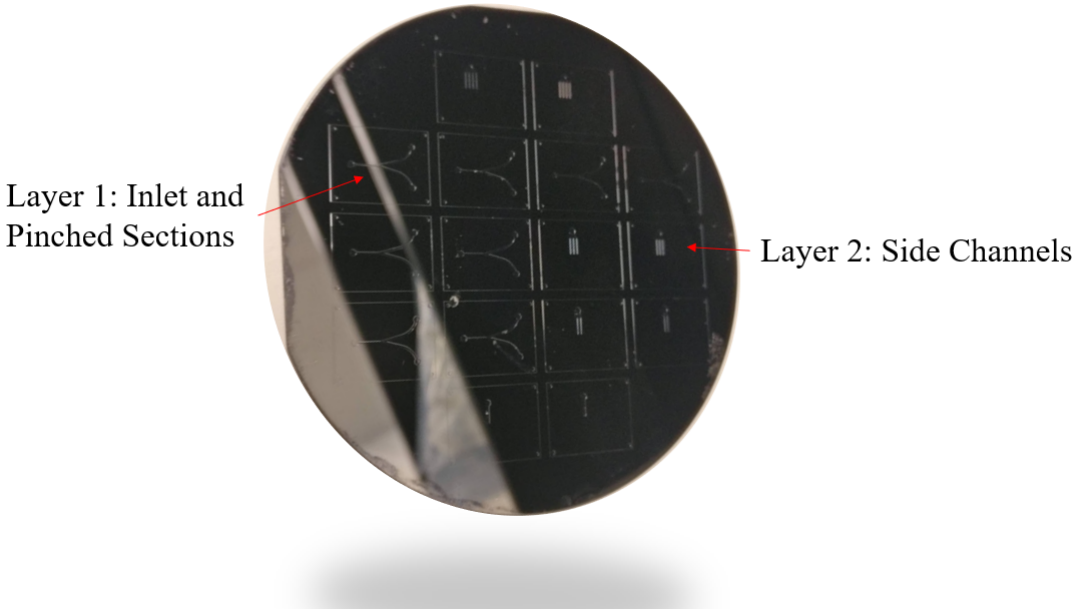

Figure 5.4: Silicon wafer etched with the layers of the buffer exchange device through DRIE

polymethylmethacrylate (PMMA). Since PMMA is a thermoplastic [70], it can withstand temperatures of 100 ^{o}C, the temperature required for curing PDMS. Furthermore, it can be precisely machined to fit the circumference of the wafer through laser cutting [66]. Finally, PDMS does not form a strong bond with PMMA under normal conditions, and hence the cured PDMS could be easily removed from the wafer [32][69].

For cutting the PMMA slabs into the desired shape, the Universal Laser Systems (Scottsdale, AZ) version 3.60 CO_2 laser cutting machine at the Center for Engineered Health (CEH) at Virginia Tech was used. The walls were then glued to the circumference of the silicon wafer using 5 Minute Epoxy. A wafer with PMMA wall glued to its circumference is shown in Figure 5.5.

Here the wall, wafer and the epoxy used to glue them together is clearly seen. The PDMS, which would be added on to the wafer, would now stay within the bounds of the wafer

circumference while curing.

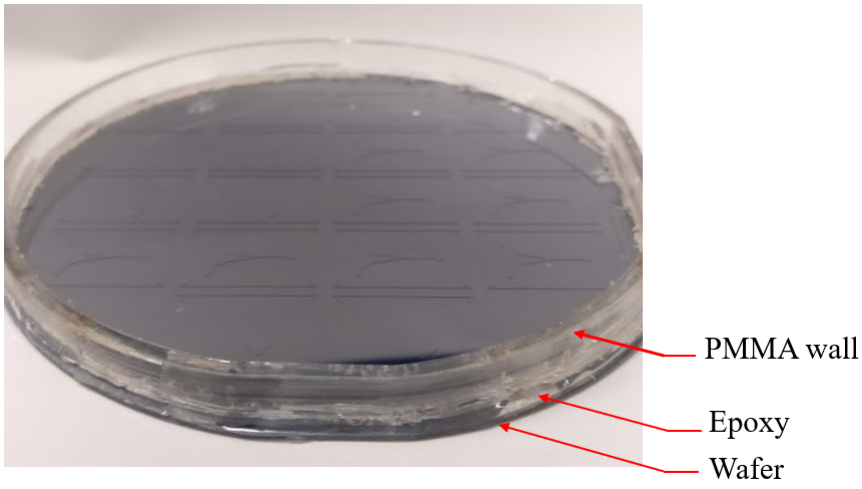

Figure 5.5: PMMA wall glued to the circumference of the silicon wafer

5.3 Fabrication of buffer exchange device using PDMS

For fabricating the device from the silicon wafer, PDMS was chosen as the ideal material since it is bio compatible [36], has high strength and durability [54], and can have miltiple layers robustly bonded [12]. The most commonly available PDMS, SYLGARD 184 (Dow Corning, Midland, MI) was used as the base PDMS along with Dow SYLGARD 184 SILICONE CURING AGENT.

The PDMS and the curing agent were mixed well at a ratio of 10:1 (w/w). The mixture was placed in a Thermo Scientific (Waltham, MA) Nalgene Vacuum Chamber for 20 minutes to degass and remove any bubbles that formed when mixing the solutions. Then the PDMS mixture was poured onto the silicone wafer in such a way as to minimize production of bubbles. Since pouring the PDMS on a wafer inevitably leads to formation of small bubbles both on the surface and inside the PDMS [29], the wafer with PDMS was left in the above

vacuum chamber for 20 minutes, as shown in Figure 5.6.

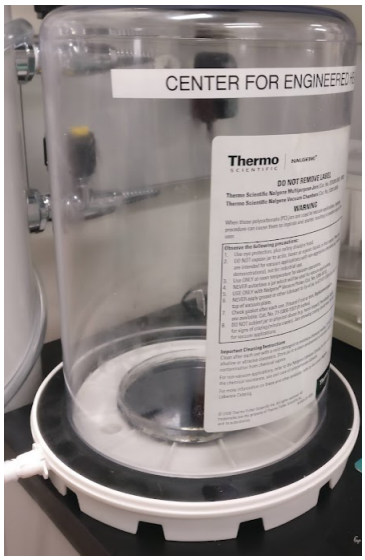

Figure 5.6: Silicon wafer with 10:1 PDMS mixture placed in vacuum chamber for removing small bubbles

Once the bubbles were removed, the wafer with PDMS mixture was carefully transferred to a hot plate for curing, as shown in Figure 5.7. A temperature of 95^{o}C was maintained for 1 hour so that the thermosetting curing agent actively formed chemical bonds [31], and the PDMS was set into a flexible solid suitable for running tests. The side of the cured PDMS in contact with the wafer was moulded with the same pattern on the wafer, which in this case are the layers of the buffer exchange device.

The wafer was then removed from the hotplate and a scalpel was used to remove the cured PDMS from the wafer, as shown in Figure 5.8. Care was taken to avoid scraping the substrate or the epoxy glue.

The two layers of the buffer exchange device were cut out from the cured PDMS. The first layer contains the inlet and main channels and the second layer contains the side channels. Figure 5.9 shows the two layers and the scale of the device can be discerned from it.

For bonding the two PDMS layers, the surfaces were treated with plasma in the Harrick

Figure 5.7: Silicon wafer with 10:1 PDMS placed on a hotplate for curing the mixture

Plasma Cleaner (Ithaca, NY) located at CEH, Virginia Tech. In this process, the two layers of the device were placed inside the chamber with the surfaces to be bonded facing up. A vacuum pressure of 200 mTorr was generated inside the chamber. Then the radio frequency (RF) power was turned on at the highest setting. After a few seconds, a faint purple glow was observed inside the chamber which indicated that the ionic plasma had started to generate inside the chamber. At this point, the needle valve's position was adjusted so as to allow optimal air flow inside the chamber. This enhanced the generation of plasma and a bright

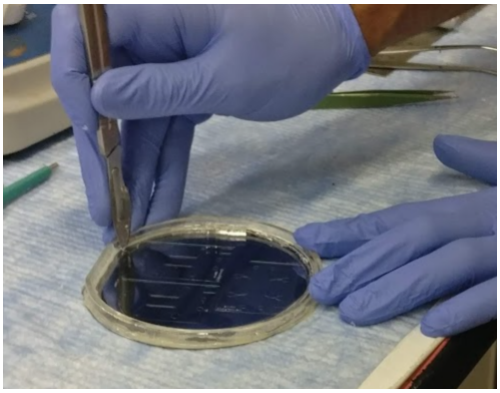

Figure 5.8: The cured PDMS mixture is removed from the silicon wafer using a scalpel

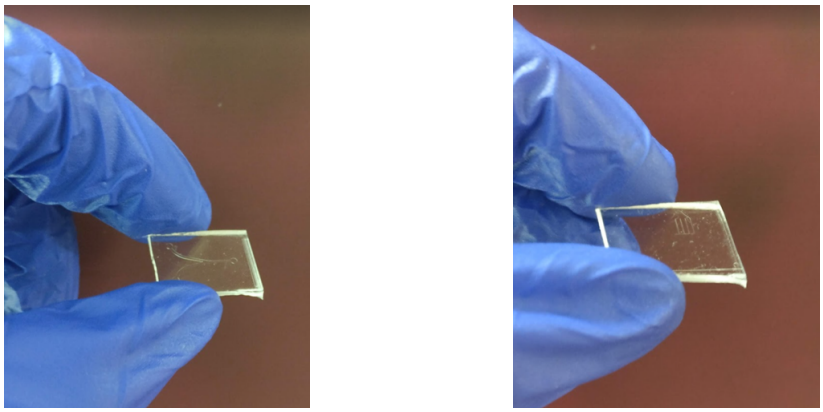

(a) (b)

Figure 5.9: The two layers of the buffer exchange device for a 4 side channel configuration made from PDMS (a) first layer (b) second layer

purple light, as seen in Figure 5.10, was observed inside the chamber.

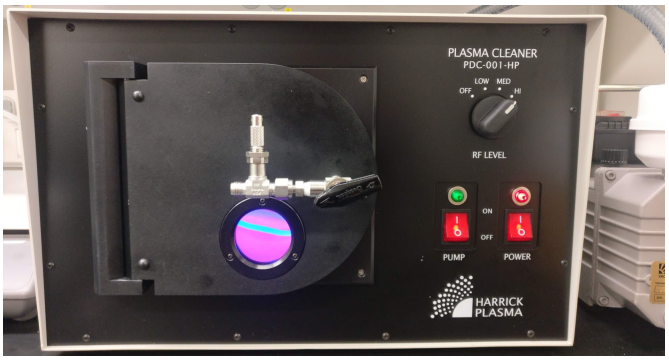

Figure 5.10: Surface treatment of PDMS by ionic plasma oxidation for bonding the two layers of the device

The oxygen ions in the plasma bombard the surface of the PDMS and replace one of the methyl (CH_3) groups in the monomer with an hydroxyl group ($-OH$) [9]. When two such treated surfaces are then brought together, they form a strong covalent bond [23] that can withstand pressures of up to 690 kPa or 100 Psi [75]. Since the bond strength is weaker for exposure times of less than 1 minute [7], the layers were surface treated for a full 2 minutes. Once sufficient surface treatment was achieved, the pump and the plasma circuit were switched off and the needle value orientation was adjusted to release the vacuum in the

chamber until atmospheric pressure was reached. Finally, the surface treated PDMS layers were removed from the plasma cleaner and care was taken to avoid touching the treated surface.

The layer containing the inlet and main channels was placed on a standard glass slide with the treated surface facing up. The slide was placed under a microscope with 5X magnification and the focus was adjusted until the channel and its walls were clearly visible. Then, the second layer containing the side channel was manually hovered a few millimeters over the first layer with the treated surface facing down. For getting the two layers aligned such that the overlap between the main and side channels were as close to 5 μm as possible, the layers were aligned visually under the microscope. Care was taken to get the desired alignment the first time the two layers made contact to ensure strong bonding between PDMS layers, since multiple attempts at bonding weakens the bond strength. The bonded surface was left overnight to maximize the bond strength between the PDMS layers. Figure 5.11 shows the two layers that have been bonded together for a 1 side channel device configuration. Figure 5.12, Figure 5.13, Figure 5.14 and Figure 5.15 show the microscope images of the bonded layers and the overlap between the main and the side channels for the other devices.

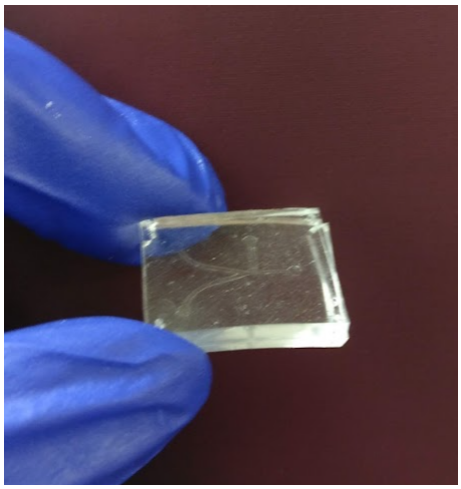

Figure 5.11: Bonded PDMS layers for 1 side channel configuration

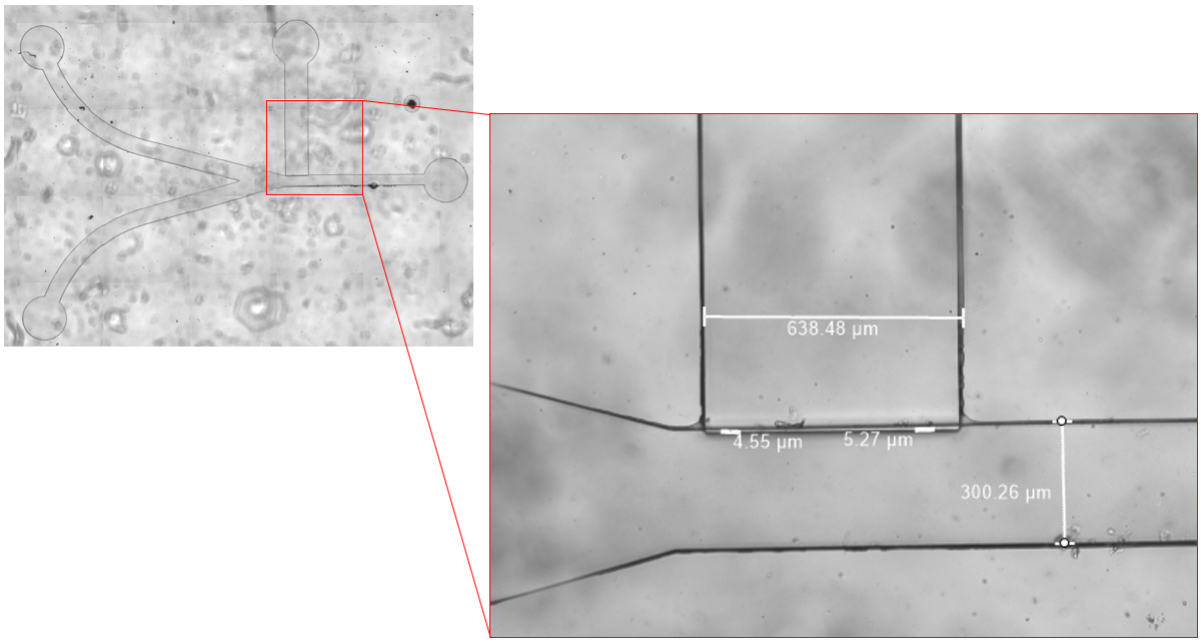

Figure 5.12: Microscope image of a 1 side channel configuration

The images were captured using the 5X and 20X magnifications in an incubated CO_2 controlled Zeiss epifluorescent microscope (Oberkochen, Germany) at the CEH , Virginia Tech. It could be observed that the overlap between the channels ranged from 2 μm to 13 μm. The range of variation is the result of manual alignment of the layers under the microscope. These values of overlap are acceptable for initial fabrication and testing since it is lower than the average cancer cell diameter of 20 μm. Upon initial prototyping and evaluation, for scaling up the fabrication of the device, precision alignment techniques, similar to mask aligners, could be employed to achieve better accuracy and control of the overlap between the two layers. The debris observed in the channels could be eliminated by fabricating the device in a cleanroom environment.

Once the layers were bonded, the inlet and outlet holes were punched using a Rapid Core (Ted Pella Inc, Redding, CA) 0.75mm hole puncher, as shown in Figure 5.16. Once the holes were punched, the device was plasma bonded to a glass slide on one side, as shown in

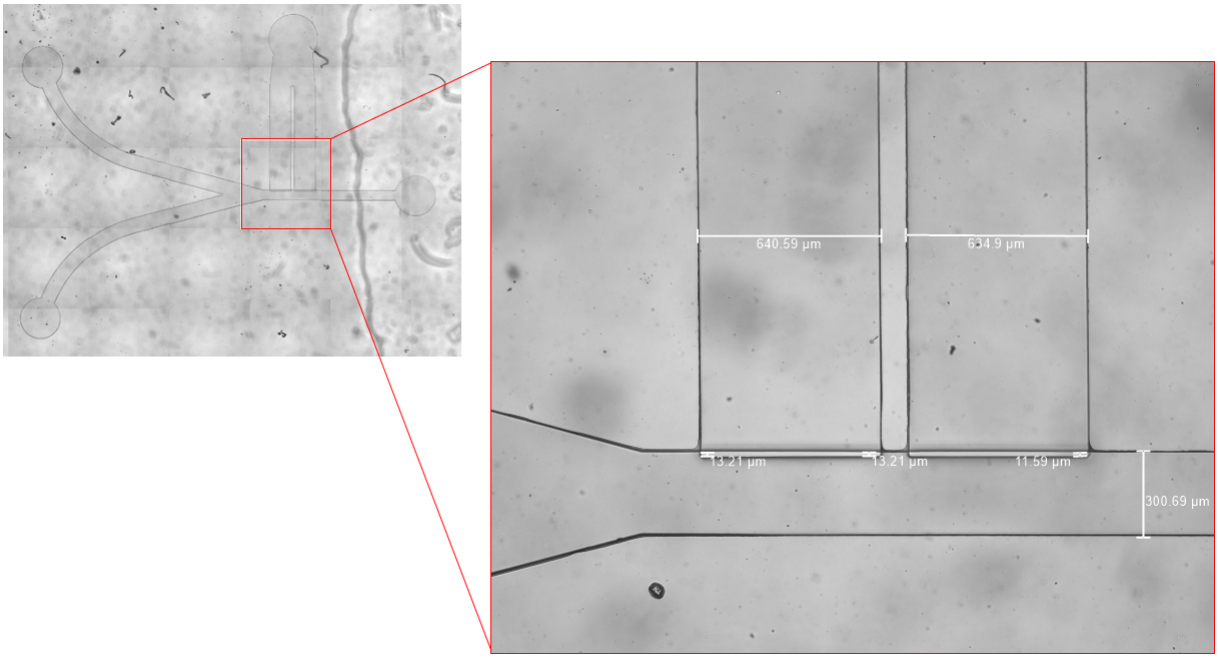

Figure 5.13: Microscope image of a 2 side channel configuration

Figure 5.17 to prevent the fluid from leaking out through the punched hole.

The setup was left undisturbed overnight to obtain maximum bond strength between the PDMS and glass slide. This bonding is the final step in the fabrication of the PDMS buffer exchange device, which can now be used for running tests and cell experiments. Testing and evaluation is planned as a part of future work and is not within the scope of this thesis.

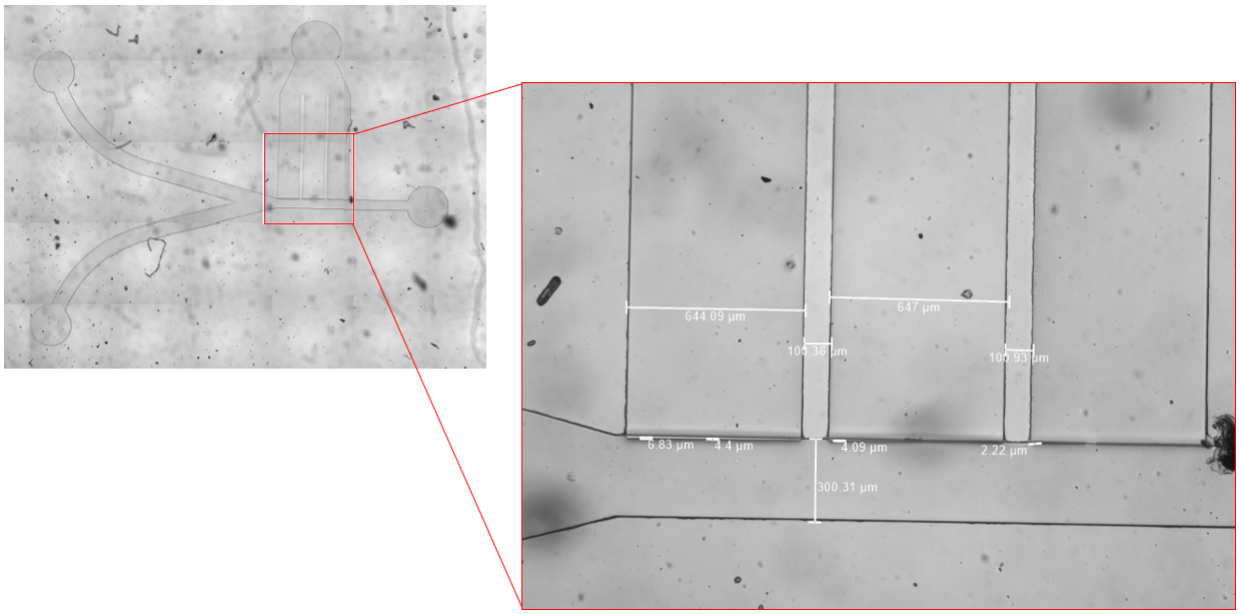

Figure 5.14: Microscope image of a 3 side channel configuration

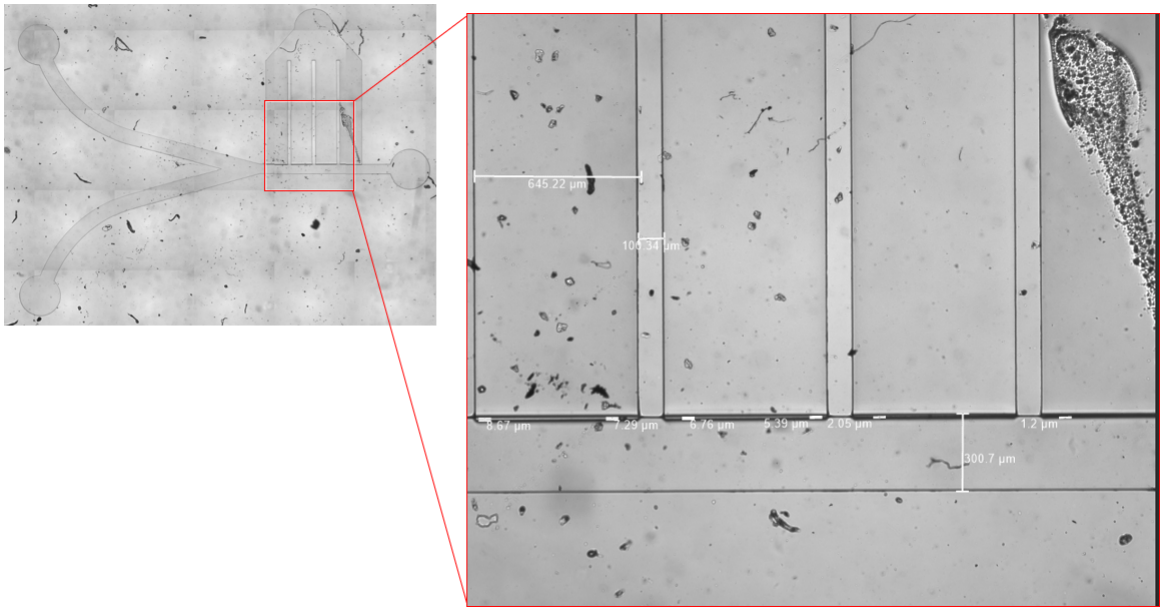

Figure 5.15: Microscope image of a 4 side channel configuration

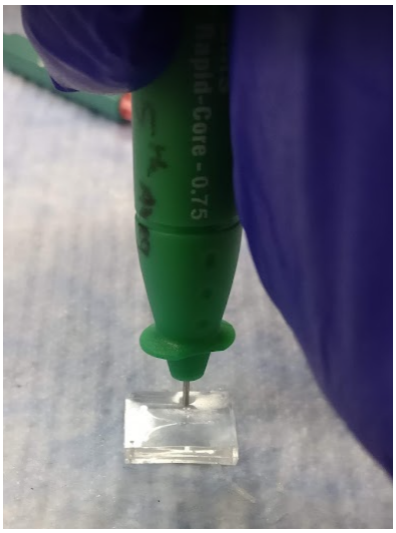

Figure 5.16: Inlet and outlet holes for connecting 30 gauge tubing punched with a 0.75 mm biopsy punch

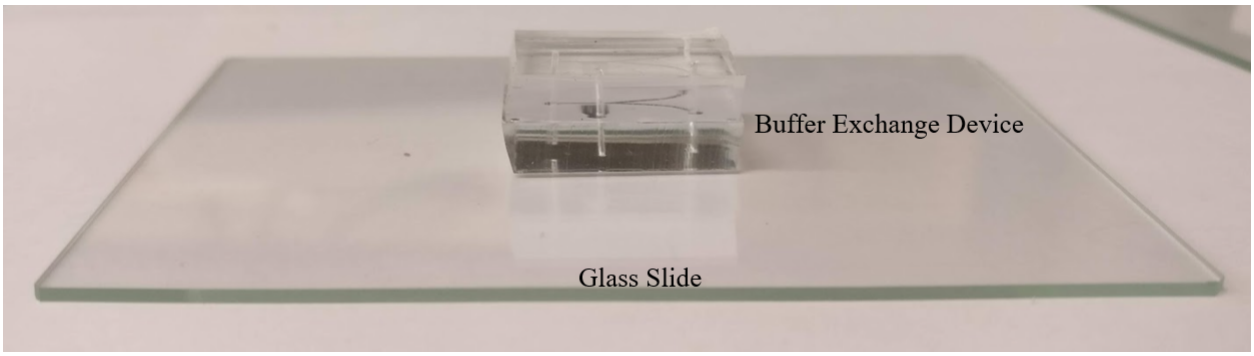

Figure 5.17: The device is plasma bonded with a $2inX3in$ 1mm thick microscope slide

Chapter 6

Conclusions and Future Work

A novel passive microfluidic device was designed for effective buffer transfer for cells. The device leverages various microfluidic techniques and methods including inertial focusing, pinched flow fractionation, cross flow filtration and hydrodynamic size based filtration. Three-dimensional CAD modeling was used to design the device. Computational fluid dynamic modeling was used to analyse the velocity field and diffusion within the channel. A parametric study was performed to determine the optimal channel configurations that induced low shear stress, supported high throughput and maintained minimal diffusion.

The proposed design has multiple advantages over the standard manual technique of buffer exchange. While the manual method for buffer transfer takes about 45 minutes to get viable cells, the proposed device is capable of performing buffer transfer in 6 seconds and the viable cells can be directly sent to the downstream analysis device using outlet tubing.

In the manual method, there is very little control over the shear forces imparted on the cells, since the cells are isolated using a centrifuge. However, in the proposed device, the shear stress value is controlled by varying the total flowrate through the device and the flowrate ratio between the inlets. The maximum shear stress value in the proposed device is less than the typical average shear stress experienced by cells in a biological system. Moreover, the residence time of cells in such maximum shear stress areas in the channel is less than 0.4 seconds. This minimal exposure to shear stress helps in preventing cell lysis and greatly increases the cell viability at the outlet.

The electrical conductivity value of the buffer at the main channel outlet, where the cells are collected for downstream cDEP analysis, is consistently maintained at or below the required value. Since maintaining a low conductivity is critical for performing cDEP analysis on cells, the proposed device is designed to precisely maintain the outlet conductivity. However, in the manual method, the only way to reach the desired conductivity value is to add precise quantities of the buffer to the centrifuged cells. Since even a small additional quantity of buffer will irreversibly alter the conductivity, this process is delicate and can affect the downstream cDEP experiment. In the proposed device, the value of the conductivity can be precisely controlled by varying the inlet flowrate and flowrate ratio of the cell medium and the buffer.

Finally, expensive laboratory equipment is needed for the manual process. In contrast, the proposed device is developed from cost effective PDMS based fabrication methods. Its easy-to-use design eliminates the need for expensive equipment and significantly reduces manual efforts. While fabricating the device in the lab, the critical channel overlap of 5 μm was achieved. This small gap helps to effectively filter the cells while allowing removal of the biological buffer.

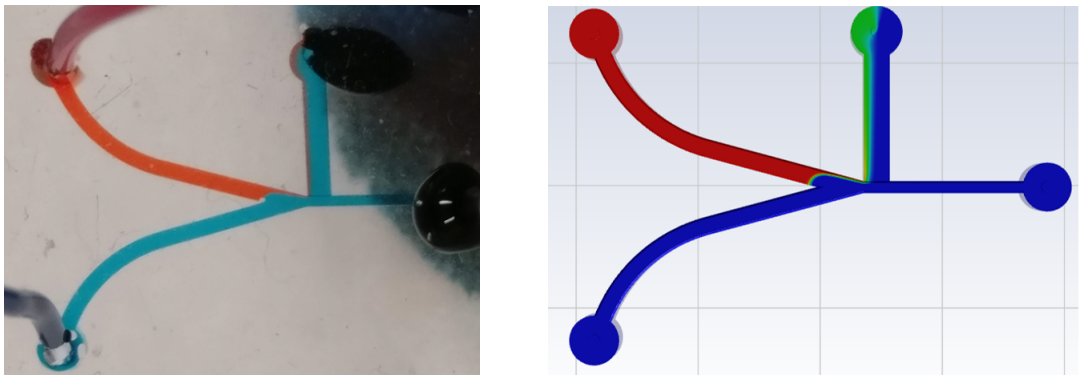

(a) (b)

Figure 6.1: Comparison of diffusion profiles between (a) the physical device and (b) the CFD model

Figure 6.1 shows a comparison between diffusion profiles in the physical device and in the CFD model for the 1 side channel configuration. The experimental diffusion profile in Figure 6.1a was obtained in preliminary testing at the Center for Engineered Health (CEH) at Virginia Tech. It can be observed that the profile in the physical device matches the CFD model well. This further proves the robust design methodology used in developing the device.

From the above results and observations, it is concluded that the novel passive microfluidic device proposed in this work is a significant improvement over current manual buffer transfer methods.

6.1 Future Work

The following are suggested as additional steps to advancing this work.

- Conduct further testing with different configurations of the device to measure the outlet conductivity at different flowrates.
- Conduct testing with polystyrene beads suspended in the 10X PBS solution to evaluate the filtration and buffer transfer capabilities of the device.
- Experiment with cancer cells to evaluate effectiveness buffer transfer.
- Establish robust fabrication protocols for scaling up production of the device.
- Integrate the buffer transfer device with the downstream cDEP device for in-situ buffer transfer, cell sorting and characterization experiments.

The results of this research will help in furthering the efforts in the domain of microfluidic device development, cell manipulations and buffer transfer.

Bibliography

[1] Amirah Abdullah, Imran Syakir Mohamad, Ahmad Yusairi Bani Hashim, Norli Abdullah, Ban Wei Poh, Mohamed Hafiz Md Isa, and Syazwani Zainal Abidin. Thermal conductivity and viscosity of deionised water and ethylene glycol-based nanofluids. *Journal of Mechanical Engineering and Sciences (JMES)*, 10:2249–2261, 2016.

[2] P Abgrall and AM Gue. Lab-on-chip technologies: making a microfluidic network and coupling it into a complete microsystem—a review. *Journal of micromechanics and microengineering*, 17(5):R15, 2007.

[3] John F Ashley, Christopher N Bowman, and Robert H Davis. Hydrodynamic separation of particles using pinched-flow fractionation. *AIChE Journal*, 59(9):3444–3457, 2013.

[4] J Matthew Barnes, Jones T Nauseef, and Michael D Henry. Resistance to fluid shear stress is a conserved biophysical property of malignant cells. *PloS one*, 7(12):e50973, 2012.

[5] Timothy Barth and Dennis Jespersen. The design and application of upwind schemes on unstructured meshes. In *27th Aerospace sciences meeting*, page 366, 1989.

[6] P Bourdin and John D Wilson. Windbreak aerodynamics: is computational fluid dynamics reliable? *Boundary-layer meteorology*, 126(2):181–208, 2008.

[7] C-f Chen and KJRA Wharton. Characterization and failure mode analyses of air plasma oxidized pdms–pdms bonding by peel testing. *RSC advances*, 7(3):1286–1289, 2017.

[8] Chen Tung A Chen. Specific heat capacities of aqueous sodium chloride solutions at high pressures. *Journal of Chemical and Engineering Data*, 27(3):356–358, 1982.

[9] I-Jane Chen and Ernö Lindner. The stability of radio-frequency plasma-treated polydimethylsiloxane surfaces. *Langmuir*, 23(6):3118–3122, 2007.

[10] Jian Chen, Jason Li, and Yu Sun. Microfluidic approaches for cancer cell detection, characterization, and separation. *Lab on a Chip*, 12(10):1753–1767, 2012.

[11] Dino Di Carlo, Daniel Irimia, Ronald G Tompkins, and Mehmet Toner. Continuous inertial focusing, ordering, and separation of particles in microchannels. *Proceedings of the National Academy of Sciences*, 104(48):18892–18897, 2007.

[12] Mark A Eddings, Michael A Johnson, and Bruce K Gale. Determining the optimal pdms–pdms bonding technique for microfluidic devices. *Journal of Micromechanics and Microengineering*, 18(6):067001, 2008.

[13] Karl Egan, Niamh Cooke, and Dermot Kenny. Living in shear: platelets protect cancer cells from shear induced damage. *Clinical & experimental metastasis*, 31(6):697–704, 2014.

[14] Ana C Fernandes, Carla M Duarte, Filipe A Cardoso, Ricardo Bexiga, Susana Cardoso, and Paulo P Freitas. Lab-on-chip cytometry based on magnetoresistive sensors for bacteria detection in milk. *Sensors*, 14(8):15496–15524, 2014.

[15] D Gazzola, E Franchi Scarselli, and R Guerrieri. 3d visualization of convection patterns in lab-on-chip with open microfluidic outlet. *Microfluidics and nanofluidics*, 7(5):659–668, 2009.

[16] AT Giannitsis and M Min. Usage of microfluidic lab-on-chips in biomedicine. In *2010 12th Biennial Baltic Electronics Conference*, pages 249–252. IEEE, 2010.

[17] Frank A Gomez. The future of microfluidic point-of-care diagnostic devices. *Bioanalysis*, 5(1):1–3, 2013.

[18] Guofeng Guan, Lidan Wu, Ali Asgar Bhagat, Zirui Li, Peter CY Chen, Shuzhe Chao, Chong Jin Ong, and Jongyoon Han. Spiral microchannel with rectangular and trapezoidal cross-sections for size based particle separation. *Scientific reports*, 3(1):1–9, 2013.

[19] A Haider and O Levenspiel. Drag coefficient and terminal velocity of spherical and nonspherical particles. *Powder technology*, 58(1):63–70, 1989.

[20] B Håkansson and P Andersson. Thermal conductivity and heat capacity of solid nacl and nai under pressure. *Journal of Physics and Chemistry of Solids*, 47(4):355–362, 1986.

[21] Tomiichi Hasegawa, Akiomi Ushida, and Takatsune Narumi. A simple expression for pressure drops of water and other low molecular liquids in the flow through micro-orifices. *Physics of Fluids*, 27(12):122001, 2015.

[22] John David Hem. *Study and interpretation of the chemical characteristics of natural water*, volume 2254. Department of the Interior, US Geological Survey, 1985.

[23] John R Hollahan and George L Carlson. Hydroxylation of polymethylsiloxane surfaces by oxidizing plasmas. *Journal of applied polymer science*, 14(10):2499–2508, 1970.

[24] Han Wei Hou, Majid Ebrahimi Warkiani, Bee Luan Khoo, Zi Rui Li, Ross A Soo, Daniel Shao-Weng Tan, Wan-Teck Lim, Jongyoon Han, Ali Asgar S Bhagat, and Chwee Teck Lim. Isolation and retrieval of circulating tumor cells using centrifugal forces. *Scientific reports*, 3(1):1–8, 2013.

[25] Lotien Richard Huang, Edward C Cox, Robert H Austin, and James C Sturm. Continuous particle separation through deterministic lateral displacement. *Science*, 304(5673): 987–990, 2004.

[26] ANSYS Inc. *ANSYS Fluent Theory Guide, 2021 R2.* ANSYS, 2021.

[27] FT Johnson, DS Kamenetskiy, RG Melvin, V Venkatakrishnan, Laurence B Wigton, DP Young, SR Allmaras, JE Bussoletti, and CL Hilmes. Observations regarding algorithms required for robust cfd codes. *Mathematical Modelling of Natural Phenomena*, 6 (3):2–27, 2011.

[28] Jiwoo Kang, Jong-Cheol Choi, Miju Kim, Hong-Ryul Jung, and Junsang Doh. Photopatterning with a printed transparency mask and a protein-friendly photoresist. *Methods in cell biology*, 119:55–72, 2014.

[29] J Mikael Karlsson, Muriel Gazin, Sanna Laakso, Tommy Haraldsson, Surbhi Malhotra-Kumar, Minna Mäki, Herman Goossens, and Wouter van der Wijngaart. Active liquid degassing in microfluidic systems. *Lab on a Chip*, 13(22):4366–4373, 2013.

[30] Ga-Yeong Kim, Jong-In Han, and Je-Kyun Park. Inertial microfluidics-based cell sorting. *BioChip Journal*, 12(4):257–267, 2018.

[31] Gang-Min Kim, Sung-Jun Lee, and Chang-Lae Kim. Assessment of the physical, mechanical, and tribological properties of pdms thin films based on different curing conditions. *Materials*, 14(16):4489, 2021.

[32] Jung Ho Kim, King Tong Lau, Rod Shepherd, Yanzhe Wu, Gordon Wallace, and Dermot Diamond. Performance characteristics of a polypyrrole modified polydimethylsiloxane (pdms) membrane based microfluidic pump. *Sensors and Actuators A: Physical*, 148 (1):239–244, 2008.

[33] Franz Laermer and Andrea Urban. *Through-Silicon Vias Using Bosch DRIE Process Technology*, pages 81–91. Springer New York, New York, NY, 2011. ISBN 978-1-4419-7276-7. doi: 10.1007/978-1-4419-7276-7_9. URL https://doi.org/10.1007/978-1-4419-7276-7_9.

[34] Franz Laermer, Sami Franssila, Lauri Sainiemi, and Kai Kolari. Chapter 21 - deep reactive ion etching. In Markku Tilli, Teruaki Motooka, Veli-Matti Airaksinen, Sami Franssila, Mervi Paulasto-Kröckel, and Veikko Lindroos, editors, *Handbook of Silicon Based MEMS Materials and Technologies (Second Edition)*, Micro and Nano Technologies, pages 444–469. William Andrew Publishing, Boston, second edition edition, 2015. ISBN 978-0-323-29965-7. doi: https://doi.org/10.1016/B978-0-323-29965-7.00021-X. URL https://www.sciencedirect.com/science/article/pii/B978032329965700021X.

[35] Thomas Laurell, Filip Petersson, and Andreas Nilsson. Chip integrated strategies for acoustic separation and manipulation of cells and particles. *Chemical Society Reviews*, 36(3):492–506, 2007.

[36] Jessamine Ng Lee, Xingyu Jiang, Declan Ryan, and George M Whitesides. Compatibility of mammalian cells on surfaces of poly (dimethylsiloxane). *Langmuir*, 20(26): 11684–11691, 2004.

[37] Wonhee Lee, Peter Tseng, and Dino Di Carlo. Microfluidic cell sorting and separation technology. In *Microtechnology for Cell Manipulation and Sorting*, pages 1–14. Springer, 2017.

[38] Amy Li and Goodarz Ahmadi. Dispersion and deposition of spherical particles from point sources in a turbulent channel flow. *Aerosol science and technology*, 16(4):209–226, 1992.

[39] George Luka, Ali Ahmadi, Homayoun Najjaran, Evangelyn Alocilja, Maria DeRosa, Kirsten Wolthers, Ahmed Malki, Hassan Aziz, Asmaa Althani, and Mina Hoorfar. Microfluidics integrated biosensors: A leading technology towards lab-on-a-chip and sensing applications. *Sensors*, 15(12):30011–30031, 2015.

[40] J McGrath, M Jimenez, and H Bridle. Deterministic lateral displacement for particle separation: a review. *Lab on a Chip*, 14(21):4139–4158, 2014.

[41] AR Mirza. One micron precision, wafer-level aligned bonding for interconnect, mems and packaging applications. In *2000 Proceedings. 50th Electronic Components and Technology Conference (Cat. No. 00CH37070)*, pages 676–680. IEEE, 2000.

[42] Hisham Mohamed, James N Turner, and Michele Caggana. Biochip for separating fetal cells from maternal circulation. *Journal of Chromatography A*, 1162(2):187–192, 2007.

[43] SAJ Morsi and AJ Alexander. An investigation of particle trajectories in two-phase flow systems. *Journal of Fluid mechanics*, 55(2):193–208, 1972.

[44] Shashi K Murthy, Palaniappan Sethu, Gordana Vunjak-Novakovic, Mehmet Toner, and Milica Radisic. Size-based microfluidic enrichment of neonatal rat cardiac cell populations. *Biomedical microdevices*, 8(3):231–237, 2006.

[45] Joanna Mystkowska, Dąbrowski J.R., Krzysztof Kowal, Katarzyna Niemirowicz Laskowska, and Halina Car. Physical and chemical properties of deionized water and saline treated with low-pressure and low-temperature plasma. *Chemik*, 67:719–724, 01 2013.

[46] Vigneswaran Narayanamurthy, ZE Jeroish, KS Bhuvaneshwari, Pouriya Bayat, R Premkumar, Fahmi Samsuri, and Mashitah M Yusoff. Advances in passively driven microfluidics and lab-on-chip devices: a comprehensive literature review and patent analysis. *RSC Advances*, 10(20):11652–11680, 2020.

[47] Hyun Woo Nho and Tae Hyun Yoon. Enhanced separation of colloidal particles in an aspff device with a tilted sidewall and vertical focusing channels (t-aspff-v). *Lab on a Chip*, 13(5):773–776, 2013.

[48] Hyun Woo Nho, Nuri Yang, Jaewoo Song, Joon Shik Park, and Tae Hyun Yoon. Separations of spherical and disc-shaped polystyrene particles and blood components (red blood cells and platelets) using pinched flow fractionation device with a tilted sidewall and vertical focusing channels (t-pff-v). *Sensors and Actuators B: Chemical*, 249: 131–141, 2017.

[49] Hyun Woo Nho, Nuri Yang, Jaewoo Song, Joon Shik Park, and Tae Hyun Yoon. Separations of spherical and disc-shaped polystyrene particles and blood components (red blood cells and platelets) using pinched flow fractionation device with a tilted sidewall and vertical focusing channels (t-pff-v). *Sensors and Actuators B: Chemical*, 249: 131–141, 2017.

[50] Joseph Ong, Giora Enden, and Aleksander S Popel. Converging three-dimensional stokes flow of two fluids in a t-type bifurcation. *Journal of fluid mechanics*, 270:51–72, 1994.

[51] Nicole Pamme and Andreas Manz. On-chip free-flow magnetophoresis: continuous flow separation of magnetic particles and agglomerates. *Analytical chemistry*, 76(24):7250–7256, 2004.

[52] Vahidreza Parichehreh, Krishnakiran Medepallai, Karan Babbarwal, and Palaniappan Sethu. Microfluidic inertia enhanced phase partitioning for enriching nucleated cell populations in blood. *Lab on a Chip*, 13(5):892–900, 2013.

[53] SV Patankar, CH Liu, and EM Sparrow. Fully developed flow and heat transfer in ducts having streamwise-periodic variations of cross-sectional area. 1977.

[54] Kiran Raj M and Suman Chakraborty. Pdms microfluidics: A mini review. *Journal of Applied Polymer Science*, 137(27):48958, 2020.

[55] Sagar Regmi, Afu Fu, and Kathy Qian Luo. High shear stresses under exercise condition destroy circulating tumor cells in a microfluidic system. *Scientific reports*, 7(1):1–12, 2017.

[56] Anna F Rusydi. Correlation between conductivity and total dissolved solid in various type of water: A review. In *IOP conference series: earth and environmental science*, volume 118, page 012019. IOP Publishing, 2018.

[57] NW Ryan and MM Johnson. Transistion from laminar to turbulent flow in pipes. *AIChE Journal*, 5(4):433–435, 1959.

[58] Ahmet C Sabuncu, Anthony J Asmar, Michael W Stacey, and Ali Beskok. Differential dielectric responses of chondrocyte and jurkat cells in electromanipulation buffers. *Electrophoresis*, 36(13):1499–1506, 2015.

[59] PGT Saffman. The lift on a small sphere in a slow shear flow. *Journal of fluid mechanics*, 22(2):385–400, 1965.

[60] Alireza Salmanzadeh, Hadi Shafiee, Mike B Sano, Mark A Stremler, and Rafael V Davalos. Enrichment of cancer cells using a high throughput contactless dielectrophoretic (cdep) microfluidic device. In *Summer Bioengineering Conference*, volume 54587, pages 47–48. American Society of Mechanical Engineers, 2011.

[61] Urban Seger-Sauli, Marilia Panayiotou, Silvan Schnydrig, Martin Jordan, and Philippe Renaud. Temperature measurements in microfluidic systems: Heat dissipation of negative dielectrophoresis barriers. *Electrophoresis*, 26(11):2239–2246, 2005.

[62] DG Sharp and JW Beard. Size and density of polystyrene particles measured by ultracentrifugation. *Journal of Biological Chemistry*, 185(1):247–253, 1950.

[63] Kendra V Sharp and Ronald J Adrian. Transition from laminar to turbulent flow in liquid filled microtubes. *Experiments in fluids*, 36(5):741–747, 2004.

[64] C Wyatt Shields IV, Catherine D Reyes, and Gabriel P López. Microfluidic cell sorting: a review of the advances in the separation of cells from debulking to rare cell isolation. *Lab on a Chip*, 15(5):1230–1249, 2015.

[65] Muthusaravanan Sivaramakrishnan, Ram Kothandan, Deenadayalan Karaiyagowder Govindarajan, Yogesan Meganathan, and Kumaravel Kandaswamy. Active microfluidic systems for cell sorting and separation. *Current Opinion in Biomedical Engineering*, 13:60–68, 2020.

[66] Steven A Soper, Sean M Ford, Shize Qi, Robin L McCarley, Kevin Kelly, and Michael C Murphy. Peer reviewed: Polymeric microelectromechanical systems., 2000.

[67] Salvatore P Sutera and Richard Skalak. The history of poiseuille's law. *Annual review of fluid mechanics*, 25(1):1–20, 1993.

[68] Makiko Tahara, Takeshi Inoue, Yasuyuki Miyakura, Hisanaga Horie, Yoshikazu Yasuda, Hirofumi Fujii, Kenjiro Kotake, and Kokichi Sugano. Cell diameter measurements obtained with a handheld cell counter could be used as a surrogate marker of g2/m arrest and apoptosis in colon cancer cell lines exposed to sn-38. *Biochemical and Biophysical Research Communications*, 434(4):753–759, 2013.

[69] Hsih Yin Tan, Weng Keong Loke, and Nam-Trung Nguyen. A reliable method for bonding polydimethylsiloxane (pdms) to polymethylmethacrylate (pmma) and its application in micropumps. *Sensors and Actuators B: Chemical*, 151(1):133–139, 2010.

[70] Hsih Yin Tan, Weng Keong Loke, and Nam-Trung Nguyen. A reliable method for

bonding polydimethylsiloxane (pdms) to polymethylmethacrylate (pmma) and its application in micropumps. *Sensors and Actuators B: Chemical*, 151(1):133–139, 2010.

[71] JE Tanner and FW Lamb. Specific heats of aqueous solutions of nacl, nabr, and kcl: Comparisons with related thermal properties. *Journal of Solution Chemistry*, 7(4): 303–316, 1978.

[72] Hui Min Tay, David C Yeo, Christian Wiraja, Chenjie Xu, and Han Wei Hou. Microfluidic buffer exchange for interference-free micro/nanoparticle cell engineering. *Journal of visualized experiments: JoVE*, (113), 2016.

[73] Joe F Thompson, Joseph L Steger, and HY Yoshihara. Three dimensional grid generation for complex configurations-recent progress. 1988.

[74] Lucas H Ting, Shirin Feghhi, Sangyoon J Han, Marita L Rodriguez, and Nathan J Sniadecki. Effect of silanization film thickness in soft lithography of nanoscale features. *Journal of Nanotechnology in Engineering and Medicine*, 2(4), 2011.

[75] Marc A Unger, Hou-Pu Chou, Todd Thorsen, Axel Scherer, and Stephen R Quake. Monolithic microfabricated valves and pumps by multilayer soft lithography. *Science*, 288(5463):113–116, 2000.

[76] Marinke W van Der Helm, Andries D Van Der Meer, Jan CT Eijkel, Albert van den Berg, and Loes I Segerink. Microfluidic organ-on-chip technology for blood-brain barrier research. *Tissue barriers*, 4(1):e1142493, 2016.

[77] V Vitagliano and Phillip A Lyons. Diffusion coefficients for aqueous solutions of sodium chloride and barium chloride. *Journal of the American Chemical Society*, 78(8):1549–1552, 1956.

[78] NRG Walton. Electrical conductivity and total dissolved solids—what is their precise relationship? *Desalination*, 72(3):275–292, 1989.

[79] Lin Wang, Robin Quant, and Athanasios Kolios. Fluid structure interaction modelling of horizontal-axis wind turbine blades based on cfd and fea. *Journal of Wind Engineering and Industrial Aerodynamics*, 158:11–25, 2016.

[80] Shengyi Wang, Derek B Ingham, Lin Ma, Mohamed Pourkashanian, and Zhi Tao. Numerical investigations on dynamic stall of low reynolds number flow around oscillating airfoils. *Computers & fluids*, 39(9):1529–1541, 2010.

[81] NP Weatherill. Mixed structured-unstructured meshes for aerodynamic flow simulation. *The Aeronautical Journal*, 94(934):111–123, 1990.

[82] Frank M White and Joseph Majdalani. *Viscous fluid flow*, volume 3. McGraw-Hill New York, 2006.

[83] George M Whitesides. The origins and the future of microfluidics. *nature*, 442(7101): 368–373, 2006.

[84] Masumi Yamada, Megumi Nakashima, and Minoru Seki. Pinched flow fractionation: continuous size separation of particles utilizing a laminar flow profile in a pinched microchannel. *Analytical chemistry*, 76(18):5465–5471, 2004.

[85] Masumi Yamada, Kyoko Kano, Yukiko Tsuda, Jun Kobayashi, Masayuki Yamato, Minoru Seki, and Teruo Okano. Microfluidic devices for size-dependent separation of liver cells. *Biomedical microdevices*, 9(5):637–645, 2007.

[86] Hoyoung Yun, Kisoo Kim, and Won Gu Lee. Cell manipulation in microfluidics. *Biofabrication*, 5(2):022001, 2013.

[87] Yan Zeng, Thong-See Lee, Peng Yu, Partha Roy, and Hong-Tong Low. Mass transport and shear stress in a microchannel bioreactor: numerical simulation and dynamic similarity. 2006.

[88] Haoqing Zhang, Honglong Chang, and Pavel Neuzil. Dep-on-a-chip: Dielectrophoresis applied to microfluidic platforms. *Micromachines*, 10(6):423, 2019.